UNIVERSITY OF CALIFORNIA

Santa Barbara

# Enhanced Conductivity and Photon Upconversion in Organic Semiconductors

A Thesis submitted in partial satisfaction of the

requirements for the degree Master of Science

in Chemistry

by

Alana Lorraine Dixon

Committee in charge:

Professor Thuc-Quyen Nguyen, Chair

Professor Mattanjah S. de Vries

Professor Christopher Bates

September 2022

The thesis of Alana Lorraine Dixon is approved.

_____
Mattanjah S. de Vries

_____
Christopher Bates

_____
Thuc-Quyen Nguyen, Committee Chair

September 2022

ACKNOWLEDGEMENTS

The course of this thesis coincided with some very difficult times in my personal life. My wonderful best friend, Abby Tran, has helped me see this through with her delightful abundance of compassion, caring, humor and strength. I would like to thank my friends and fellow researchers at UCSB for every moment of commiseration or fun diversions. For their honest and comforting conversations, I would especially like to thank Sheila Kulkarni, Jackie Rohrer and Luana Llanes. I already miss all of my fellow lab mates as well as the visiting researchers who also shared their free-time with us in the Nguyen group. I will continue to cherish the memories of meandering conversations ranging from scientific ideas to hilarious life stories, the occasional movie night, attempts at completing a single basketball game without injury, and all of the smaller bits of levity such as the jumping husky. Of course, I would not have had the opportunity to meet such enjoyable and talented researchers without being welcomed into the lab by Professor Quyen Nguyen whom I would like to thank not only for guiding my research, but also for meaningful and inspiring conversations on the difficulties of life. I would like to also thank the entire lab for their sweet condolences after my mother passed away last September.

Finally, I would like to dedicate this thesis to my mom Victoreen "Vikki" Dixon, a fantastic storyteller and an incredibly sweet, caring, welcoming, bold and hilarious woman whom I am indescribably lucky to have had in my life.

*The work in this thesis was supported by the US Department of Energy under Award no. DE-SC0017659 and by the Department of the Navy, Office of Naval Research (Award No. N000142112181).*

ABSTRACT

Enhanced Conductivity and Photon Upconversion in Organic Semiconductors

by

Alana Lorraine Dixon

This thesis details a morphological study of organic semiconductors (OSCs) that is doped through the use of small molecule dopants and a spectroscopic study of photon upconversion of organic molecules. As OSCs suffer lower intrinsic conductivities than their inorganic counterparts, comprehensive understandings of successful doping strategies are of great importance. Impacts of added dopants on the intermolecular arrangement of the OSC are crucial considerations as charge transport relies upon the close arrangement of conjugated portions of OSC polymers or small molecules. The study discussed herein utilizes solid state nuclear magnetic resonance (ssNMR) and electron paramagnetic resonance (EPR) techniques to compare interactions between two dopants F4TCNQ (2,3,5,6-tetrafluoro-7,7,8,8-tetracyanoquinodimethane) and BCF (tris[pentafluorophenyl] borane), when blended with the polymer PCPDTBT (P4) (poly[2,6-(4,4-bis(2-hexadecyl)-4H-cyclopenta[2,1-b;3,4-b′]dithiophene)-alt-4,7(2,1,3-benzothiadiazole).

The congregation of ssNMR and EPR results provides details explaining the previously observed lower P4 doping efficiency exhibited by F4TCNQ in comparison to BCF. Comparison of 1H and 13C ssNMR spectra from P4, P4:BCF, and P4:F4TCNQ blends reveal dopants alter the local arrangement of P4, both broadening and decreasing the intensity of the signal produced

in the NMR spectra. Hyperfine interactions resolved via two-dimensional pulsed EPR measurements provided evidence that F4TCNQ intercalates between the conjugated moieties of the P4 polymer backbone. In contrast, BCF was found to be closely associated, but not inserted between the P4 backbone units. Both spectroscopic methods reveal a more severe disruption of the local arrangement of P4 when F4TCNQ serves as the dopant in comparison to BCF. Examination of the 19F ssNMR spectra illustrate an additional environment in which F4TCNQ molecules form aggregates outside of the P4 polymer, in agreement with previous studies suggesting F4TCNQ forms clusters due to its low solubility in organic solvents popularly used for OSC processing.

Advancing the frontier of research in the field of photon upconversion involves seeking improvements in the parameters for efficiency (upconversion quantum yield) and performance (anti-Stokes shift) as well as reducing material costs. Herein a novel ternary upconversion system is designed which exhibits an over two-fold improvement in upconversion efficiency compared to the corresponding binary scheme. In both systems, visible light is first absorbed by the sensitizer 4CzIPN, a molecule which displays thermally activated delayed fluorescence (TADF) without relying on costly or toxic heavy metals, and ultimately emitted from p-terphenyl in order to preserve the anti-Stokes shift of 0.83 eV. 4CzIPN still demonstrated considerable delayed fluorescence in the presence of p-terphenyl, as a result of inefficient energy harvesting. Comparing the delayed fluorescence from 4CzIPN in the presence of various acceptors in combination with DFT simulations of excited state energy levels allowed the identification of 1-methylnaphthalene as the ideal intermediate acceptor to add to the binary system, producing a ternary blend with an enhanced upconversion efficiency of 7.6 %.

## Curriculum Vitae

### *Education*

2022 M. S. in Chemistry (expected), University of California, Santa Barbara (UCSB)

2018 B. S. in Chemistry, University of New Orleans (UNO)

### *Publications*

2022 Yurash, B., **Dixon, A.**, Espinoza, C., Mikhailovsky, A., Chae, S., Nakanotani, H., Adachi, C., Nguyen, T.Q. Efficiency of Thermally Activated Delayed Fluorescence Sensitized Triplet Upconversion Doubled in Three-Component System. *Adv. Mater.* 34, 2103976 (2022).

**Dixon, A.L.**, Vezin, H., Nguyen, T.Q., and Reddy, G.N.M. Structural insights into Lewis acid- and F4TCNQ-doped conjugated polymers by solid-state magnetic resonance spectroscopy. *Mater. Horizons.* 9, 981-990 (2022).

2021 Schopp, N., Brus, V.V., Lee, J., **Dixon, A.**, Karki, A., Liu, T., Peng, Z., Graham, K.R., Ade, H., Bazan, G.C., Nguyen, T.Q. Effect of Palladium-Tetrakis (Triphenylphosphine) Catalyst Traces on Charge Recombination and Extraction in Non-Fullerene-based Organic Solar Cells. *Adv. Funct. Mater*. 31, 2009363, (2021).

Du, Z., Mainville, M., Vollbrecht, J., **Dixon, A.L.**, Schopp, N., Schrock, M., Peng, Z., Huang, J., Chae, S., Ade, H., Leclerc, M., Reddy, G., Nguyen, T. Insights into Bulk-Heterojunction Organic Solar Cells Processed from Green Solvent. *Solar RRL*. 5, 2100213 (2021).

Nguyen-Dang, T., Harrison, K., Lill, A., **Dixon, A.**, Lewis, E., Vollbrecht, J., Hachisu, T., Biswas, S., Visell, Y., and Nguyen, T.Q. Biomaterial-Based Solid-Electrolyte Organic Electrochemical Transistors for Electronic and Neuromorphic Applications. *Adv. Ele. Mater.* **7**, 2100519 (2021).

2020 Huang, J., Lee, J., Vollbrecht, J., Brus, V.V., **Dixon, A.L.**, Cao, D.X., Zhu, Z., Du, Z., Wang, H., Cho, K., Bazan, G., Nguyen, T. A High-Performance Solution-Processed Organic Photodetector for Near-Infrared Sensing. *Adv. Mater*. 32, 1906027 (2020).

Karki, A., Vollbrecht, J., Gillett, A.J., Selter, P., Lee, J., Peng, Z., Schopp, N., **Dixon, A.L.**, Schrock, M., Nádaždy, V., Schauer, F., Ade, H., Chmelka, B., Bazan, G., Friend, R., Nguyen, T. Unifying Charge Generation, Recombination, and Extraction in Low-Offset Non-Fullerene Acceptor Organic Solar Cells. *Energy Environ. Sci*. 13, 3679–3692 (2020).

Huang, J., Lee, J., Schrock, M., **Dixon, A.L.**, Lill, A.T., Cho, K., Bazan, G.C., and Nguyen, T.Q. Large-gain low-voltage and wideband organic photodetectors via unbalanced charge transport. *Mater. Horizons.* **7,** 3234-3241 (2020).

Karki, A., Vollbrecht, J., Gillett, A.J., Xiao, S.S., Yang, Y., Peng, Z., Schopp, N., **Dixon, A.L.**, Yoon, S., Schrock, M ., Ade, H., Reddy, G., Friend, R., Nguyen, T. The role of bulk and interfacial morphology in charge generation, recombination, and extraction in non-fullerene acceptor organic solar cells. *Energy Environ. Sci*. 13, 3679-3692 (2020).

2019 Yurash, B., Cao, D.X., Brus, V.V., Leifert, D., Wang, M., **Dixon, A.**, Seifrid, M., Mansour, A.E., Lungwitz, D., Liu, T., Santiago, P., Graham, K., Koch, N., Bazan,

G., Nguyen, T., Towards understanding the doping mechanism of organic semiconductors by Lewis acids. *Nat*. *Mater. 18,* 1327–1334 (2019).

Karki, A., Vollbrecht, J., **Dixon, A.L.**, Schopp, N., Schrock, M., Reddy, G.N.M., and Nguyen, T.Q. Understanding the high performance of over 15% efficiency in single-junction bulk heterojunction organic solar cells. *Adv*. *Mater.* 31, 1903868 (2019).

***Presentations***

2022 "*Exciton Dynamics in Organic Semiconductors Modified with Lewis Acids*" and "*Light Upconversion via Triplet-Triplet Annihilation*", Center for Polymers and Organic Solids Seminar, Santa Barbara, United States

2018 "*Searching for chirality in a new route to heteroclite alkylphosphine oxides*", National Meeting of the American Chemical Society, New Orleans, United States

2017 "*Synthesis and Analysis of LaNi1-xMxO2 (M = Cu, Co) Possible Analog for Superconducting Cuprate*", Innovate UNO and University of Louisiana System Academic Summit, New Orleans, United States

***Awards & Honors***

2019 Phi Lambda Upsilon, National Honorary Chemical Society, United States

2017 Innovate UNO Poster Award 5th Place, United States

TABLE OF CONTENTS

## I. Introduction to Organic Semiconductors

In a society where technology is woven into multiple facets of daily life and an ever-increasing number of common items are being re-envisioned with touchscreens and light emitting diode (LED) displays, OSCs have sustained interest for their flexibility, lightweight and high degree of customizability thanks to the broad toolbox of organic chemistry. OSCs are molecules or polymers containing alternating carbon double and single bonds, known as π-conjugation. Single bonds are made up of relatively lower energy sigma (σ) bonds with maximal orbital overlap whereas double bonds contain one σ-bond in addition to one higher energy pi (π) bond which relies on less extensive lateral orbital overlap. Carbon atoms contain 4 valence electrons, 2 in the 2s-orbital and 1 in each of the $2p_x$ and $2p_y$ orbitals with an empty $2p_z$ orbital. In a conjugated system such as 1,3-butadiene the 3 σ-bonds are formed by the combination of $sp_2$-hybridized orbitals, leaving one pure $p_z$-orbital on each carbon atom to form the alternating π-bonds. The presence of adjacent $p_z$-orbitals allows for electron delocalization and charge transport across and between the conjugated segments.

One of the primary obstacles for organic semiconductors is their inherently low number of free charge carriers which limits their conductivity. Organic semiconductors are intrinsically insulating as promoting a molecule from the ground state to the excited state requires an electron in the highest occupied molecular orbital (HOMO) to absorb sufficient energy to enter the next highest orbital, the lowest unoccupied molecular orbital (LUMO). In organic semiconductors, this amount of energy is in excess of that provided by thermal energy at room temperature by 0.5 or as much as 2 eV.[1–4] To get around this, free charge carriers can be provided through charge injection at metal electrodes or chemical doping.

Enhancing the conductivity of OSCs through the addition of a small amount of specific chemical species, doping, has been one of the pivotal advancements in the development of high performance OSC devices. Additives which improve the conductivity of electrons are referred to as n-dopants. This type of doping is harder to achieve as the n-dopant needs to have a high HOMO energy level in order to donate an electron from its HOMO to the relatively high lying LUMO of an OSC material. This makes suitable n-dopants unstable in ambient air and vulnerable to reactions with oxygen. P-type doping is therefore much simpler with more stable dopants available. These dopants must possess a LUMO which is of lower energy than the HOMO of the OSC to allow the OSC to act as the electron donor, leaving it with a higher number of holes and thus greater hole conductivity. A simple schematic for these types of doping is shown in Figure 1.1.

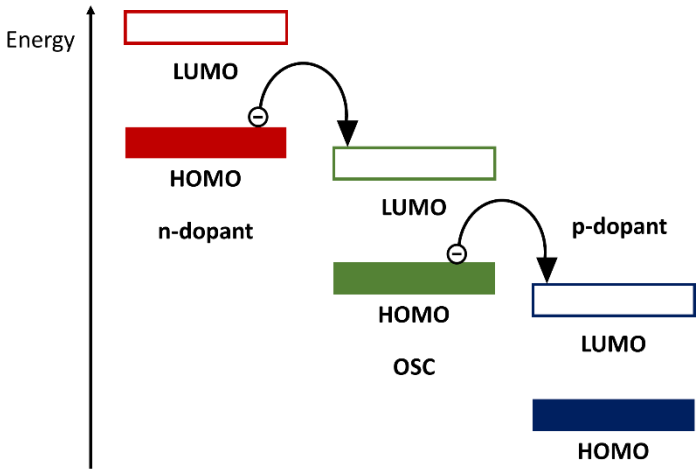


**Figure 1.1. Schematic of OSC doping indicating electron transfer from the dopant HOMO to the OSC LUMO (n-doping) and from the OSC HOMO to the dopant LUMO (p-doping).**

The two main OSC doping mechanisms result in the formation of either an ion pair (IP) via integer charge transfer or a charge transfer complex (CTC) through partial charge transfer. Integer charge transfer requires an electron to be transferred completely from the dopant to the

OSC, resulting in a dopant cation and an OSC anion in the case of n-doping and a dopant anion and a dopant anion and OSC cation in the case of p-doping. This can be represented by the simple model for doping shown in Figure 1.1. As organic semiconductors have low dielectric constants, the Coulombic forces between opposite charges are not screened effectively, providing an additional energy barrier of approximately 0.4 eV to any charge separation which occurs within them including dissociation of the ion pair.[5]

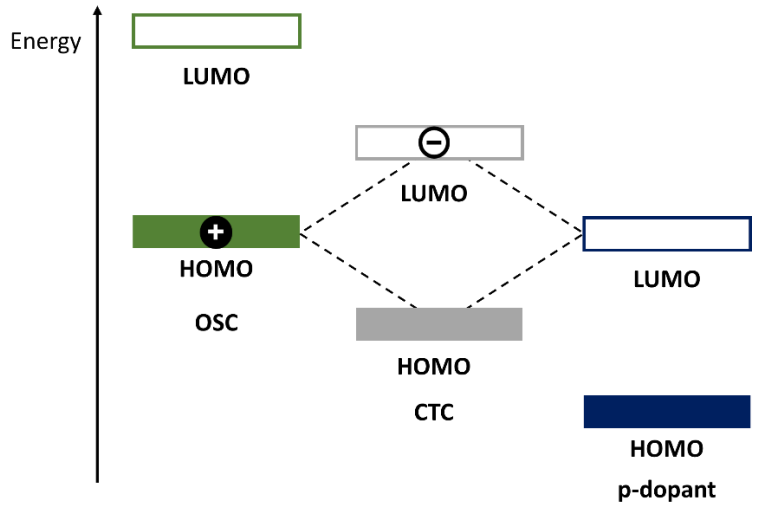


**Figure 1.2. Schematic of p-type OSC doping through the formation of a charge transfer complex (CTC). The LUMO of the p-dopant and HOMO of the OSC hybridize to form a LUMO and HOMO characteristic of the CTC. The CTC may then act as a dopant accepting an electron via integer charge transfer from a HOMO on another unit of the OSC.**

In the formation of charge transfer complexes, rather than complete charge transfer, the orbitals of the dopant and OSC mix to form new hybridized molecular orbitals (Figure 1.2). Notably, p-type CTCs can be formed when the LUMO of the dopant is lower or higher than the HOMO of the OSC and n-type CTCs can form when the HOMO of the dopant is higher or lower

than the LUMO of the OSC. The amount of orbital overlap and the magnitude of the difference in energy levels between the relevant orbitals of the dopant and OSC determine the extent of orbital hybridization and the magnitude of the gap between the resultant orbitals of the charge transfer complex ($LUMO_{CTC}$ and $HOMO_{CTC}$).[5–7] This form of doping can be less effective than IP formation as an additional step of integer charge transfer between one of the CTC orbitals and an orbital from the neutral OSC, in addition to overcoming the Coulombic attraction between the resulting charges in order to produce free charge carriers.[6]

One of the less commonly used doping strategies which is pertinent to the work contained in this thesis is Lewis acid doping. Our lab proposed a mechanism for this form of doping based on studies using the Lewis acid tris-(pentafluorophenyl)borane (BCF) and the polymer poly[2,6-(4,4-bis(2-hexadecyl)-4H-cyclopenta[2,1-b;3,4-b′]dithiophene)-alt-4,7(2,1,3-benzothiadiazole)] (PCPDTBT) which proceeds as follows. BCF readily forms a BCF•$H_2O$ complex with trace amounts of water which acts as a strong Brønsted acid, donating a proton to the CPDT unit. This results in a negatively charged $[BCF\text{-}OH]^-$ anion and a positive charge on the polymer backbone $[PCPDTBT\text{-}H]^+$. A neutral segment of the polymer chain then transfers an electron to the positively charged segment, producing a protonated radical $[PCPDTBT\text{-}H]^\bullet$ and a positively charged radical polymer segment $[PCPDTBT\text{-}H]^{\bullet+}$. It is this positively charged radical species which is proposed as the free charge carrier with the $[BCF\text{-}OH]^-$ anion serving as the counter-ion. In this study, BCF was shown to dope PCPDTBT more efficiently than the integer charge transfer dopant $F_4TCNQ$ and continued to be effective at higher dopant concentrations due to its better solubility in organic solvents commonly used in OSC processing.[8–11] Chapter 4 of this thesis includes our subsequent investigation of the intermolecular arrangements of BCF and $F_4TCNQ$ different dopants when blended with PCPDTBT which allowed us to gain a deeper

understanding of the structural factors which contribute to their differences in doping efficiency and concentration-dependent doping performance.[12]

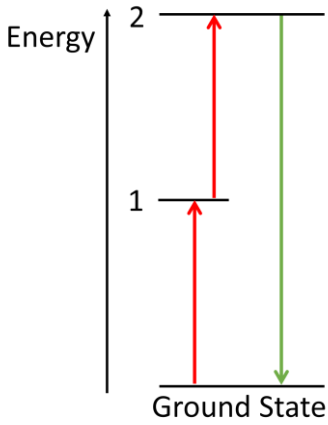


**Figure 1.3. General diagram for photon upconversion in which excitation into excited states 1 and 2 can be provided either by light absorption or energy transfer processes. The ultimate result is the emission of light which is of a higher energy than that provided in either of the individual energy absorption steps.**

OSCs are, of course, not only attractive for their tunable electronic properties, but also for interesting optical applications such as photon upconversion which allows low energy light absorption to be converted into higher energy light emissions. A general schematic for upconversion is shown in Figure 1.3. A molecule in the ground state will first absorb energy either from light absorption or an energy transfer process from a separate molecule in order to reach a first excited state energy level. Subsequent energy absorption either through optical excitation or energy transfer allows a molecule to reach a second higher excited state energy level. When a molecule in the second excited state decays radiatively to the ground state, it emits light which is higher in energy than either of the individual amounts of energy absorbed. While

there are a variety of mechanisms for upconversion, Chapter 3 of this thesis focuses on photon upconversion via triplet-triplet annihilation.[13,14]

It is important to note that upconversion is distinct from two-photon absorption which requires coherent excitation from lasers with high power densities on the order of $10^6$ W $cm^{-2}$ to allow two photons to be absorbed simultaneously.[15] In contrast, upconversion processes can proceed with excitation from lower energy incoherent lasers and even sunlight with excitation power densities on the scale of 100 mW $cm^{-2}$, making them attractive for incorporation in organic photovoltaics to enable lower energy light to be harvested without needing to alter the absorbance range of the materials in the active layer.[16–18] Upconverting light emitting diodes (LEDs) have also been developed and even paired with a photosensitive organic field effect transistors (OFETs) to enable pixel-free infrared imaging.[17–20] The basic operating principles of OLEDs, OFETs and OPVs are discussed below.

### *A. Organic Light Emitting Diodes*

The average person is currently most likely to come into contact with OSCs in the form of organic light-emitting diodes (OLEDs) in digital display panels or lighting fixtures. To summarize the operation of OLED devices, electrons and holes are injected at metal contacts, then travel through layers of organic material where they encounter each other and combine to release energy in the form of light. Benefits offered by OLEDs over their inorganic counterparts include a wider color range and viewing angle, higher contrast, faster response times, brighter, thinner and flexible devices with lower power consumption and the ability to operate in a wider range of temperatures. OLEDs also achieve true black by turning off pixels, something not accessible for inorganic LEDs which utilize backlighting panels, resulting in small amounts of

remnant light emission at any pixel. In order to make the utilization of OLEDs more attractive for the lighting and display market, advancements still need to be made in device encapsulation to prevent degradation in ambient air, solution-processing techniques to bring down manufacturing costs, and materials development or device design in order to improve upon the relatively low device efficiencies.

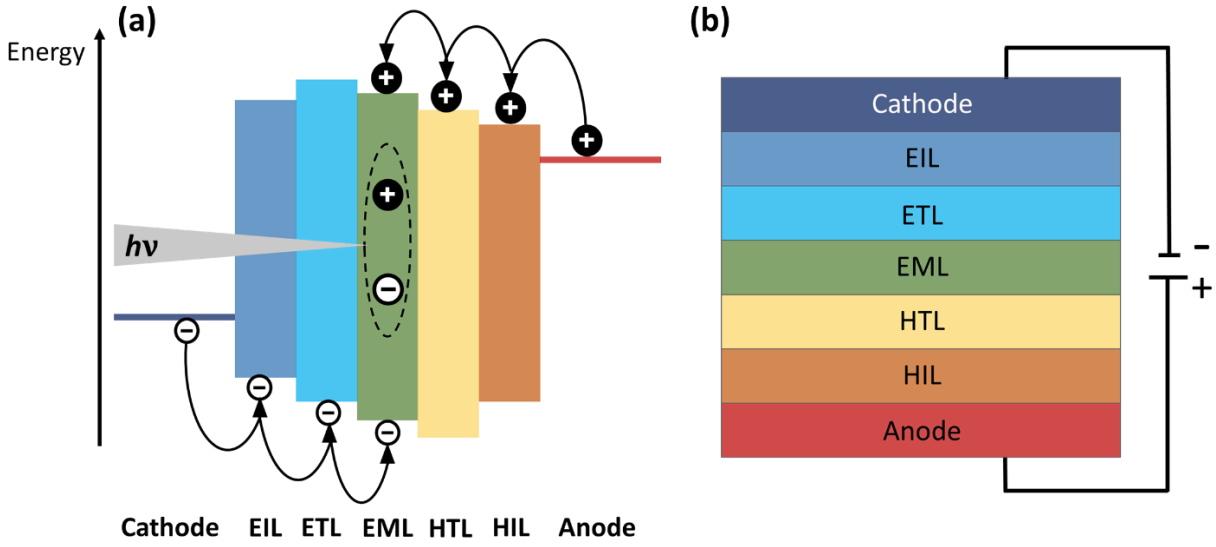


**Figure 1.4. a) Energy diagram illustrating OLED working principle adapted from ref. 21. Electrons flow into the electron injection layer (EIL) from the negatively biased cathode while holes flow into the hole injection layer (HIL) from the positively biased anode. Charges then enter the electron/hole transport layers (ETL/HTL) and recombine into excitons in the emissive layer (EML) which decay radiatively to the ground state, emitting light. b) Schematic of an OLED device.**

The general OLED energy diagram and schematic for modern devices is shown in Figure 1.4 A negative bias applied at the cathode causes electrons to flow into the electron-injection layer (EIL) while a positive bias at the anode draws holes into the hole injection-layer (HIL). These injection layers are used to prevent charge accumulation at the metal-organic contact and reduce the probability of charge recombination as well as the driving voltage required to move charges farther into the device. The hole-injection layer is chosen to provide a more favorable energetic

pathway for holes to transfer between the Fermi level of the anode and the deep-lying HOMO of the hole-transport layer (HTL). The electron-injection layer is likewise chosen to promote electron flow between the relatively high LUMO of the organic electron transport layer with the Fermi level of the cathode. The choices for cathode materials are more limited as they must be "low work function" material from which electrons can easily be removed, making most options such as alkali metals reactive to air, water and organic materials. Oxidation at the outer surface of the cathode has been diminished by the use of capping layers while mitigation of oxidation at the cathode-organic interface is another purpose served by the electron-injection layer.[22]

In order to efficiently radiatively combine electrons and holes in the emissive layer, charges are funneled through selective charge transport layers. Optimizing the orbital energy levels for the materials serving as injection layers is rather straightforward in comparison to the more complicated factors governing charge transport in organic semiconductors. As a reminder, charges in OSCs are delocalized over conjugated segments, making charge transport in these materials dependent upon thermally activated hopping between the HOMOs and LUMOs of neighboring segments. Some of the important considerations in promoting charge transfer in OSCs include intermolecular packing and orientation, orbital overlap and the associated reorganization energies. The tendency of organic semiconductors to have higher hole than electron mobilities limits the number of material options available for electron-transport layers but also highlights the importance of these layers for populating the emissive layer with a sufficient number of electrons. Conveniently, both transport layers serve as blocking-layers for the opposite charges which helps to confine charge recombination to the emissive layer.

The initial design of the emissive layer in OLEDs was rather simple: a homogeneous layer of emitter molecule. One of the first major improvements in OLED device efficiency was to

incorporate a much smaller amount of emitter molecule as a dopant in the emissive layer which was primarily composed of a host matrix. Choosing a host matrix with good energetic alignment to both the LUMO of the electron-transporting layer and the HOMO of the hole-transporting layer resulted in more efficient charge transfer from the transporting layers, concentration of the resulting Coulombically bound electron-hole pairs also known as “excitons”, and a reduction in self-quenching between emitter molecules.

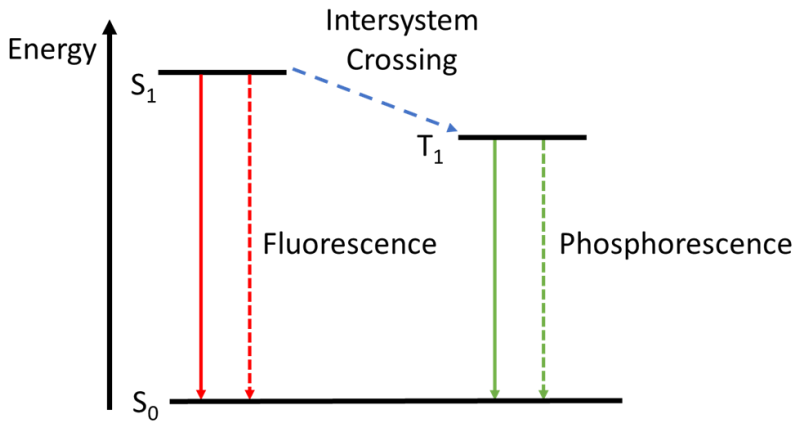


**Figure 1.5. Radiative (solid lines) and non-radiative (dashed lines) transitions available to singlet ($S_1$) and triplet ($T_1$) excitons. The ground state is indicated by $S_0$.**

OLED devices can be divided into groups based on the type of photoluminescent transitions which occur in their emissive layers. First generation devices are based on fluorescence, second generation devices are based on phosphorescence, and third generation devices are based on thermally activated delayed fluorescence. The different emission pathways are shown in Figure 1.2. First generation devices are limited by the spin statistics of exciton formation since there is only a 25% chance of generating the singlet state from which fluorescence occurs. In singlet excitons, the electron spins are both anti-parallel and 180° out-of-phase, while those of triplet excitons are parallel and in phase. There is only one orientation which produces a singlet exciton (25% chance of formation) while there are three orientations available to triplets (75% chance of formation). Another interesting aspect to consider is that there is no ground state for triplet excitons. In the case of photon absorption, molecules in the singlet ground state absorb light to access the singlet excited state. Since photons absorption cannot induce a change in spin orientation, $S_0$ to $T_1$ transitions are considered forbidden. However, individual charges injected

into these OLED devices have random spins, meaning that their resulting excitons are determined by spin statistics, not the rules of optical transitions, producing a minority of singlets.

Harvesting triplet excitons in OLED devices began with the use of phosphorescent emitters in second generation devices, resulting in a greater internal quantum efficiency (IQE) which is the ratio of photons generated within the device to injected charge carriers. In fact, these devices achieved nearly 100% IQE with phosphorescent emitters containing heavy metals such as Ir and Pt.[23,24] These metals exhibit strong spin-orbit coupling which facilitates the forbidden spin flip required to complete intersystem crossing, converting nearly all singlet excitons into the desired triplets for phosphorescence. Of course, these devices also have their own drawbacks. Singlet excitons tend to decay to the ground state within picoseconds while triplet excitons can take microseconds. In this extra time, triplet excitons can travel through the emissive layer and engage in other reactions decreasing the device efficiency such as triplet-triplet and triplet-polaron annihilation.[25,26]

Third generation OLED devices turn these triplets back into fluorescent singlet excitons through the process of reverse intersystem crossing (RISC). The additional energy transfer step results in a delay before the observed fluorescence, thus these molecules are known as thermally activated delayed fluorescence (TADF) emitters. Instead of relying on the spin-orbit coupling of heavy-metals, sophisticated design principles can be used to produce TADF molecules which have a very small (< 100 meV) difference between the $S_1$ and $T_1$ energy levels.[27–29] This represented another significant breakthrough in the external quantum efficiencies (EQE) for fluorescent OLEDs which were previously limited to 5%. TADF emitters enabled EQEs of around 30% for red, green and blue emitting devices.[30]

### *B. Organic Field-Effect Transistors*

Transistors are key components of electronic devices, acting as signal amplifiers or switches to convey binary information by alternating between on and off states. Inorganic transistors based on crystalline silicon have the advantage of faster switching speeds and higher packing densities. Organic field-effect transistors (OFETs) offer advantages of biocompatibility (an important aspect considering the interest of using these components in bioelectronics and biosensors), low-cost solution processing, flexibility, and low power consumption.[31,32] Applications for OFETs have included gas, humidity, heat, chemical, pressure and pH sensing as well as controlling OLEDs, non-volatile computer memory and artificial synapses.[33–39]

OFETs are composed of an organic semiconducting layer with a source and drain electrode at opposite ends and an insulating dielectric layer separating the organic semiconductor from the gate electrode. A general schematic for the conventional OFET device is shown in the lower panel of Figure 1.6 with either electrons or holes as the dominant charge carrier producing current. Based on the relatively higher mobility of holes in OSC materials, there are more options available for p-type devices with holes as the majority charge carrier (Figure 1.6 d) although n-type (Figure 1.6 e) and ambipolar devices do exist. [31,40] OFET devices are said to operate in charge accumulation mode with charges injected into the semiconductive active layer, rather than depletion mode in inorganic transistors. This is because OSCs have inherently low numbers of free charge carriers and such carriers also cannot be generated by thermal energy at room temperature. In a p-type OFET, applying a sufficiently negative voltage bias between the source and drain will eventually result in only a small current to flow in the space between the contacts, referred to as the channel. The negative bias needs to be sufficiently large in order to draw out enough charge carriers to fill the trap states before charges can move freely through the

channel, this minimum voltage for current flow is the threshold voltage ($V_T$). Utilization of the gate electrode allows larger currents to be achieved. Applying a negative bias between the gate and the source ($V_G$) in this same OFET will draw holes into the HOMO of the OSC within the active layer (Figure 1.6 a), leading to their accumulation at the semiconductor-dielectric interface. Then, application of a negative bias greater than $V_T$ between the source and drain electrodes ($V_{DS}$), will result in current flow between the source and drain which is larger by orders of magnitude than in the absence of $V_G$ (Figure 1.6 d).

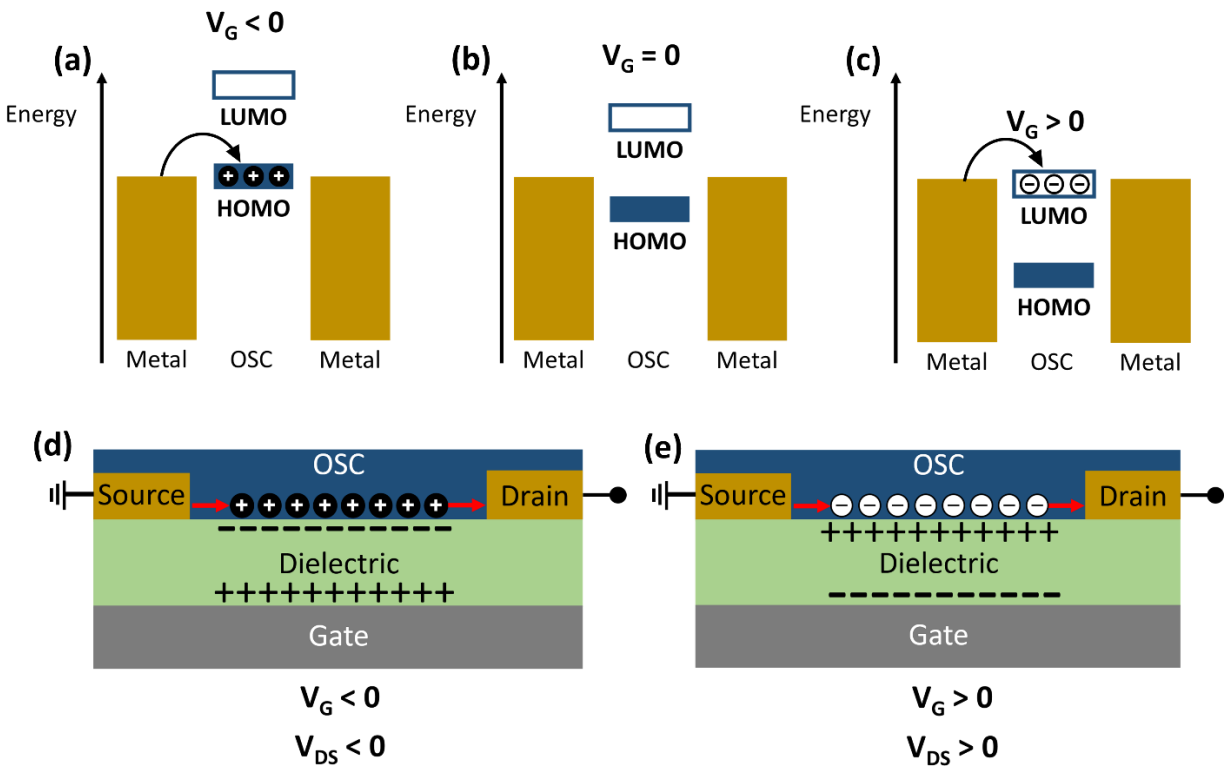


**Figure 1.6. Energy diagram showing a) hole injection from a metal contact into the HOMO of a p-type OSC active layer with a negative gate voltage ($V_G$), b) no charge injection when $V_G = 0$, and c) electron injection into the LUMO of a n-type OSC active layer with a positive gate voltage adapted from ref. 41. Device schematics show the charge distribution within the dielectric which changes to d) stabilize the positive charges accumulated within the OSC under a negative $V_G$ and the flow of holes from the source to the drain due to the negative bias between these contacts ($V_{DS}$) in a p-type device, as well as the n-type device operation in which the negative charges in the OSC are stabilized by the dielectric under a positive $V_G$ and the electrons flow to the drain when a positive $V_{DS}$ is applied.**

In order to switch quickly between the on and off states of the OFET, high field-effect mobilities are required. Reducing the amount of defects in the semiconducting material or enhancing its degree of organization are useful in increasing the mobility. Increased order and crystallinity can limit the flexibility of the device overall, thus mobility enhancements for flexible OFETs have been achieved through the addition of species such as conjugated carbon nanorings or elastomers into polymers.[42] Since flexible batteries are currently limited to a voltage

of around 2V, there is also interest in lowering the operating voltage of OFETs. Using materials with high dielectric constants (κ) can help lower the operating voltage, often at the expense of charge carrier mobility as charges can become trapped at the interface between the OSC and the high κ dielectrics.[31] Methods to simultaneously achieve both goals include utilization of parylene films as the dielectric layer and bilayer dielectric designs combining organic materials with aluminum oxides.[43–45] The aluminum oxide dielectric layers offer higher capacitance as well as a high degree of homogeneity and lower surface trap densities. These properties also contribute to lowering the threshold voltage and decreasing the amount of current which leaks out od the device while in the off state, resulting in a high on/off current ratio which is favorable for OFET devices.[45]

### *C. Organic Photovoltaics*

When integrating renewable energy generation into designs such as those of a building or wearable technology, lightweight and tunable organic photovoltaics (OPVs) arise as prime candidates. These devices convert absorbed light energy into electricity using four main components: an anode, a donor and an acceptor OSC material located in the active layer, and a cathode. The wavelengths of light which can be utilized by a specific device is determined based on the energetic gap between the LUMO and HOMO of the materials within the active layer. As OSC energy levels can be modulated synthetically or with post-processing additives, solar cells can be produced which absorb energy from a select region of the solar spectrum, enabling selectively transparent or colored devices.[46–52] When photons of suitable energy enter the active layer of the OPV, an exciton is formed which must travel to the donor/acceptor interface to split into separate charges. The relative HOMO and LUMO energies of the donor and acceptor

materials are important in promoting this charge separation. The donor material should have a LUMO energy higher than that of the acceptor while the acceptor materials should have a HOMO energy below that of the donor, facilitating electrons hopping to lower energy states and holes hopping to higher energy states. With the help of an applied electric field, electrons are swept through the acceptor material to the cathode while holes are swept through the donor material to the anode.

The main performance metric for these devices is the power conversion efficiency which describes how effectively the light incident upon the OPV is converted into electric energy. Some of the highest performing OPV devices have utilized an active layer structure in which the donor and acceptor materials are blended together to form a bulk heterojunction (BHJ).[53,54] The current world record holding OPV reached a power conversion efficiency of 18% using four components in a BHJ active layer.[55] With OPV active layers typically 100-200 nm thick for strong absorption and exciton diffusion limited to about 10 nm, the multiple interfaces for charge separation in BHJ devices offer a great advantage for efficiency over planar heterojunction devices with their singular continuous interface.[56–58] Figure 1.7 shows an energy diagram illustrating the OPV working principle and a general schematic of a BHJ OPV device. It is possible to create charge islands in BHJ devices if the active layer is made too thick or if the domains of donor or acceptor material are made too small, reducing the number of percolation pathways for either charge carrier to the electrodes. Even if there are only domains of donor materials holding trapped holes, this can diminish the number of electrons extracted as nearby electrons can be attracted by those positive holes and recombine, lowering the device efficiency. Large domains and active layers which are too thin will reduce the area available for charge

separation, also diminishing the efficiency.[59–61] Thus, controlling the domain size and active layer thickness are necessary to reap the benefits of the BHJ active layer design.

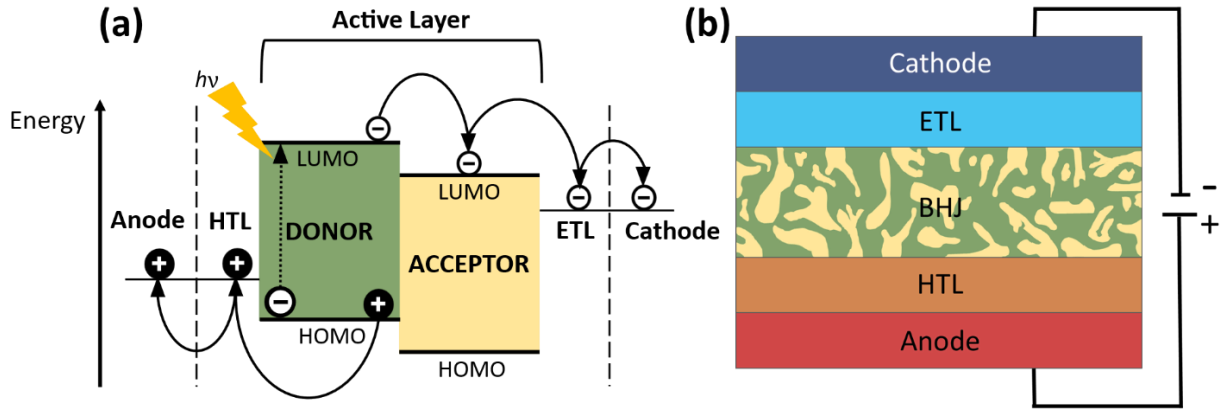


**Figure 1.7 a) Energy diagram illustrating OPV working principle adapted from ref. 21. Photons incident upon the active layer provide the energy needed to promote an electron from the HOMO to the LUMO, leaving behind a positively charged hole in the HOMO. These charges bound by Coulombic forces make up the exciton which diffuses to a donor/acceptor interface for charge separation. With the aid of an applied electric field, these charges are swept through the transport layers and ultimately to their respective electrodes. b) Schematic of bulk heterojunction OPV device.**

Despite the aid of the applied electric field in charge extraction, the typical low charge carrier mobilities in organic semiconductors can also limit device performance and contribute to the limitations on active layer thickness. Furthermore, the magnitude of the applied electric field is influenced by the choice of the electrodes, which is likewise guided by the energy levels of the OSCs used in the active layer. Of course, the OSCs themselves may contain impurities which can trap charge carriers or otherwise diminish device performance. The degree of order and type of organization within the OSC may also influence charge transport in the active layer as charges hop between sufficiently close conjugated segments. Depending on the innate properties of the OSC as well as the substrate and active layer processing conditions, these conjugated segments may be stacked parallel or perpendicular to the electrodes, a mixture of these and other orientations, or completely disordered, with those morphologies aligning the conjugated backbones in stacks pointing towards the electrodes favorable for device performance.

## II. Experimental Methods

### *A. Design of Ternary Photon Upconversion System*

The TADF materials, 4CzIPN and 2,4,5,6-tetrakis(3,6-dibromocarbazol-9-yl)isophthalonitrile (4CzIPN-Br), were synthesized according to the literature procedures.[62,63] P-terphenyl, naphthalene and 1-methylnaphthalene were purchased from Acros-Organics; fluorene, pyrene, and 2-5-diphenyloxazole (PPO) were purchased from Sigma-Aldrich and all used as received. Air-stable powder stock materials such as p-terphenyl were stored outside of the glovebox. All samples were prepared in the nitrogen atmosphere of a glovebox and sealed in quartz cuvettes prior to measurements. Absorption measurements were performed on a Perkin Elmer Lambda 750 VU-vis/NIR spectrometer. Steady-state fluorescence spectra of emitter molecules were obtained using a Horiba PTI QuantaMaster fluorimeter.

1. Photoluminescence Lifetimes

Time correlated single photon counting (TCSPC) was conducted to observe the delayed fluorescence from 4CzIPN. Solution samples were excited with a Ti:Sapphire laser (Coherent Mira 900) with a 200 fs pulse width. The 800 nm fundamental frequency was doubled to obtain a 400 nm excitation wavelength using an Inrad 9300 second harmonic generator. The detection wavelength was determined by the wavelength of maximum emission intensity. A homemade acousto-optical pulse picker was used to reduce the repetition rate of the laser, crucial for avoiding saturating the sample with excited-state chromophores. An Advanced Micro Devices avalanche photodiode served as the single-photon detector with the detection wavelength set to 960 nm for the acceptor and 760 nm for the donor. Attenuation of the laser beam ensured that

each pulse produced fewer than $3 \times 10^{11}$ excitons $cm^{-2}$ (corresponding to an energy density of 500 $pJcm^{-2}$).

2. Photon Upconversion Measurements

Upconversion experiments were performed using 457 nm excitation from an $Ar^+$-ion laser (Spectraphysics Beamlok 2060-8). For measurements not used for $\eta_{UC}$ calculations, the beam was directed onto a 10 mm quartz cuvette, the incident laser power was measured directly in front of the sample, and the upconverted photoluminescence was measured at 90° relative to the laser beam. The intensity of the incident laser beam was attenuated using a series of neutral density filters (Appendix Figure 7.1). A bandpass filter (Schott UG-11, 3 mm thick) was used to block the residual sensitizer photoluminescence and laser from reaching the charge-coupled device (CCD) detector. The threshold light intensity ($I_{th}$) for efficient TTA for each sample was determined by the excitation intensity dependence of the integrated upconverted photoluminescence. The $I_{th}$ is discussed in more detail in the results section.

The setup for the referenceless measurement of the photoluminescence upconversion quantum efficiency is shown in Figure 2.1. The output of the $Ar^+$-ion laser at 457 nm was directed into the 25.4 cm diameter, Spectrolone-coated integrating sphere (Labsphere). The laser beam was passed through a bandpass filter with 10 nm FWHM transmission band to remove plasma emission spectral lines. The beam was focused at the sample position inside the sphere with a lens with 25 cm focal length. The sample solution was placed into a quartz cell with 1 mm optical path length and screw-on cap ensuring hermetical seal. The sample was tilted by ~7° relative to the laser beam to avoid back reflection of the laser beam. Upconverted photoluminescence produced in the cell was detected through the sphere's output port located at

90° angle relative to the excitation laser beam and screened by a baffle from the direct emission from the sample. 25 mm focal length relay lens imaged the output of the sphere on the input of a Cherny-Turner spectrometer (PI/Acton Research SP2358) with a CCD camera detector (Andor iDus 401OE). To attenuate the visible photoluminescence and intense laser light, the bandpass filter (Schott UG-11, 3 mm thick) was placed in front of the spectrometer.

The spectral response of the setup was calibrated in a 2-step process. First, a light from the radiometrically calibrated light source (Ocean Optics DH-MINI) was injected into the integrating sphere and the spectrum was recorded with a CCD camera. The spectrometer grating was set so that the CCD camera could acquire the UV photoluminescence emission of the sample in a single shot. The relative system sensitivity curve was determined by dividing the actual light source spectrum by the recorded one: $S(\lambda) = I_a(\lambda)/I_m(\lambda)$. Second, to obtain the absolute sensitivity curve for the setup, a light with known power from a 361 nm laser was injected into the sphere. Taking into account that:

$$A \int I_{las}(\lambda) S(\lambda) d\lambda = \frac{P\lambda}{hc}, \quad (1)$$

where A is a constant, $I_{las}(\lambda)$ is the recorded spectrum of the laser light, P is the power of the light injected into the sphere, $\lambda$ is the light wavelength, h is the Planck constant, and c is the speed of light, the calibration constant was determined as:

$$A = \frac{P\lambda}{hc \int I_{las}(\lambda) S(\lambda) d\lambda}. \quad (2)$$

Then, the total number of photons emitted by the sample from the photoluminescence spectrum recorded with the CCD camera was calculated as:

$$N_{em} = A \int S(\lambda) I_{PL}(\lambda) d\lambda. \quad (3)$$

The number of photons absorbed from the excitation laser beam was found using UV-Vis absorption spectra of samples collected using a spectrophotometer (Perkin Elmer Lambda 750):

$$N_{abs} = \frac{(1-10^{-OD(457)})P_{457}\lambda}{hc}, \quad (4)$$

where OD(457) is the sample optical density and $P_{457}$ is the laser power at 457 nm, respectively. In our experiments, we assumed that only single pass absorption of the laser light contributed to the photoluminescence upconversion, and the laser light scattered from the sphere after passing through the sample did not produce UV photoluminescence.

The quantum yield of the upconverted photoluminescence was found as a ratio of (3) and (4):

$$QY = \frac{N_{em}}{N_{abs}}. \quad (5)$$

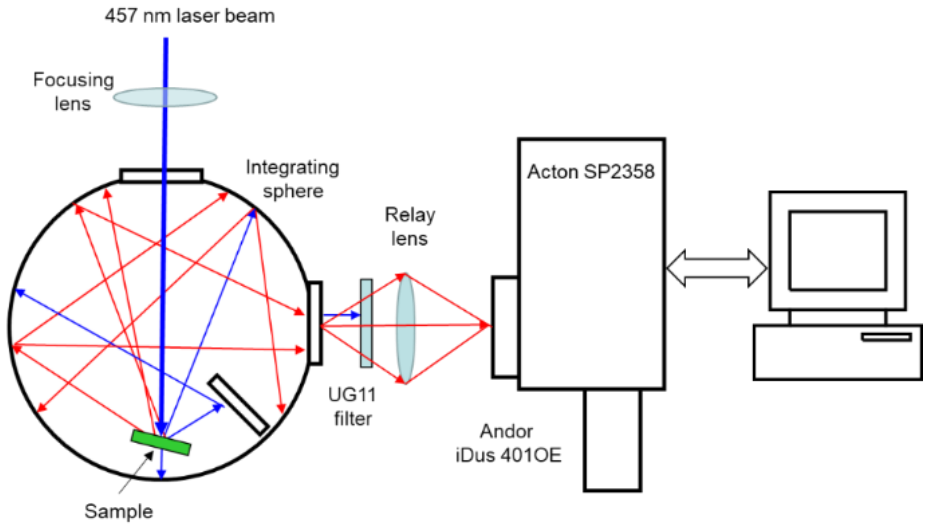


**Figure 2.1. Setup for the referenceless determination of the photoluminescence upconversion quantum efficiency.**

In measuring the absolute photoluminescence quantum yield of upconversion, one must also consider the impact of reabsorption of the emitted upconverted light by the sample.[64] Thus, we compared the transmission of the Ocean Optics DH-MINI through the empty integrating sphere with that of the 1mm cuvette filled with the benzene solvent and each of the upconversion

samples. The cell was positioned inside the sphere so that the incident light did not hit the cell directly. As shown in the appendix (Figure 7.8), the UV-spectrum absorbance due to the samples themselves was negligible when compared to the benzene solvent. We observed that the decrease in transmission intensity was caused by the light absorption by the cell and solvent. Further, the reabsorption correction coefficient was calculated using the following expression in which $T_S(\lambda)$ was the transmission coefficient spectrum of the setup with the sample.

$$K_{RA} = \frac{\int I_{PL}(\lambda)d\lambda}{\int T_S(\lambda)I_{PL}(\lambda)d\lambda} \quad (6)$$

The reabsorption correction factors are also shown in the appendix (Figure 7.2). Although these values are rather consistent between each sample and the solvent itself, the corrected QY value can be calculated by multiplying QY by $K_{RA}$.

Each editorial page has a major asset in the fact that it is one of a series, just one link in a long chain of events. It must take advantage of that asset by making sure that its outline is as regular as possible, in order to contrast with the irregular perimeter of the ads.

***B. Solid-State Magnetic Resonance Study of Doped Polymer Morphology***

1. Materials, Synthesis and Deposition

The polymer poly[2,6-(4,4-bis(2-hexadecyl)-4H-cyclopenta[2,1-b;3,4-b′]dithiophene)-alt-4,7(2,1,3-benzothiadiazole)] (P4) was purchased from commercial suppliers, and neat P4 and P4:dopants at indicated molar ratios were prepared according to the procedure described in 1-Material, tris(pentafluorophenyl)borane (BCF) was purchased from TCI America and F4TCNQ was purchased from Lumtec and all were stored in a nitrogen glovebox and used as received. Stock solutions of the dopants (10 mg/ml BCF, 0.2 mg/ml F4TCNQ in chloroform) were

prepared and then added in the proper ratio to solutions of P4 which was also dissolved in chloroform. The solutions of the doped polymer were allowed to sit overnight before being sealed under nitrogen in an airtight sample holder for drying via rotary evaporation at room temperature. The rotary evaporator was purged 3 times with nitrogen before opening the valve connecting the sample to the vacuum of the rotary evaporator. Once dry, the sample holder was filled with nitrogen again before being brought into the glovebox where the material was scraped into clean vials prior to the ssNMR measurements.

2. Solid-state NMR and EPR Spectroscopy

All solid-state NMR and EPR experiments were carried out at high field NMR facility at University of Lille, France. Pristine P4, P4:BCF (1:0.05, 1:0.2, and 1:1 molar ratios) and P4:F4TCNQ (1:0.02 and 1:0.2 molar ratios) were separately packed into either 1.3 mm (outer diameter) or 3.2 mm (outer diameter) cylindrical zirconia rotors and fitted with Vespel® caps. All fast MAS (50 KHz) 1D $^{1}$H, $^{19}$F, and 2D $^{1}$H-$^{1}$H and $^{19}$F-$^{19}$F NMR experiments were carried out on a Bruker AVANCE NEO (18.8 T, Larmor frequencies of $^{1}$H, $^{13}$C, $^{11}$B and $^{19}$F were 800.1 MHz, 201.2 MHz, 256.7 MHz and 752.8 MHz respectively) spectrometer with 1.3 mm H-X probehead unless otherwise stated. The $^{1}$H and $^{13}$C experimental shifts were calibrated with respect to neat TMS using adamantane as an external reference (higher ppm $^{13}$C resonance, 35.8 ppm, and the $^{1}$H resonance, 1.85 ppm), and $^{19}$F chemical shifts were calibrated to the $^{19}$F chemical shift of Teflon at −132 ppm, in turn calibrated using neat $CFCl_3$ ($^{19}$F, 0 ppm) as an external reference. The $^{11}$B chemical shifts are referenced to $^{11}$B peak (-42.06 ppm) using an external standard $NaBH_4$, which is calibrated to $BF_3.OEt_2$ ($^{11}$B, 0 ppm) in $CDCl_3$.

***1D MAS NMR experiments.*** – For all materials, single-pulse $^{1}$H MAS NMR experiments were carried out by co-adding 32 transients. $^{1}$H relaxation delays were of 3 s and 2 s for the neat P4 materials and P4:dopant blends, respectively. In all cases, the $^{1}$H and $^{19}$F $T_1$ relaxation delays were measured by saturation recovery experiments and analysis. All 1D $^{1}$H→$^{13}$C cross polarization (CP)-MAS experiments of neat materials and blends were carried out at Bruker 9.4 T spectrometer (Larmor frequencies were $^{1}$H = 400 MHz, and $^{13}$C = 100.6 MHz). $^{1}$H→$^{13}$C CP-MAS spectra of P4, P4:BCF (1:1) and P4:F4TCNQ (1:0.2) were acquired by co-adding 4096, 16384, 20480 transients, respectively, with a CP contact time of 4 ms. Heteronuclear decoupling was applied during the acquisition period using two-pulse phase modulation (TPPM) decoupling sequence.[65] For F4TCNQ and P4:F4TCNQ blends, 1D $^{19}$F MAS experiments were acquired using a spin-echo sequence with an echo delay corresponding to one rotor period. For neat BCF and P4:BCF blends, 1D $^{11}$B experiments were carries out at 18.8 T with 20 kHz MAS using a spin-echo sequence with an echo delay corresponding to one rotor period. For P4:BCF+water and P4:BCF+$D_2O$ titration experiments, ~20 µl of Millipore water or $D_2O$ was added to 9 mg of blend materials and allowed to set at room temperature. 1D $^{1}$H and $^{11}$B MAS NMR experiments of these materials were separately carried out for P4:BCF+water and P4:BCF+$D_2O$ blends.

***1D lineshape analysis. –*** $^{1}$H lineshape analysis was carried out using Bruker Topspin (sola) package. For neat P4 and P4:dopant blends and P4:BCF+water blends, the $^{1}$H signals correspond to aliphatic, water and aromatic sites were deconvoluted in order to estimate the peak integrals, which are compared in Table 7.1.

***2D MAS NMR experiments***. – 2D $^{1}$H-$^{1}$H DQ-SQ correlation spectra were acquired using a one rotor period Back-to-Back (BaBa) sequence with fast MAS,[66–68] 2D $^{1}$H-$^{1}$H DQ-SQ spectra of neat P4 material, P4:F4TCNQ and P4:BCF blends were acquired using 128 $t_1$ increments, each

by co-adding 16 transients with a rotor-synchronized $t_1$ increment of 20 μs. 2D $^{1}$H-$^{13}$C heteronuclear correlation (HETCOR) spectrum of neat P4 was acquired with 128 $t_1$ increments, each with 16 co-added transients, to evolve the indirect $^{13}$C dimension using STATES-TPPI method. 2D $^{19}$F-$^{19}$F spin-diffusion experiments were carried out using a three-pulse NOESY-like sequence,[69–71] using 80 $t_1$ increments, each by co-adding 16 transients with a rotor-synchronized $t_1$ increment of 20 μs.

## III. Design of Ternary Photon Upconversion System

This chapter presents research published in Ref. **14**. The research presented herein details the design and characterization of a novel three-component system for photon upconversion. I would like to thank Dr. Brett Yurash and Carolina Espinoza for the foundational work on this research determining which molecules to include in the upconversion system and a comparison between the emitter molecule 4CzIPN and a brominated form, 4CzIPN-Br. My contributions in identifying the optimal molecular ratios and characterizing the upconversion system would not have been possible without Dr. Alexander Mikhailovsky's instruction and assistance in troubleshooting measurements in his optical lab. I also must thank Dr. Yurash and my lab mate Sangmin Chae immensely for performing the measurements presented in appendix figures 7.1-7.3 and 7.5 and composing the discussion of those results to address reviewer questions while I was away from lab following my mother's passing.

As in many fields, the most exciting endeavors in photon upconversion research focus on increasing the efficiency (upconversion quantum yield) and performance (anti-Stokes shift) while diminishing the cost of production. In this vein, studies employing metal-free thermally

activated delayed fluorescence (TADF) sensitizers have garnered increased interest. Here, for the first time, the strategy of ternary photon upconversion was utilized with the TADF sensitizer 4CzIPN, resulting in a doubling of the upconversion quantum yield in comparison to the binary system employing p-terphenyl as the emitter. In this ternary blend, the sensitizer 4CzIPN is paired with an intermediate acceptor, 1-methylnaphthalene, in addition to the emitter molecule, p-terphenyl yielding a normalized upconversion quantum yield of 7.6 % while maintaining the 0.83 eV anti-Stokes shift. These results illustrate the potential benefits of utilizing this strategy of energy-funneling, previously used only with heavy-metal based sensitizers, to increase the performance of these photon upconversion systems.

### *A. Introduction*

The process of photon upconversion through triplet-triplet annihilation (TTA-UC) allows higher energy light to be emitted after lower energy light is absorbed. This process has been utilized in varied applications such as forensic and in situ-biological imaging, temperature and mechanical stress sensing, as well as solar energy generation.[27,72–75] TTA-UC has gained great attention because it can proceed efficiently at low threshold intensities of incident incoherent light at or below 100 mW $cm^{-2}$.[72,76,77] This phenomenon was first discovered in single molecules of anthracene and phenanthrene as early as 1962,[78] continued research has produced increasingly efficient TTTA-UC systems and revealed the ease of tuning optical properties in multi-component systems.[28,79,80] The first step in multi-component triplet upconversion is photon absorption by a sensitizer molecule, resulting in the generation of a singlet excited state, $S_1$ **(Figure 3.1a)**. It converts to the triplet excited state ($T_1$) through intersystem crossing (ISC) and is then donated to an acceptor molecule through triplet energy transfer (TET). The collision of

two triplets on the acceptor initiates the TTA process, resulting in one higher energy $S_1$ state on one acceptor molecule from which light is emitted (while the other decays to the ground state). Thus, emission from that $S_1$ state results in higher energy light than what was used for the excitation energy. There has been some confusion in the literature on how upconversion efficiencies are reported. Sometimes they are reported as the absolute efficiency (50% theoretical maximum), while others have chosen to normalize the efficiency to the 50% theoretical maximum, resulting in efficiencies of upconversion that can range from 0% to 100%. As suggested by Zhou et al., we will indicate the efficiencies normalized to 50% as $\eta_{UC}$.[81] The relationship between the absolute quantum yield, $\Phi_{UC}$, and the normalized upconversion efficiency, $\eta_{UC}$, is given in Equation (7)

$$\eta_{UC} = 2 \times \Phi_{UC} \quad (7)$$

Some notable $\eta_{UC}$ values achieved include those in liquid-state UC systems such as 28% in the first aerated solvent-free system using a Pt(II) porphyrin-based sensitizer and,[82] 35.17% in the system using a Pd(II) tetraphenylporphyrin-based sensitizer with DPA,[83] and 22% in the solid-state by combining a Pd(II) octaethylporphyrin sensitizer with DPA,[84] each using heavy-metal-based sensitizer molecules and 9,10-diphenylanthrancene DPA as the acceptor.

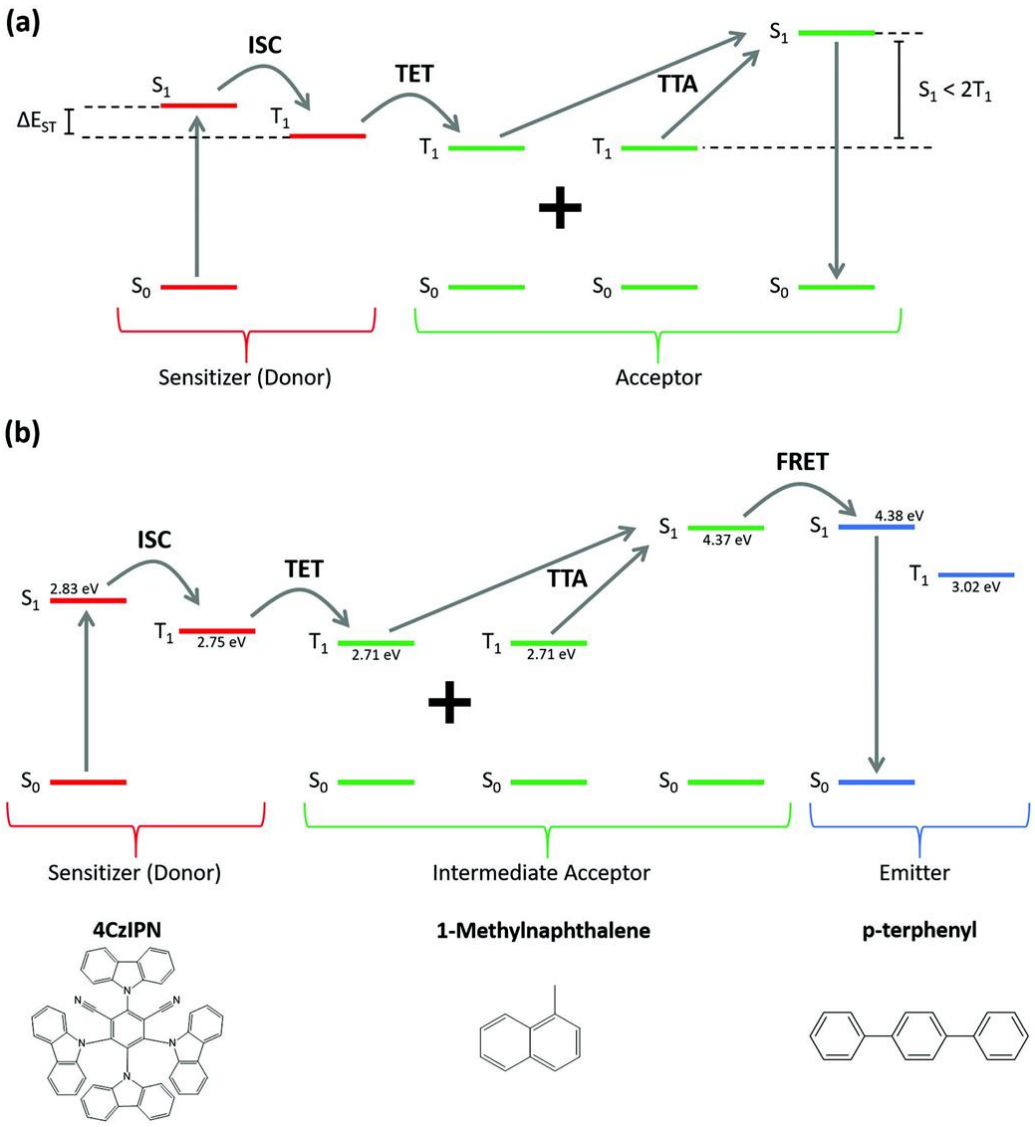


**Figure 3.1. a) General schematic for TTA-UC where upconversion is achieved in a two component system. b) Schematic for how TTA-UC can be achieved in a three component system, as is done in this work. Energy levels are taken from DFT gas phase calculations and experimental quenching data. Arrows indicate the flow of energy.**

The benefit of using heavy-metal-based materials for triplet photon upconversion is that those large atoms increase the efficiency of the ISC step ($\Phi_{ISC}$) by increasing the amount of spin-orbit coupling. This coupling is beneficial because of the nature of the ISC transition, which converts the singlet excited state to a triplet excited state, requiring one electron to undergo a spin flip which is classically forbidden. A transition involving a spin-flip would alter the spin angular momentum of the electron, causing its total angular momentum to no longer be conserved, and thus the transition itself to be forbidden. However, when the spin angular momentum and orbital angular momentum are coupled, an additional interaction is possible which compensates for change caused by the spin-flip, thus conserving the total angular momentum.[85] Although heavy metal atoms thoroughly promote ISC through this method, there are some drawbacks to their use in some cases such as their toxicity or higher price tag.[76,86] In addition, molecules in this class of materials tend to have a large singlet–triplet splitting energy, which limits their maximum possible anti-Stokes shift in TTA-UC systems

To develop heavy-metal free TTA-UC systems, researchers have turned to a class of materials which undergo reverse-intersystem crossing (RISC) upon thermal excitation of triplets to re-populate the singlet state. As this requires the forbidden spin-flip, the singlet emission from RISC is delayed and these materials are known as thermally activated delayed fluorescence (TADF) emitters.[58,87,88] The first applications of TADF materials were in organic light-emitting diodes (OLEDs), resulting in several high-performance devices.[89–94] The fast and efficient ISC in TADF materials is aided by material design strategies which produce a small energetic offset (less than 100 meV) between their $S_1$ and $T_1$ energy levels ($\Delta E_{ST}$), which also makes these materials attractive for triplet-upconversion.[27–29] One of the common TADF materials is 2,4,5,6-

tetrakis(carbazol-9-yl)isophthalonitrile (4CzIPN), which has also been used in high-performance UV photodetectors and OLEDs.[91,95–99] By pairing the 4CzIPN sensitizer with p-terphenyl as the triplet acceptor/singlet emitter, Yanai et al. achieved a maximum normalized solution-state $\eta_{UC}$ of 2.8%.[100] Apart from the efficiency, the magnitude of upconversion reported through the Anti-Stokes shift is also an important parameter. The excitation wavelength-independent definition of the Anti-Stokes shift is the difference between the lowest energy absorbance peak of the sensitizer molecule and the fluorescence peak of the emitter.[81] The high $S_1$ energy of p-terphenyl yielded a notably large Anti-Stokes shift of 0.83 eV, with the current record for systems using TADF sensitizers being 0.93 eV by Chen et al. using a fluorescein-based sensitizer.[28,100] In seeking to improve upon the efficiency of the 4CzIPN:p-terphenyl system, we turned to the work of Ogawa et al., in which they doubled the $\eta_{UC}$ value by the addition of an "energy collector" (intermediate acceptor) molecule, which accepts triplets from the Pt(II) porphyrin-based sensitizer and donates singlets to a separate anthracene-based emitter molecule.[101] This approach has not been used in the metal-free TTA-UC materials. In this work, we present a ternary metal-free TTA-UC system utilizing the TADF sensitizer 4CzIPN with the triplet acceptor 1-methylnaphthalene (1MeN) and energy collector/singlet emitter p-terphenyl (p-terp) with a $\eta_{UC}$ of 7.6% determined using absolute quantum yield measurements. The choice of intermediate acceptor was made after an acceptor candidate screening process relying on DFT simulations and time-dependent photoluminescence. Herein, we also present a brief comparison of TET performance between 4CzIPN and 4CzIPN-Br which utilizes the heavy-atom effect to promote ISC.

### *B. Results and Discussion*

1. Intermediate Acceptor Screening

The absolute quantum yield of the TTA-UC process can be described by

$$\eta_{UC} = 2 \times \Phi_{UC} = \Phi_{ISC}\Phi_{TET}\Phi_{TTA}f\Phi_{AF} \quad (8)$$

where $\Phi_{ISC}$ is the quantum yield of intersystem crossing, $\Phi_{TET}$ is the quantum yield of triplet electron transfer, $\Phi_{TTA}$ is the quantum yield of triplet–triple annihilation, f is the spin statistical factor (the fraction of annihilation events resulting in a singlet excited state), and ΦAF is the quantum yield of fluorescence of the acceptor molecule. For a ternary blend, the final term in Equation (8), $\Phi_{AF}$, simply becomes the product of the quantum yield of the energy transfer from the intermediate acceptor and the quantum yield of fluorescence for the emitter. This equation is instructive because it shows how the overall upconversion efficiency can be improved by tweaking individual terms in the equation. Our work began by focusing on $\Phi_{TET}$.

An initial determination of how efficiently p-terphenyl quenched the triplet excitons of 4CzIPN was made by measuring the delayed fluorescence of the TADF material with and without the acceptor **(Figure 3.2)**. A high efficiency of TET ($\Phi_{TET}$) would result in fewer triplets able to undergo RISC to the singlet state from which this delayed fluorescence is observed. The addition of $25 \times 10^{-3}$ M p-terphenyl to $50 \times 10^{-6}$ M 4CzIPN in benzene has only a very small impact on the delayed fluorescence of 4CzIPN, implying the $\Phi_{TET}$ is low. Therefore, the first task in improving the upconversion yield from 4CzIPN was to explore different acceptors that might have more suitable energy levels, which could lead to a great increase in $\Phi_{TET}$.

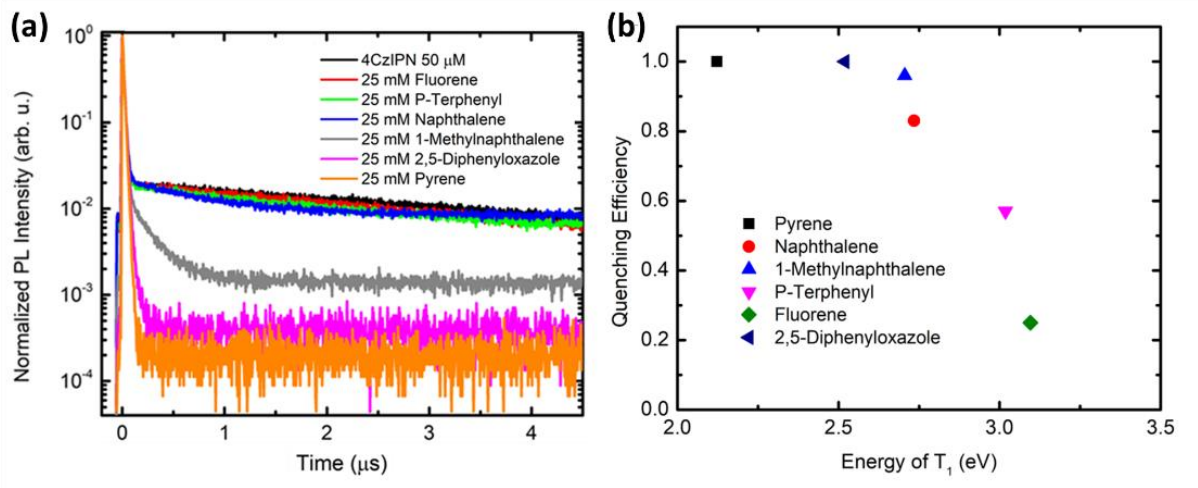


**Figure 3.2 (a) Decay of delayed photoluminescence from 50 μm 4CzIPN in benzene with 25 mm of selected acceptors. (b) Quenching efficiency of various acceptors plotted versus their $T_1$ energy level.**

To assess the viability of different acceptor molecules, DFT calculations of the excited singlet $S_1$ and triplet $T_1$ energy levels were pursued for various small molecules. Calculations were performed in the gas phase using the B3LYP functional and 6-31G (d, p) basis set.[102,103] The results are shown in Table 3.1. Once the $T_1$ and $S_1$ energy levels had been determined, the ratio between them provided a sense of whether TTA could even result in upconversion with the knowledge that no upconversion would occur for molecules where the $S_1$ energy level was higher than twice that of the $T_1$ energy level. Ideally, for a maximized anti-Stokes shift, the $S_1$ energy should be just below twice the energy of $T_1$. The most promising acceptor candidates were identified by first eliminating molecules with an $S_1/T_1$ ratio above 2.0. The remaining molecules were down-selected again by considering a maximum $T_1$ energy of 3.0 eV (approximately the value for p-terphenyl). Finally, molecules known to have a very low fluorescence quantum yield were omitted.[104] From this analysis, it became clear that naphthalene and 1-methylnaphthalene would be great choices, with 2,5-diphenyloxazole (PPO),

fumaronitrile, fluorene, carbazole, and 3-phenyl dibenzofuran as other potentially good acceptors.

$$Q_{\text{efficiency}} = 1 - \frac{k_{\text{d pristine}}(s^{-1})}{k_{\text{d blend}}(s^{-1})} \quad (9)$$

The efficiency of the selected acceptors in quenching the 4CzIPN delayed fluorescence was determined by observing the rate of delayed fluorescence ($k_d$) with and without the acceptor based on Eq. 9 (Figure 3.2). Pyrene was included not as a real acceptor candidate, but to assess what 100% quenching should look like, since its $T_1$ energy is very small. From this data, we can infer that the triplet energy of 4CzIPN is about 2.5 eV. Furthermore, this data allowed us to rule out fluorene as a potentially good acceptor.

**Table 1. Singlet and triplet energy levels calculated using density functional theory.**

| Molecule | $T_1$ [eV] | $S_1$ [eV] | $S_1/T_1$ | Molecule | $T_1$ [eV] | $S_1$ [eV] | $S_1/T_1$ |
|---|---|---|---|---|---|---|---|
| naphthalene | 2.73 | 4.46 | 1.63 | 1,3,5-hexatriene [cis] | 2.13 | 4.85 | 2.28 |
| 1-methylnaphthalene | 2.71 | 4.37 | 1.62 | 1,3,5-hexatriene [trans] | 2.09 | 4.86 | 2.33 |
| carbazole | 3.19 | 4.15 | 1.30 | pyrrole | 4.15 | 6.55 | 1.58 |
| fluorene | 3.10 | 4.67 | 1.51 | pyrazole | 4.41 | 6.79 | 1.54 |
| p-terphenyl | 3.02 | 4.38 | 1.45 | oxazole | 4.04 | 6.40 | 1.58 |
| pyrene | 2.12 | 3.72 | 1.75 | thiazole | 3.56 | 5.36 | 1.50 |
| 2-methylnaphthalene | 2.76 | 4.41 | 1.60 | imidazole | 4.33 | 6.58 | 1.52 |
| p-methyl anisole | 3.72 | 5.30 | 1.43 | furan | 3.84 | 6.50 | 1.69 |
| 1,4-dimethoxybenzene | 3.74 | 5.28 | 1.41 | thiophene | 3.48 | 5.92 | 1.70 |
| 9,10-dihydrophenanthrene | 3.06 | 4.57 | 1.50 | thienothiophene | 2.96 | 4.88 | 1.65 |
| dibenzofuran | 3.20 | 4.53 | 1.41 | cyclopehtadithiophene | 2.31 | 4.01 | 1.74 |
| 3-phenyl dibenzofuran | 2.95 | 4.23 | 1.43 | benzodithiophene | 2.64 | 3.99 | 1.51 |
| indole | 3.25 | 4.88 | 1.50 | 1,4-cyclohexadiene | N/A | 5.98 | N/A |
| 2,5-diphenylfuran | 2.35 | 3.76 | 1.60 | PPO-2 | 2.99 | 4.71 | 1.58 |
| 2,5-diphenyloxazole | 2.52 | 3.88 | 1.54 | PPO-3 | 2.90 | 4.72 | 1.63 |
| benzofuran | 3.31 | 5.07 | 1.53 | anthracene | 1.80 | 3.28 | 1.82 |
| benzothiadiazole | 2.23 | 3.86 | 1.73 | 9,10-dihydroanthracene | 3.71 | 5.29 | 1.43 |
| isoindene | 1.10 | 3.02 | 2.75 | 9,10-diphenylanthracene | 1.74 | 3.17 | 1.82 |
| pentalene | 0.55 | 1.63 | 2.95 | tyrosine | 3.69 | 5.05 | 1.37 |
| fumaronitrile | 2.70 | 5.36 | 1.99 | acrylonitrile | 3.33 | 6.10 | 1.83 |
| 1,3-cyclohexadiene | 2.49 | 4.82 | 1.93 | tetracyanoethylene | 1.94 | 4.33 | 2.23 |

Given that the calculated triplet energies of naphthalene and 1-methylnaphthalene are so similar, their difference in photoluminescence quenching is surprising. We suspected that the energy of $T_1$ was not the only important factor for $\Phi_{TET}$. Because triplet electron transfer is governed by the Dexter energy transfer mechanism, the donor and acceptor molecules must have suitable wavefunction overlap of their frontier molecular orbitals. Perhaps then, naphthalene and 1-methylnaphthalene differ significantly in this respect. The lower degree of symmetry for 1-methylnaphthalene compared to naphthalene could also be significant.

Although triplets are more efficiently transferred to the 1-methylnaphthalene than p-terphenyl, steady-state photoluminescence measurements revealed that p-terphenyl still resulted in a higher intensity of upconverted emission (Figure 3.2b). This can be linked to the relative photoluminescence quantum yields of the individual emitter molecules, as there is more radiative decay from the singlet state of p-terphenyl than 1-methylnaphthalene.[104] To take advantage of the efficient TET to 1-methylnaphthalene while utilizing a more emissive singlet acceptor, we prepared a ternary TTA-UC system.

2. TTA-UC Comparison between Binary and Ternary Solutions

In choosing the singlet acceptor, one must consider the efficiency with which the singlets formed through TTA in the triplet acceptor/singlet donor will be transferred to the emitting molecule. Since this will occur through Förster resonance energy transfer (FRET), the emission spectrum of the singlet donor should have good overlap with the absorbance spectrum of the singlet acceptor.[18] For our ternary system, we have chosen p-terphenyl to serve as the singlet emitter (Figure 3.1b). It is important to note that 1-methylnaphthalene and p-terphenyl do not

display ideal spectral overlap for FRET (Figure 7.1 in the Appendix). However, the comparison of this ternary TTA-UC system to the binary 4CzIPN:p-terphenyl system allows us to demonstrate the impact of these combined strategies, optimizing the $\Phi_{TET}$ and employing a high quantum yield emitter, on the upconversion quantum yield and highlight the opportunity for further $\eta_{UC}$ enhancement by optimizing the FRET efficiency.

Our work with this ternary TTA-UC solution began with optimizing the concentration of p-terphenyl for the maximal UC emission based on steady-state photoluminescence measurements utilizing 457 nm excitation from an Ar-ion laser (Figure 3.3a). The relative amount of upconversion increased up to a maximum at $26 \times 10^{-3}$ M p-terphenyl, while further increasing the concentration of p-terphenyl actually reduced the upconversion intensity. Steady-state upconversion spectra of binary and ternary blends are shown in Figure 3.3b. Note how the upconversion spectrum of the ternary blend is identical to the binary blend of 4CzIPN:p-terphenyl. The absence of spectral features in the ternary blend related to 1-methylnaphthalene emission indicates efficient energy transfer from 1-methyl-naphthalene to p-terphenyl (this is especially apparent at short wavelengths, e.g., 325 nm). The large increase in upconversion intensity in the ternary blend compared to the binary blend with p-terphenyl further indicates that energy transfer from 4CzIPN to p-terphenyl was mediated through 1-methylnaphthalene. Time resolved measurements of the UV emission in the ternary blend also suggest that this emission results from the TTA-UC process (Figure 7.2). It is worth noting that although the 4CzIPN:1-methylnaphthalene blend has a lower upconversion intensity compared to the 4CzIPN:p-terphenyl blend, its anti-Stokes shift is 0.08 eV larger than the anti-Stokes shift of 4CzIPN:p-terphenyl. Relative to the excitation wavelength of 457 nm, the anti-Stokes shift of 4CzIPN:1-

methylnaphthalene is 0.99 eV—the largest anti-Stokes shift we are aware of in purely organic TTA-UC systems.

The maximum upconversion quantum yield of the 4CzIPN ($50 \times 10^{-6}$ M), 1-methylnaphthalene ($25 \times 10^{-3}$ M), p-terphenyl ($26 \times 10^{-6}$ M) solution was then determined using the integrating sphere setup described in the experimental section. The ternary solution displayed a maximum $\eta_{UC}$ of 7.6%, more than twice that of the binary solution of 4CzIPN ($50 \times 10^{-6}$ M) and p-terphenyl ($25 \times 10^{-3}$ M) using the same singlet emitter (3.4%) (Figure 3. 4a–c). Again, the 1-methylnaphthalene served to increase the efficiency of triplet transfer from the sensitizer. This greater $\Phi_{TET}$ allows more triplets to partake in triplet– triplet annihilation, yielding singlets which are then transferred to the more emissive p-terphenyl. The binary solution of 4CzIPN ($50 \times 10^{-6}$ M) and 1-methylnaphthalene ($25 \times 10^{-3}$ M) was determined to have a maximum $\eta_{UC}$ of 2.5%, showing how the improved $\Phi_{TET}$ alone does not result in a greater photoluminescence upconversion efficiency. Further discussion on the relative upconversion efficiency of these blends is provided in Figure 7.3.

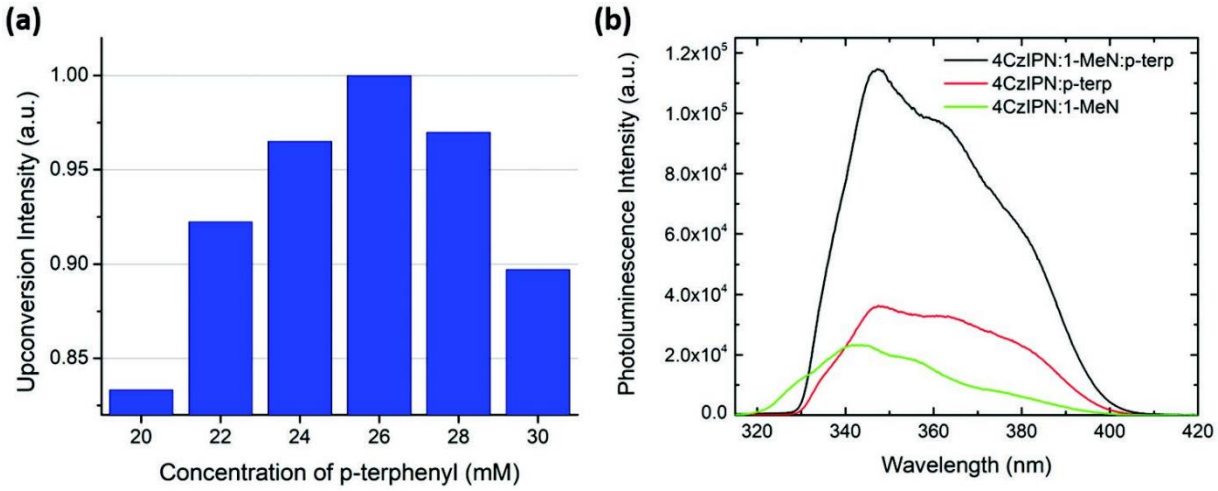


**Figure 3. (a) Optimization of p-terphenyl concentration in the ternary blend. The concentrations of 4CzIPN and 1-MeN were kept constant at $50 \times 10^{-6}$ M and $25 \times 10^{-3}$ M,**

**respectively. Upconversion intensities were normalized to the peak intensity of the optimal solution which contained $26 \times 10^{-3}$ M p-terphenyl. b) Steady-state photoluminescence from upconversion solutions in benzene with $50 \times 10^{-6}$ M 4CzIPN, $25 \times 10^{-3}$ M p-terphenyl or 1-MeN in the binary solutions and $50 \times 10^{-6}$ M 4CzIPN, $25 \times 10^{-3}$ M MeN and $26 \times 10^{-3}$ M p-terphenyl in the ternary solution. Spectra were recorded with a Thor Labs UG-11 filter in front of the spectrometer.**

The threshold excitation intensity ($I_{th}$) was also determined for each of these upconversion solutions (Figure 3.4d-f). This value represents the incident light intensity above which the triplet population in the sample is high enough that triplet annihilation is the main process removing triplets from the excited state. As the TTA process results in singlet production, among other products, the $I_{th}$ value can be determined by observing the dependence of the upconverted photoluminescence intensity on the excitation intensity. In the regime of low excitation power, the photoluminescence intensity depends quadratically on the excitation intensity as both spontaneous triplet decay and TTA remove triplets from the excited state. When the photoluminescence intensity resulting from excitation below $I_{th}$ is plotted against the excitation intensity, and both are logarithmically scaled, the result will be a line with a slope approximating 2. In the high excitation regime with efficient TTA predominately determining the rate of triplet removal from the excited state, there is a linear relationship between the excitation intensity and the intensity of upconverted photoluminescence. Thus, the log-log plot of photoluminescence intensity vs. excitation intensity will show a line with a slope approximating 1 in the high excitation regime beyond $I_{th}$.[105] This quadratic-to-linear transition has been used to certify whether the upconversion mechanism is triplet annihilation along with conveniently indicating the $I_{th}$ value at the intersection of the two lines.[100,105]

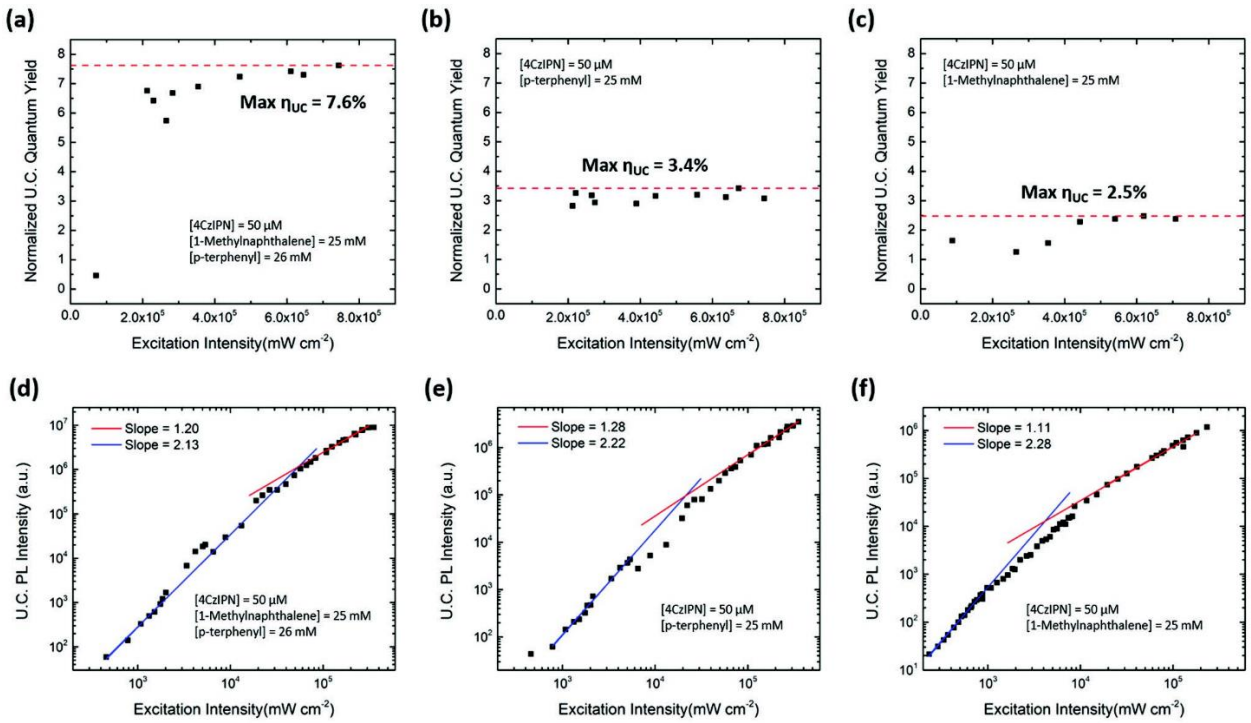


**Figure 3.4. a–c) Plots of the integrated sphere photoluminescence quantum yield values for the ternary, binary with p-terphenyl and binary with 1-methylnaphthalene upconversion solutions, respectively. d–f) Plots of the photoluminescence upconversion intensity versus the excitation intensity for the indicated TTA-UC solutions in benzene. The red and blue lines are extended linear fits which serve as a guide to the eye. The fitted regions are shown in Figure 7.4 of the Appendix.**

Each of our upconversion solutions shows the quadratic-to-linear transition indicative of TTA-UC. The $I_{th}$ values determined were as follows, 45,671 mW cm$^{-2}$ for the ternary solution, 20,877 mW cm$^{-2}$ for 4CzIPN with p-terphenyl, and 4,072 mW cm$^{-2}$ for 4CzIPN with 1-methylnaphthalene. It is important to note that the $I_{th}$ determined for our binary solution of 4CzIPN with p-terphenyl is significantly higher than that shown previously. Yanai et al. used a tunable dye laser to excite at 445 nm, while our samples were excited with the 457 nm output of the $Ar^+$-ion laser where the 4CzIPN sensitizer does not absorb as strongly (Figure 7.3). Regardless, these differences in $I_{th}$ do illustrate the importance of $\Phi_{TET}$ as the more efficient triplet acceptor 1-methynaphthalene results in a five-fold decrease in the $I_{th}$. When comparing

between the 4CzIPN:1-methylnaphthalene and the ternary UC solutions, we see an order of magnitude increase in the $I_{th}$ value when the energy collector p-terphenyl is added. In contrast, when comparing the binary and ternary crystalline TTA-UC systems prepared Ogawa et al., they noted that the similar $I_{th}$ values and triplet lifetimes indicated that the triplet annihilation likely occurred in the same component, the intermediate acceptor, present in both the binary and ternary UC systems.[101] Perhaps, there is some triplet excitation transferred directly to the p-terphenyl molecule in the ternary solution, contributing to the increased $I_{th}$ in comparison with the binary solution. Some strategies proposed to decrease $I_{th}$ include altering the sensitizer concentration to reduce the amount of reverse TET back to the sensitizer, covalent attachment of the sensitizer and acceptor molecules to a backbone structure, and utilization of molecular self-assembly.[80,106,107] Managing the $I_{th}$ will be important in order to take advantage of the ternary TTA-UC system design for efficiently supplying triplet excitons to bright (high QY) emitters without sacrificing the low $I_{th}$ values which make TTA attractive.

3. TET Comparison with 4CzIPN-Br

In the upconversion experiments using 4CzIPN as a triplet sensitizer, there was always a considerable amount of residual fluorescence from 4CzIPN. The $\Phi_{ISC}$ of 4CzIPN in benzene was determined to be 0.91 and for 4CzIPN-Br 0.98.[99] One would assume that the overall upconversion efficiency of blends could be improved by using 4CzIPN-Br instead of 4CzIPN. However, the quenching efficiency of 1-methylnaphthalene, naphthalene, and p-terphenyl were unexpectedly low for 4CzIPN-Br, despite the fact its singlet and triplet energies are nearly identical to 4CzIPN (Figure 4.5). This brief comparison further highlights the need for in-depth investigations to understand what underpins the $\Phi_{TET}$ achievable in these systems.

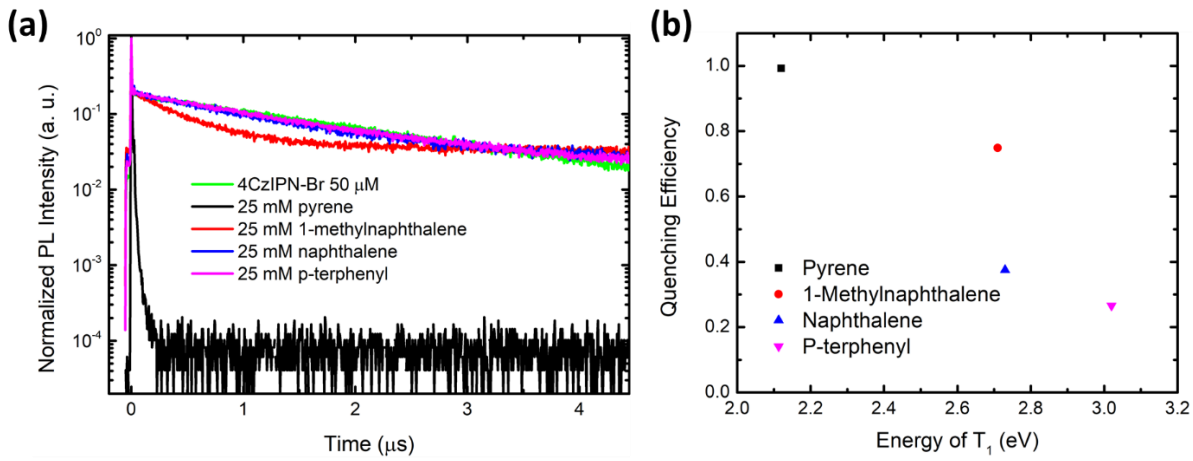


**Figure 4.5. (a) Decay of delayed photoluminescence from $50 \times 10^{-6}$ M 4CzIPN-Br in benzene with $25 \times 10^{-3}$ M of selected acceptors. (b) Quenching efficiency of various acceptors plotted versus their $T_1$ energy level.**

## IV. Solid-State Magnetic Resonance Study of Doped Polymer Morphology

This chapter presents research reproduced from Ref. **12** with permission from the Royal Society of Chemistry. Herein, we compare the local morphology and molecular-level interactions between a semiconducting polymer and two small molecule dopants, BCF and F4TCNQ, through techniques of magnetic resonance spectroscopy. The resulting observations help to explain the dramatic differences in the performance of each dopant. I would like to thank Dr. Manjunatha Reddy and Dr. Hervé Vezin for performing, analyzing, and discussing the solid-state NMR and EPR measurements, respectively.

Molecular doping strategies facilitate orders of magnitudes enhancement in the charge carrier mobility of organic semiconductors (OSCs). Understanding the different doping mechanisms and molecular-level constraints on doping efficiency related to the materials energy levels is crucial to develop versatile dopants for OSCs. Given the compositional and structural heterogeneities associated with OSC thin films, insight into dopant-polymer interactions by long-range techniques such as X-ray scattering and electron microscopy is exceedingly challenging to obtain. This study employs short-range probes, solid-state (ss)NMR and EPR spectroscopy, to resolve local structures and intermolecular interactions between dopants such as F4TCNQ (2,3,5,6-tetrafluoro-7,7,8,8-tetracyanoquinodimethane), Lewis acid BCF (tris[pentafluorophenyl] borane) and Lewis base conjugated polymer, PCPDTBT (P4) (poly[2,6-(4,4-bis(2-hexadecyl)-4H-cyclopenta[2,1-b;3,4-b′]dithiophene)-alt-4,7(2,1,3-benzothiadiazole). Analysis of $^{1}H$ and $^{13}C$ ssNMR spectra of P4, P4:F4TCNQ and P4:BCF blends indicate that the addition of dopants induces local structural changes in P4 polymer, and causes paramagnetic-induced signal broadening and intensity losses. The hyperfine interactions in P4:BCF and P4:F4TCNQ are

characterized by two-dimensional pulsed EPR spectroscopy. For P4:F4TCNQ, $^{19}$F ssNMR analysis indicates that the F4TCNQ molecules are distributed and aggregated into different local chemical environments. By comparison, BCF molecules are intermixed with P4 polymer and interact with traces of water molecules to form BCF-water complexes which serve as Brønsted acid sites, as revealed by $^{11}$B ssNMR spectroscopy. These results indicate the P4-dopant blends exhibit complex morphology with different distributions of dopants, whereby the combined use of ssNMR and EPR provides essential insights into how higher doping efficiency is observed with BCF and a mediocre efficiency associated with F4TCNQ molecules.

### *A. Introduction*

Organic semiconductors (OSC) are attractive due to their flexibility and lightweight, which lend themselves suitable for optoelectronic applications such as organic light emitting diodes (OLEDs) for large area displays, organic photovoltaic cells (OPVs), organic photodiodes, organic field-effect transistors (OFETs), thermoelectrics, and emerging applications in bioelectronics. A key parameter for such applications is the energy gap between electronic states of of π-conjugated building blocks, and charge transport within and in between π-conjugated chains. For OSCs, the conductivity is limited by the relatively low number of charge carriers compared to their inorganic counterparts and hybrid compositions.[108,109] This limitation is due in part to the relatively large energy band gaps of OSCs, meaning a sufficiently high energy (above the thermal energy provided at room temperature) must be supplied to excite an electron from the ground state into the excited state. Additionally, poor electric field screening in organic semiconductors leads to the attractive Coulombic force between the excited electron and its positively charged "hole" in the lower energy level to provide an additional energy barrier to

overcome.[58] One way to enhance the number of charge carriers is through doping, the addition of a dopant to the OSC which either serve as electron donors (n-type doping) or electron acceptors (p-type doping).

Early OSC doping strategies relied on the use of metals and volatile halides[110,111] which unfortunately tended to diffuse through the organic layers, resulting in irreproducible doping and device instability.[112,113] The advent of molecular dopants has allowed for stable doping to be achieved in OSCs, improving the performance of devices such as OFETs, OLEDs, and OPVs.[8–13, 36] Specifically, acid-base complexation and reduction-oxidation (redox) reactions between small molecule dopants and conjugated polymers are among the widely explored chemical doping strategies to adjust the optical and electronic properties in OSCs. In a redox doping, an integer charge transfer occurs from the LUMO (Lowest Unoccupied Molecular Orbital) of dopant to the HOMO (Highest Occupied Molecular Orbital) of OSC, which depends strongly on their energy level alignment.[120] F4TCNQ is one of the most common p-dopant because its LUMO matches with the HOMO of many OSCs and the material is commercially available. However, F4TCNQ has very low solubility in common organic solvents and tends to aggregate in thin films.[9,10,121–123] In the case of acid-base reactions, doping occurs by proton transfer to the basic polymer backbones upon addition of small molecule acids. Several Lewis and Brønsted acids have been proposed as molecular dopants to OSCs, whereby Lewis and Brønsted acids lead to weak and strong doping, respectively.[124–131] Recently, OSC doping driven by ion exchange has been suggested.[132] In order to take full advantage of the opportunity presented by molecular doping, a detailed understanding of the polymer-dopant intermolecular interactions upon doping with specific small molecules is needed.

The impact of dopants on the optoelectronic properties of OSCs has been rationalized based on morphological studies and dopant-host interactions. For example, in the poly(3-hexylthiophene) (P3HT):F4TCNQ system, it was observed that doping by vapor diffusion resulted in minimal disturbance to the ordering of the conjugated backbone along which charges are transported in OSC materials, yielding significantly higher conductivity values when compared to solution doping which more drastically altered the OSC morphology.[133,134] In the case of poly[2,5-bis(3-tetradecylthiophen-2-yl)thieno[3,2-b]thiophene](PBTTT-$C_{14}$):F4TCNQ blend, F4TCNQ molecules are ordered in a cofacial arrangement with PBTTT-$C_{14}$, leading to an efficient charge transfer.[135,136] In other studies, varied processing conditions were used to tune the ratio of doping by F4TCNQ which occurred through the integer charge transfer (ICT) or partial charge transfer mechanisms as explained by the location of the dopant molecule in the polymer structure.[137–140] As partial charge transfer involves orbital hybridization between the dopant and the host material,[141,142] it was shown to be favored when the dopant intercalates between the conjugated backbone of the OSC.[135,143] In contrast to the multitude of doping studies involving F4TCNQ molecules, the doping mechanism employed by the relatively nascent Lewis acid dopant BCF is still unclear and ripe for further investigation.[144–146] Nevertheless, the emerging Lewis acid dopants such as BCF are of great current interest to the OSC community due their high doping efficiency, defined as the ratio of free charge carriers to dopant molecules, and good solubility in common organic solvents when compared to other dopants such as F4TCNQ.[129,144,147–149] When BCF molecules interact with traces of water molecules, BCF-water complexes are formed which act as strong Brønsted acids shown to dope conjugated polymers.[144] In a recent study by Yurash et. al., the proposed BCF doping mechanism is based on proton transfer from a BCF·$H_2O$ adduct to the polymer backbone, followed by electron transfer from a

nearby neutral polymer chain. It is then proposed to result in a neutral radical on the polymer backbone chain containing the extra proton, a positive radical on the adjacent polymer backbone chain which already donated an electron, and a coexisting BCF-$OH^-$ anion.[144] In a later study by Arvind et al, it is the neutral protonated radical which was not observed in electron paramagnetic resonance (EPR) measurements of P3HT:BCF blend.[145] Therefore, it has been suggested that the overall P3HT-BCF reaction resulted in the formation of $H_2$ product, with one possible route for $H_2$ formation being the reaction of two neutral radical species in the neighboring polymer chains. In addition, density-functional theory (DFT) calculations of various scenarios from both mechanisms show highly endergonic processes (positive free energy) unless a larger anion, $[BCF(OH)(OH_2)BCF]^-$, is formed in which $[BCF(OH)]^-$ is hydrogen bonded to another $BCF(OH_2)$ complex.[146] The formation of $[BCF(OH)(OH_2)BCF]^-$ has been previously observed by Doerrer and Green in their work on the oxidation of metallocenes by $BCF(OH_2)$ in non-aqueous solvents, in which $H_2$ was also proposed to be the side product.[150] The formation of $H_2$ proposed in these BCF oxidation reactions of both P3HT and metallocenes has not, however, been observed experimentally. Thus, molecular-level understanding of the doping mechanism is expected to help the development of design rules for producing novel efficient Lewis acids which dope OSCs. However, such knowledge is rarely fully established, due to compositional and structural heterogeneity associated with molecularly doped conjugated polymers.

Studies on dopant-host morphology have mostly been based on techniques such as X-ray scattering which is limited to detecting the crystalline and well-ordered regions of a material, and atomic force or optical microscopy which are limited by their nature as surface techniques. Very few OSC doping studies have utilized complementary analytical techniques such as solid-state NMR (ssNMR) spectroscopy.[136,151] Information on intermolecular interactions at the atomic-

scale can be obtained through ssNMR and EPR techniques, which cover the entirety of the material by probing both crystalline as well as amorphous regions in both conjugated polymers and their blends.[70,71,152–156] Specifically, 2D EPR techniques enable the electron-nuclear hyperfine interactions in polymer-dopant blends to be identified and distinguished at complementary length scales to ssNMR, as the latter technique probes predominantly the undoped regions of polymer.

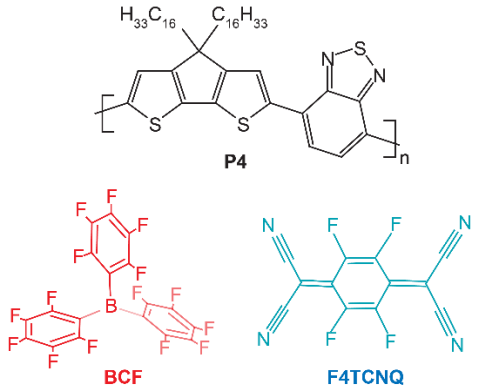


**Figure 4.1. Structures of the host polymer P4 along with dopants BCF and F4TCNQ.**

In this study, 1D and 2D ssNMR and EPR techniques were employed to study the intermolecular interactions between the dopants BCF-water complex and F4TCNQ with the OSC polymer referred to as P4 (Figure 4.1). In P4:F4TCNQ, fully doped F4TCNQ molecules lead to strong hyperfine interactions with P4 backbones as revealed by 2D EPR analysis (e.g., charge transfer complexes that may disrupt π-π stacking), and the undoped/aggregated F4TCNQ molecules (i.e., diamagnetic regions) can be detected by $^{19}$F ssNMR spectroscopy. In the P4:BCF blend, the local boron environments of BCF dopants are characterized by $^{11}$B NMR and the hyperfine structure is characterized by 2D EPR techniques. Furthermore, the results discussed herein elucidate that the BCF doping mechanism does not rely on BCF association (or intercalation) with the conjugated backbone, as it does not require the formation of a charge-

transfer complex. The results provide essential insights into polymer-dopant interactions, and partly explain the lower doping efficiency observed in F4TCNQ doped P4 (< 4%) as compared to that of BCF doped P4 (> 14%).[157] The addition of these solid-state NMR and EPR results are expected to help experimental characterization and modelling studies of different BCF-polymers interactions and doping mechanisms.

### *B. Results and Discussion*

We separately examined the local structures and interactions in neat P4 polymer and P4:dopant blends at different molar ratios. Based on our previous morphological studies of BCF-doped P4 using grazing incidence wide angle X-ray scattering (GIWAXS) and atomic force microscopy (AFM), we did not expect BCF to significantly alter the degree of molecular order in P4 polymer.[40] Nevertheless, the addition of a dopant to a polymer is expected to result in a variety of local chemical environments such as diamagnetic and paramagnetic species, which can be investigated by ssNMR and EPR techniques.

#### 1. Nuclear Magnetic Resonance

A molecular-level assessment of local structures and interactions in the neat P4, P4:BCF and P4:F4TCNQ samples can be made by analyzing the $^{1}H$ and $^{13}C$ Magic-Angle Spinning (MAS) NMR spectra. The compositional and structural heterogeneity of P4-dopant blends is indicated by broad signals covering a wider range of $^{1}H$ and $^{13}C$ chemical shift ($\delta$) values than the pristine P4 polymer (Appendix, Figures 7.10 and 7.11).[158] Of particular note, the origin of NMR signal broadening in doped P4 polymers can be related to several short and long range interactions, anisotropic bulk magnetic susceptibility (ABMS) effects, hyperfine interactions, locally (dis)ordered structures and relaxation-induced broadening that are often difficult to deconvolute.

However, $^{1}H \rightarrow ^{13}C$ cross polarization (CP) MAS NMR[159] spectra of P4-dpoant blends exhibit higher signal broadening and intensity losses in their aromatic regions than the alkyl peaks, indicating that the noteworthy changes occur in the vicinity of P4 backbone moieties (Appendix, Figure 7.10). Notably, broad distributions of $^{13}C$ peaks in the range 105-175 ppm (~70 ppm wide for P4:BCF and P4-F4TCNQ blends compared to ~50 ppm for pristine P4) indicate the different local chemical environments in doped polymers as well as the presence of free radicals, which could also lead to signal intensity loss due to paramagnetic induced relaxation.[160,161] Consequently, a large number of transients were coadded to acquire $^{13}C$ CP-MAS spectra of P4:dopants with good signal-to-noise ratio (20480 and 16384 coadded transients for P4:F4TCNQ and P4:BCF), compared to the coaddition of 4098 transients for the P4 polymer. Although $^{1}H \rightarrow ^{13}C$ CP-MAS experiments of these materials do not provide quantitative assessment of $^{13}C\{^{1}H\}$ peak enhancements, a comparison of alkyl/aromatic $^{13}C$ signal intensities indicate that the major intensity loses occur in P4-dopant blends (Figure 7.10, Appendix) compared to the neat P4 polymer.

To gain further insight into the signal intensity losses induced by the addition of a dopant to P4 polymers, $^{1}H$ MAS NMR spectra of undoped and doped P4 polymers (~2.5 mg each) were acquired at identical experimental conditions and compared (Appendix, Figure 7.11 and Table 7.1). For pristine P4 polymer, the aliphatic signal (0-4 ppm) intensity is calibrated to 66 which leads to the estimation of aromatic signal (5-9 ppm) intensity of 4.7, consistent with the composition of the CPDT-BT unit with 4 aromatic protons and 66 alkyl sidechain protons. By comparison, the peak integral of alkyl sidechains in P4:F4TCNQ (1:0.2 molar ratio) blend is reduced to 36.3 (calibrated with respect to 66 in pristine P4), and the aromatic signal is reduced to 1.7, which suggests that the intensity losses occurred for both alkyl and aromatic peaks,

though the greater intensity losses were observed for aromatic peaks than the aliphatic signals. Similar trend is observed for the P4:BCF blend, whereby the peak integrals of alkyl (49.5) and aromatic (1.4) groups are decreased (Table 7.1). It can be reasoned that the presence of both para- and diamagnetic entities in the vicinity of P4 polymer backbones, as characterized by the EPR and NMR techniques discussed below, contribute to such peak broadening and intensity losses. For example, previous studies have shown that the F4TCNQ molecules are known to intercalate between the π- π stacks and/or lamellar stacks of PBTTT-C[14] and P3HT polymers, leading to charge transfer complexes,[133,136,139,140,162–165] In addition, the contributions from the undoped polymer regions with self-aggregated dopant molecules to the NMR peak broadening cannot be ruled out.

To examine the backbone and sidechain moieties in (un)doped P4 polymer more closely, we employed 2D $^{1}$H-$^{13}$C heteronuclear correlation and $^{1}$H-$^{1}$H Double Quantum-Single Quantum (DQ-SQ) correlation NMR spectroscopy (Appendix, Figures 7.12 and 7.13). In measurements of this type, the 2D signals are created for through-space and dipolar coupled $^{1}$H-$^{13}$C and $^{1}$H-$^{1}$H spin pairs, which correspond to inter- and intramolecular interactions. Specifically, 2D $^{1}$H DQ-SQ combines several key advantages; $^{1}$H signals are detected in two different frequency dimensions, whereby the DQ signals originating from dipolar coupled $^{1}$H-$^{1}$H pairs are manifested as the sum of $^{1}$H SQ chemical shifts (see Figure 4.2, vertical DQ axis has a chemical shift range twice as larger as the horizontal SQ axis). The DQ intensities are characteristic to strength of dipolar interaction between specific $^{1}$H-$^{1}$H pairs, which manifest as on- and off-diagonal correlation peaks corresponding to chemically equivalent and distinct sites, respectively. This is illustrated with greater details in the previous studies.[166–168] A comparison of 2D $^{1}$H-$^{1}$H DQ-SQ correlation spectra of neat P4, P4:BCF and P4:F4TCNQ blends acquired with

20 microseconds of recoupling time is shown in Figure 4.2. For neat P4 polymer (Figure 4.2b), the broad distribution of $^{1}$H DQ peaks centered at ~3 ppm corresponds to dipolar coupled $^{1}$H-$^{1}$H pairs in alkyl sidechains. The off-diagonal DQ signals at 7.5 and 9.3 ppm are due to the dipolar interactions between sidechain and aromatic $^{1}$H-$^{1}$H pairs. The distribution of on-diagonal $^{1}$H DQ peaks in the range of 11-14 ppm (Figure 4.2b, solid oval) is attributable to the close $^{1}$H-$^{1}$H proximities in BT units of P4 polymer. Although the on-diagonal DQ peak associated with through-space H-H proximities in CPDT moieties is expected to resonate in the range 14-16 ppm, this peak is too weak to be detected due to weak inter- and intramolecular dipolar interactions between the thiophene protons. Nonetheless, a $^{1}$H DQ-SQ spectrum of neat P4 acquired with a large recoupling time of 40 microseconds (Appendix Figure 7.15a) shows weak signal intensity at ~15 ppm. In addition, the off-diagonal peak associated with the aromatic groups of P4 appear at 5.4 and 5.9 ppm on the SQ axis (DQ, 11.3 ppm) is attributable to the different local chemical environments of $^{1}$H sites with different aromatic ring current effects in the π-π stacked PDT units. In contrast to the pristine P4 material, the doped polymers display different DQ-SQ features whereby the aliphatic signals are detected with appreciable intensities but not the aromatic regions (Figures 4.2c-d, dashed ovals) indicating that the free radicals are closely associated with the aromatic moieties of P4 polymers. In addition, the $^{1}$H DQ coherences relax much faster than the SQ coherences, which may contribute to further signal intensity losses, particularly in the localities of the free radicals. This is further evaluated by examining horizontal line-cut spectra of 2D $^{1}$H DQ spectra of doped systems acquired with different recoupling times shown in Appendix (Figure 7.14, 7.15b-c). The weak intensity signals depicted in dashed ovals are either artifacts or any residual aromatic $^{1}$H DQ peaks originating from the undoped diamagnetic regions. This result is in line with the analysis of 1D $^{1}$H and $^{13}$C CP-MAS

spectra, although $^{1}$H DQ-SQ NMR notably allows observation of the specific moieties polymer impacted by the doping process. It can be reasoned that the different doping mechanisms and the presence of different radical species contribute to the intensity losses, as will be investigated by EPR techniques discussed below.

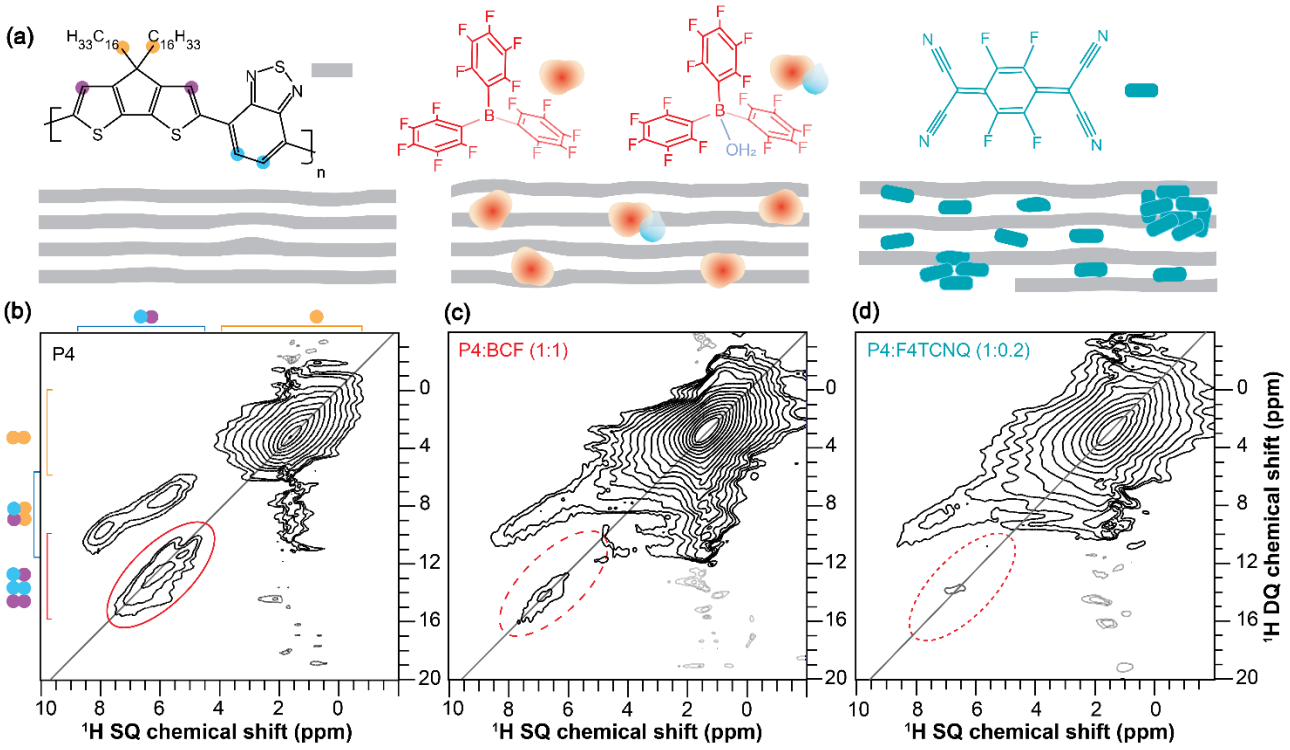


**Figure 4.2. Solid-state 2D $^{1}$H-$^{1}$H DQ-SQ correlation NMR spectra of (a) neat P4 (b) P4:BCF (1:1 molar equiv.) (c) P4:F4TCNQ (1:0.2 molar equiv.) indicating the signal intensity losses in the aromatic regions of doped P4 polymers. Weak intensity signals in the dashed oval are likely to be artefact or residual DQ signals originate from the undoped diamagnetic aromatic regions of the P4-dopant blends.**

2. Electron Paramagnetic Resonance

Information on the hyperfine structure and local chemical environments of dopants in organic semiconductors can be obtained by EPR spectroscopy,[165,169,170] which has a single-site resolution to investigate paramagnetic species. Figure 4.3 compares the X-band continuous-wave length (CW) EPR and pulsed EPR HYperfine Sublevel COrRElation (HYSCORE) spectra of P4,

P4:BCF and P4:F4TCNQ blends. The CW spectrum of P4 polymer (Figure 4.3a) shows a very week EPR signal with a 5 Gauss (G) linewidth centered at a g-factor of 2.0026 indicating the mobility of the delocalized electrons at minuscule concentrations. The addition of dopants to P4 induces a spike in the signal intensity and a dramatic change in the EPR linewidth that decreases to 1.7 G with a g-factor that resembles the free electron g-value. However, the P4:BCF blend leads to a relatively stronger EPR signal than the P4: F4TCNQ, consistent with the increased doping efficiency associated with the BCF molecules. More elaboratively, the localization of dopant molecules in P4 polymer network are analyzed by 2D-HYSCORE technique that provides information on the hyperfine interactions between electron and nuclear spins. The physical origins that contribute to hyperfine couplings are (i) anisotropic dipole-dipole interaction which depends on the relative orientation of magnetic moments, and (ii) isotropic fermi-contact interaction that arises when there is a finite spin density of the electron spin at the nucleus. For the neat P4 polymer, a weak fermi-contact hyperfine coupling associated with $^{1}H$ (14.5 MHz) with a maximum anti-diagonal ridge extent of 8.2 MHz is detected in the (+,+) quadrant (Figure 4.3b). In addition, weak hyperfine couplings associated with $^{13}C$ and with $^{14}N$ sites are observed. In the (-,+) quadrant of the same spectrum, the single-quantum and double-quantum signals associated with $^{14}N$ are observed as indicated by red arrows. By comparison, 2D HYSOCRE spectrum of P4:BCF (Figure 4.3c) exhibits weak hyperfine couplings with the two isotopes of boron $^{10}B$( $\upsilon$ = 1.6 MHz) and $^{11}B$ ($\upsilon$ = 4.8 MHz) on the diagonal (red arrows), and does not show an anti-diagonal signals, indicating that these hyperfine interactions arise purely from dipolar interaction. A well-resolved $^{19}F$ ($\upsilon$ =13.7 MHz) signal with a maximum hyperfine coupling of 2.1 MHz indicates that the fluorine atoms are spin polarized by the electrons, whereas the $^{1}H$ signal ($\upsilon$ =14.9 MHz) with a hyperfine coupling of 5 MHz (with an electron-$^{1}H$

distance greater than 0.4 nm) suggests that the bulky aromatic BCF molecules are located in the vicinity of P4 backbone moieties rather than intercalated between the π-π stacked P4 backbones. In the case of P4: F4TCNQ (Figure 4.3d), a $^{1}H$ signal at $\upsilon$=14.9 MHz originates from pure dipolar interaction with a vertical shift of 1.4 MHz with a distance of less than 0.38 nm between unpaired electron and 1H, as estimated based on the dipole single point approximation. This hyperfine coupling is within the regime of a typical π-π stacking interactions in conjugated polymers, suggesting that the F4TCNQ molecules are intercalated, at least in part, between the π-π stacked P4 polymers. Combined, 2D ssNMR and EPR results corroborate that the BCF and F4TCNQ molecules exhibit different intermolecular interactions with P4 polymer, leading to different doping mechanisms and efficiencies.

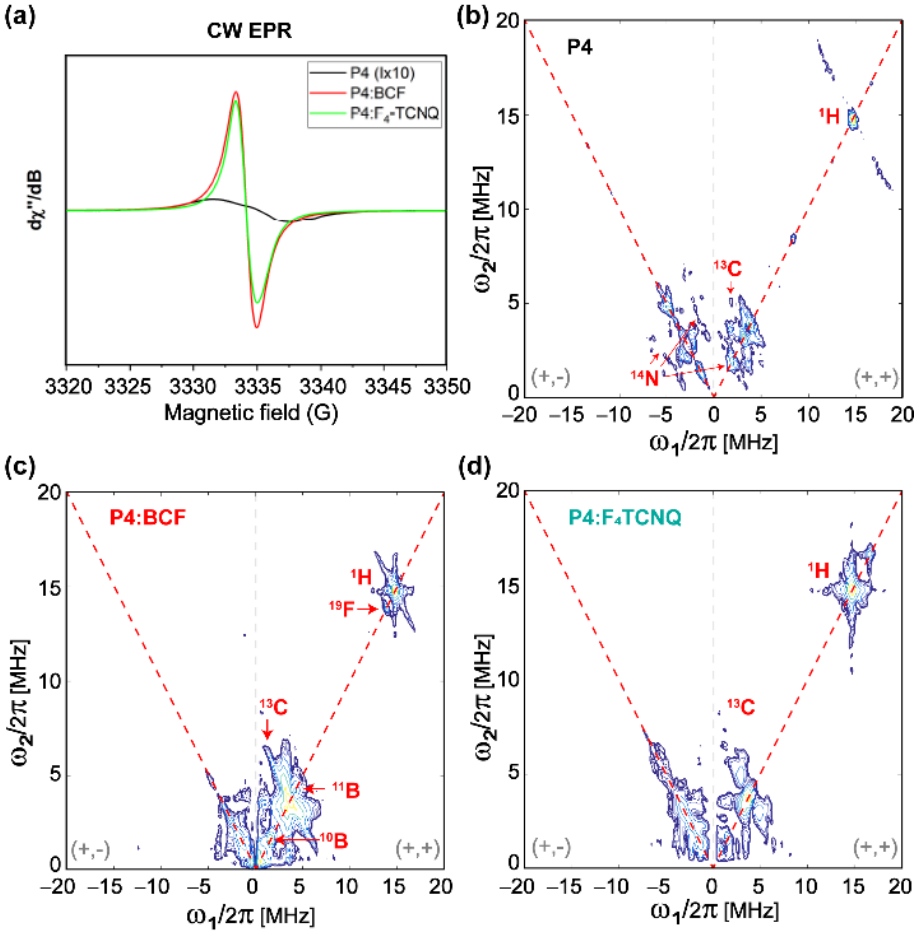


**Figure 4.3. Solid-state (a) continuous-wave EPR spectra of P4 and P4:dopant blends, and 2D HYSCORE spectra of (b) P4, (c) P4:BCF (1:1 molar equiv.) and (d) P4: F4TCNQ (1:0.2 molar equiv.) indicating the different hyperfine interactions between P4 and dopant molecules.**

Further insights into the different doping effects in P4:BCF and P4: F4TCNQ blends can be obtained by analyzing NMR longitudinal relaxation times ($T_1$) of $^1$H sites in P4 polymer. The presence of paramagnetic species in doped polymers influences the associated longitudinal relaxation ($T_1$) times of nuclear spins.[161] For neat P4 and P4:dopant blends, the $T_1$ relaxation times are given in Table 7.2. Aromatic $^1$H sites in P4:BCF show relatively longer $T_1$ values (~0.89 s) than the same sites in P4: F4TCNQ blend (0.03 s), indicating different nuclear spin relaxation behaviors in these blends. However, the P4:BCF-water complexes exhibit much shorter $T_1$ values for both alkyl and aromatic $^1$H sites. The different $T_1$ values are hypothesized to originate from different distributions of dopant molecules in the polymers and the different hyperfine interactions in the P4: F4TCNQ, P4:BCF and P4:BCF-water blends. Although the $^1$H $T_1$ relaxation measurements and analysis corroborate that the loss of $^1$H DQ signal intensities in P4:dopant blends (Figure 4.2c) is due to the presence of paramagnetic species in much closer proximity to the P4 backbone moieties (as confirmed by EPR analysis, Figure 4.3), further investigation of the factors that contribute to site-specific $T_1$ relaxation times is required to gain insight into the different relaxation behaviors in doped polymers.

By analyzing $^{11}$B (spin magnetic moment I = 3/2, and exhibits quadrupolar interaction) MAS NMR spectra of BCF and BCF:P4 bends, we provide further insight into the changes in the local chemical environments of BCF molecules upon addition to the P4 polymer. As seen in Figure 4.4a, 1D $^{11}$B spectra of neat BCF show a broad quadrupolar lineshape between 45-60 ppm produced by the tri-coordinated boron atoms in BCF, and a relatively narrow lineshape near 0 ppm attributed to tetracoordinated boron nuclei in BCF·$H_2O$ complex. As a result of the increased coordination number of boron, and reduced quadrupolar interactions, the tetracoordinated BCF·$H_2O$ complex exhibits a relatively narrow signal.[159,171] Although the neat

BCF material was stored in the nitrogen atmosphere of a glovebox, trace amounts of water present (or exposure to the ambient atmosphere during sample preparation for ssNMR studies) were enough to result in the BCF·$H_2O$ complex,[157] and different types of BCF-water complexes.[146] Upon addition to P4, there is further narrowing of the $^{11}B$ peak appearing at -4 ppm, which could be attributed to the BCF molecules embedded into the polymer chains and the hyperfine interactions between BCF-water/BCF·$OH^-$ and the P4 polymer radicals. Nevertheless, when a higher concentration of BCF is incorporated into the P4 polymer (1:1 molar ratio), an additional $^{11}B$ signal emerges at ~18 ppm, indicating the formation of additional BCF·water, BCF·$OH^-$ like or bridged complexes involving two BCF molecules.[146,157] It is noteworthy that the conjugated polymers with extended sidechains are lipophilic, and thus enhance moisture stability of BCF molecules embedded into the P4 polymer. Addition of water molecules promotes the formation of BCF·water and bridged complexes, which influence the doping efficiency of P4:BCF blend. To test this, we carried out $^{11}B$ and $^{1}H$ MAS NMR experiments as a function of the amount of water added to P4:BCF blend, whereby the $^{11}B$ signal at 15-19 ppm is detected with much higher intensity (Figure 4.4a). The $^{1}H$ NMR spectra also show the emergence of a water $^{1}H$ signal resonating at ~4.5 ppm (Figure 4.4b), and the $^{1}H$ signal integral values associated with aliphatic and aromatic protons (13.2 and 0.5) indicate further signal intensity loss upon addition of water to the P4:BCF blend (Table 7.1). In addition, a comparison of 1D X-band CW-EPR spectra of P4, P4: F4TCNQ, P4:BCF and P4:BCF+water complexes (Appendix 7.16) suggests that the P4:BCF-water complex has a relatively high concentration of radical species as indicated by the stronger signal intensity than the P4:BCF blend. The distinct EPR features of P4:BCF+water complex are due to the different local chemical environments of dopant molecules and hyperfine interactions between P4 and BCF-water complexes. Overall, this

analysis suggests that the increased concentrations of paramagnetic species are formed when a drop of water is added to the P4:BCF complex. This result is in line with our previous observation, whereby the addition of a drop of water to P4:BCF resulted in enhanced charge carrier mobility.[157] Conversely, when deuterated water ($D_2O$) is added to the P4:BCF blend, there is no such trend in the emergence of $^{11}B$ signal intensity (15-20 ppm) or the additional $^{1}H$ signal intensity loss in the aromatic regions of the $^{1}H$ MAS NMR spectra. It can be reasoned that the deuteration of water molecules can affect the formation of bridged BCF-water complexes (for example, large anions), due to the geometric isotopic effects on the hydrogen bonding interactions, which may ultimately influence the proton transfer process to the P4 polymer chains.

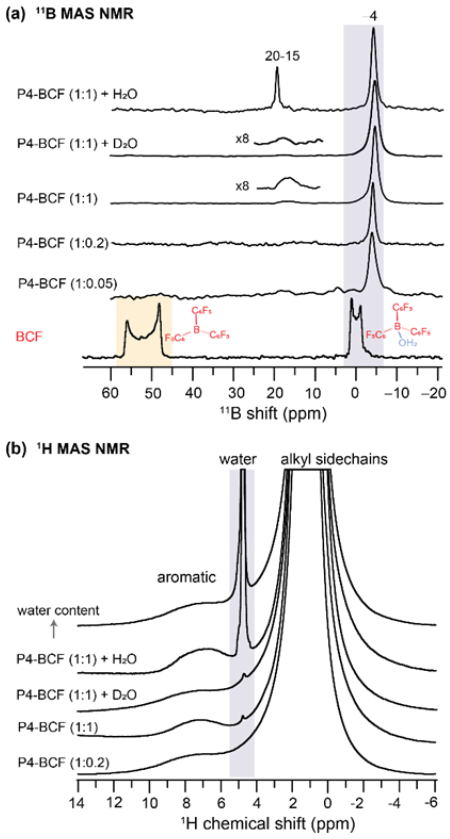


**Figure 4.4. 1D 11B MAS NMR spectra of (a) neat BCF, P4:BCF at different molar ratios and P4:BCF with a drop of added water and water-d. (b) 1H MAS NMR spectra of P4:BCF with and without added water or water-d. All spectra were acquired at 18.8 T (1H = 800.1 MHz, 11B = 256.7 MHz) at room temperature.**

From the 1D $^{19}$F NMR of neat F4TCNQ (Figure 4.5a), we observe two distinct peaks at –129 and –133 ppm corresponding to the unique local environments for fluorine atoms in the crystal structure of pure F4TCNQ.[172,173] For P4:F4TCNQ blends (1:0.02 and 1:0.2 molar ratios), the detection $^{19}$F signals is challenging due to minuscule concentrations of F4TCNQ molecules and longer $^{19}$F longitudinal relaxation delays of up to several minutes.[136] This is further exacerbated by the presence of delocalized electrons in the vicinity of intercalated F4TCNQ molecules between the polymer backbones, as revealed by the EPR analysis as well as the intensity loss in the $^{1}$H NMR spectrum of P4:F4TCNQ shown in Figure 4.2. Here we use a spin-echo filter to

suppress background signals from the NMR probe, and a large number of transients were coadded (1600 scans) to acquire the $^{19}F$ spectrum of P4:F4TCNQ (1:0.02) in order to identify two distinct $^{19}F$ signals at −128 and −150 ppm. Further addition of F4TCNQ (0.2 molar equivalents) produces two additional local environments for fluorine nuclei, resulting in partially resolved peaks at −134, −135, −138 and −143 ppm. Although $^{19}F$ signals correspond to fully doped P4:F4TCNQ regions (i.e., intercalated F4TCNQ molecules) may not be observed in ssNMR experiments,[136] the NMR-detected $^{19}F$ signals are expected to originate from the nonconducting regions and/or locally aggregated F4TCNQ molecules in the proximity of lamellar regions.[139] The combined ssNMR and EPR results suggest that F4TCNQ molecules are distributed into different local chemical environments in P4 polymer, and some of which, but not all, are involved in doping process. However, from the 1D $^{19}F$ ssNMR data alone we cannot discern which peaks would correspond to backbone intercalated, crystalline or disordered aggregates of F4TCNQ molecules in P4:F4TCNQ blends. To further resolve these signals, we used a spin-echo filter[174] of 10 μs that suppresses the signals from probe background and a series of 1D $^{19}F$ NMR spectra (Figure 4.5b) were acquired by varying longitudinal relaxation delays in the range of 0.5 to 50 s. This experiment allows fast and slow relaxing $^{19}F$ sites in aggregated and ordered F4TCNQ molecules to be distinguished and identified. The distribution of F4TCNQ molecules closely associated with P4 backbone moieties produce broad peaks at −143 and −134 ppm, visible after short relaxation delay (0.5 s), whereas aggregated F4TCNQ results in narrow signals at −138 and −135 ppm which were detected at higher intensities when a relaxation delay of greater than 20 s is used. It is noteworthy that these relaxation delays are much smaller than the $T_1$ relaxation delays of neat F4TCNQ (up to 600s), suggesting that the added F4TCNQ

molecules to P4 polymer exhibit different local structures and dynamics than the pristine F4TCNQ. For example, literature reports detail F4TCNQ aggregate formation at high doping concentrations, and can be avoided at low dopant concentrations.[148,175] This trend is observed in the P4:F4TCNQ system as revealed by the additional 1D $^{19}$F NMR experiment carried out for a lower P4:F4TCNQ molar ratio of 1.0:0.02 (Figure 4.5a), which showed only the peaks near −128 and −150 ppm. These $^{19}$F chemical shifts are identical to those reported earlier, which correspond to dopant molecules located in the vicinity of the P4 backbone moieties, further supporting the assignments made by the spin echo experiments.

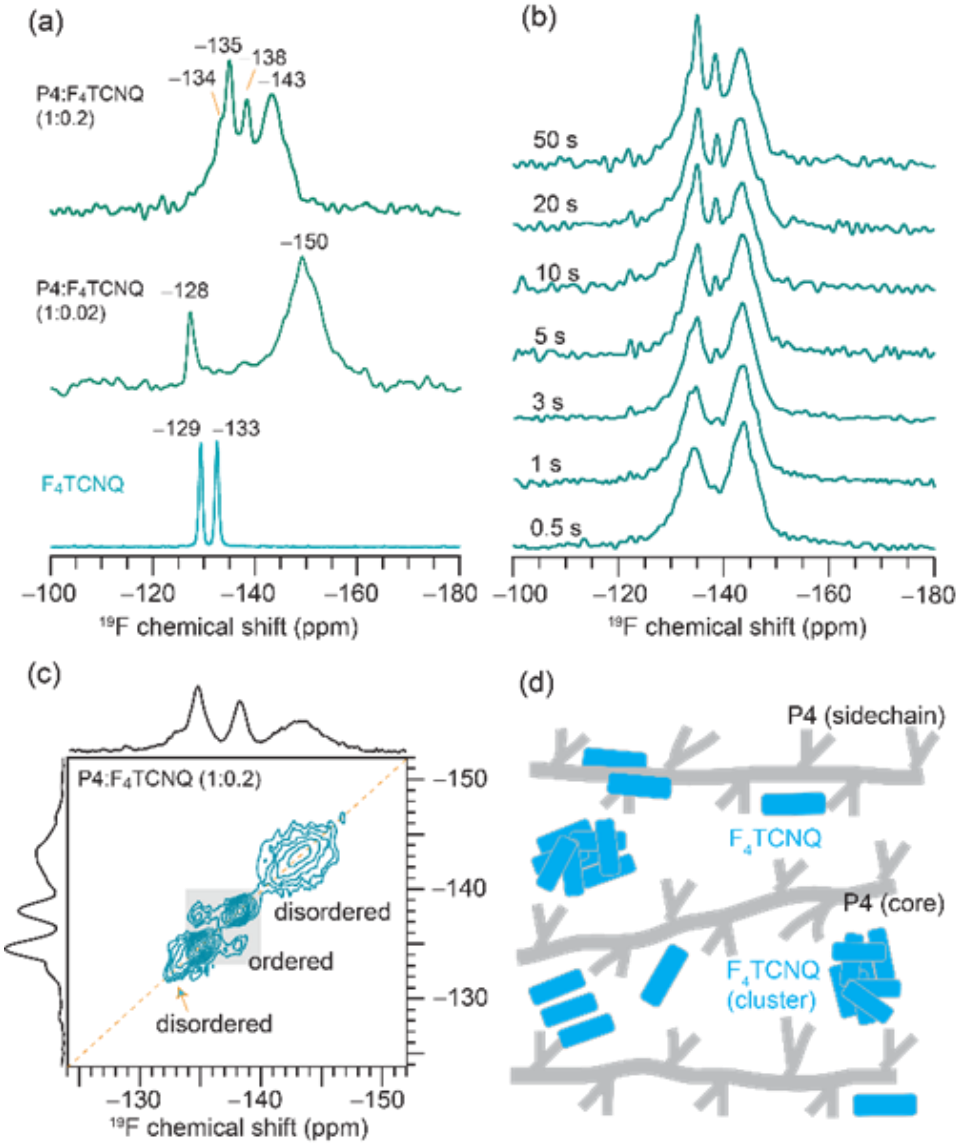


**Figure 5.5. Solid-state (a) 1D $^{19}$F MAS NMR spectra of neat F4TCNQ and P4:F4TCNQ blends with different F4TCNQ molar ratios, and (b) $T_2$-filered $^{19}$F MAS NMR spectra P4:F4TCNQ (1:0.2) as a function of spin-echo time, and 2D (c) $^{19}$F-$^{19}$F spin-diffusion NMR spectrum of P4:F4TCNQ (1:0.2) acquired with 500 ms mixing time. (d) schematic representation of different distributions of F4TCNQ molecules in P4 polymer chains.**

Correspondingly, 2D $^{19}$F-$^{19}$F spin diffusion measurements also provided resolution of the aggregated and distributed F4TCNQ molecules in the doped P4 polymer (Figure 4.5c-d). These experiments use a spin-diffusion delay (also referred to as mixing time) to allow magnetization

exchange between dipolar coupled $^{19}F$ spins. A small mixing time of 10 ms is not enough for the exchange of magnetization between $^{19}F$ sites (Figure 7.17, Appendix), resulting in only self-correlation (on-diagonal) peaks which appear along the diagonal. The longer spin diffusion time of 500 ms allows a markedly different spectrum to be obtained, showing cross-correlation peaks between the signals at −138 and −135 ppm on both axes, which indicates spin magnetization exchange between chemically distinct $^{19}F$ nuclei in the F4TCNQ aggregates. In contrast, the lack of cross (off-diagonal) peaks between intercalated (or closely associated with the P4 backbone) $^{19}F$ nuclei producing peaks at −143 ppm and those in the aggregates producing peaks at −135 suggests these two $^{19}F$ sites are too distant or locally disordered to allow for spin magnetization exchange between them. F4TCNQ aggregation in the blend and the partial disruption of the P4 backbone by F4TCNQ explain the lower doping efficiency observed in P4: F4TCNQ films (< 4%). Further analysis of cooperative interactions that drive molecular self-assembly in OSCs are expected to help to understand the aggregation behaviors of small molecular dopants in polymers.[176]

Owing to the inherently heterogeneous chemical nature, the π-conjugated polymers and their blends represent a characterization challenge. The addition of dopant molecules causes changes to the molecular self-assembly and local structures at sub-nanometer distances, which are often difficult to analyze by X-ray scattering and microscopy techniques, and insights offered by infrared spectroscopy are also limited. On the other hand, electroanalytical and UV-visible spectroscopy techniques which provide information on the macroscopic changes such as conductivity and optical absorption do not resolve atomic-level structures and interactions. Therefore, it is less straightforward to reach a consensus about structure-property relationships. To this end, ssNMR and EPR analysis presented here enabled the specific moieties of doped

polymers impacted such as backbone and sidechain structures, and hyperfine interactions to be identified and distinguished. Our results indicate that the addition of F4TCNQ and BCF to P4 polymer lead to different intermolecular interactions and structural changes due to different doping mechanisms. Some of the F4TCNQ molecules, but not all, dope the P4 polymer by forming charge transfer complexes (free radicals that can be detected by EPR and confirmed by the signal intensity loss in the aromatic $^{1}$H NMR spectra of P4 polymer), and the self-aggregated F4TCNQ molecules distributed within the polymer network can be analyzed by $^{19}$F MAS NMR and relaxation measurements. In addition, ssNMR and EPR analysis provide essential insights into the BCF-doped P4 polymers that exhibit an entirely different doping mechanism, whereby BCF molecules interact with traces of water molecules to serve as Brønsted acid sites to transfer a proton to P4 polymer leading $BCF{\cdot}OH^-$ and other BCF-water Brønsted acid complexes that are detected by $^{11}$B MAS NMR. These magnetic resonance techniques present several opportunities and obvious challenges for the study of doped polymers. For example, it is less straightforward to distinguish between the doped and undoped polymer regions and polymer-dopant interfaces precisely and quantitively. It is also difficult to determine the domain sizes and shapes of the doped and undoped polymers due to the short-range nature of both EPR and NMR techniques. More generally, polymer blends consisting of dia- and paramagnetic species lead to signal broadening due to several short and long-range interactions such as Fermi contact, pseudocontact, anisotropic bulk magnetic susceptibility (ABMS)-induced shifts, as well as the dipolar contributions and locally disordered regions, which are additive, and deconvolution of these factors to rationalize the NMR peak broadening requires the ability to quantify them separately.

## V. References


1. Knupfer, M., Fink, J., Zojer, E. & Leising, G. Localized and delocalized singlet excitons in ladder-type poly(paraphenylene). *Phys. Rev. B* **57**, R4202 (1998).
2. Alvarado, S. F., Seidler, P. F., Lidzey, D. G. & Bradley, D. D. C. Direct Determination of the Exciton Binding Energy of Conjugated Polymers Using a Scanning Tunneling Microscope. *Phys. Rev. Lett.* **81**, 1082 (1998).
3. Barth, S. & Bässler, H. Intrinsic Photoconduction in PPV-Type Conjugated Polymers. *Phys. Rev. Lett.* **79**, 4445 (1997).
4. Hill, I. G., Kahn, A., Soos, Z. G. & Pascal, R. A. Charge-separation energy in films of π-conjugated organic molecules. *Chem. Phys. Lett.* **327**, 181–188 (2000).
5. Salzmann, I., Heimel, G., Oehzelt, M., Winkler, S. & Koch, N. Molecular Electrical Doping of Organic Semiconductors: Fundamental Mechanisms and Emerging Dopant Design Rules. *Acc. Chem. Res.* **49**, 370–378 (2016).
6. Méndez, H., et al. Charge-transfer crystallites as molecular electrical dopants. *Nat. Commun.* **6**, 8560 (2015).
7. Méndez, H., et al. Doping of Organic Semiconductors: Impact of Dopant Strength and Electronic Coupling. *Angew. Chemie Int. Ed.* **52**, 7751–7755 (2013).
8. Yurash, B., et al. Towards understanding the doping mechanism of organic semiconductors by Lewis acids. *Nat. Mater.* , DOI:10.1038/s41563-019-0479-0.
9. Gao, J., et al. The effect of 2,3,5,6-tetrafluoro-7,7,8,8-tetracyanoquinodimethane charge transfer dopants on the conformation and aggregation of poly(3-hexylthiophene). *J. Mater. Chem. C* 5638–5646 (2013).
10. Tyler Scholes, D., et al. Overcoming Film Quality Issues for Conjugated Polymers Doped with F4TCNQ by Solution Sequential Processing: Hall Effect, Structural, and Optical Measurements. *J. Phys. Chem. Lett.* **6**, 4786–4793 (2015).
11. Zalar, P., et al. Increased mobility induced by addition of a lewis acid to a lewis basic conjugated polymer. *Adv. Mater.* **26**, 724–727 (2014).
12. Dixon, A. L., Vezin, H., Nguyen, T. Q. & Reddy, G. N. M. Structural insights into Lewis acid- and F4TCNQ-doped conjugated polymers by solid-state magnetic resonance spectroscopy. *Mater. horizons* **9**, 981–990 (2022).
13. Zhou, J., Liu, Q., Feng, W., Sun, Y. & Li, F.*Chem. Rev.*, 2015, 115, 395–465.
14. Yurash, B., et al. Efficiency of Thermally Activated Delayed Fluorescence Sensitized Triplet Upconversion Doubled in Three-Component System. *Adv. Mater.* **34**, 1–9 (2022).
15. Xu, C. & Webb, W. W. Measurement of two-photon excitation cross sections of molecular fluorophores with data from 690 to 1050 nm. *J. Opt. Soc. Am. B* , DOI:10.1364/josab.13.000481.
16. Keivanidis, P. E., Baluschev, S., Lieser, G. & Wegner, G. Inherent photon energy recycling effects in the upconverted delayed luminescence dynamics of poly(fluorene)-pt"octaethyl porphyrin blends. *ChemPhysChem* **10**, 2316–2326 (2009).
17. Singh-Rachford, T. N. & Castellano, F. N. Triplet sensitized red-to-blue photon upconversion. *J. Phys. Chem. Lett.* **1**, 195–200 (2010).
18. Deng, F., Sommer, J. R., Myahkostupov, M., Schanze, K. S. & Castellano, F. N. Near-IR phosphorescent metalloporphyrin as a photochemical upconversion sensitizer. *Chem. Commun.* **49**, 7406–7408 (2013).

19. Yang, L., et al. Photon-upconverters for blue organic light-emitting diodes: A low-cost, sky-blue example. *Nanoscale Adv.* **4**, 1318–1323 (2022).
20. Li, D., et al. Near-Infrared to Visible Organic Upconversion Devices Based on Organic Light-Emitting Field Effect Transistors. *ACS Appl. Mater. Interfaces* , DOI:10.1021/acsami.7b10538.
21. C., A., Pahlevani, M. & Welch, G. C.*Mater. Adv.*, 2021, 2, 628–645.
22. Gaspar, D. J. & Polikarpov, E. *OLED fundamentals: Materials, devices, and processing of organic light-emitting diodes*. (CRC Press, 2015).
23. Adachi, C., Baldo, M. A., Thompson, M. E. & Forrest, S. R. Nearly 100% internal phosphorescence efficiency in an organic light-emitting device. *J. Appl. Phys.* **90**, 5048–5051 (2001).
24. Baldo, M. A., et al. Highly efficient phosphorescent emission from organic electroluminescent devices. *Nature* **395**, 151–154 (1998).
25. Reineke, S. & Baldo, M. A. Recent progress in the understanding of exciton dynamics within phosphorescent OLEDs. *Phys. Status Solidi Appl. Mater. Sci.* **209**, 2341–2353 (2012).
26. Freidzon, A. Y., et al. Predicting the Operational Stability of Phosphorescent OLED Host Molecules from First Principles: A Case Study. *J. Phys. Chem. C* **121**, 22422–22433 (2017).
27. Qiao, X. & Ma, D. Nonlinear optoelectronic processes in organic optoelectronic devices: Triplet-triplet annihilation and singlet fission. *Mater. Sci. Eng. R Reports* **139**, 100519 (2020).
28. Chen, W., et al. Red-to-blue photon up-conversion with high efficiency based on a TADF fluorescein derivative. *Chem. Commun.* **55**, 4375–4378 (2019).
29. Wu, T. C., Congreve, D. N. & Baldo, M. A. Solid state photon upconversion utilizing thermally activated delayed fluorescence molecules as triplet sensitizer. *Appl. Phys. Lett.* , DOI:10.1063/1.4926914.
30. Hong, G., et al. A Brief History of OLEDs—Emitter Development and Industry Milestones. *Adv. Mater.* , DOI:10.1002/adma.202005630.
31. Raj, B., Kaur, P., Kumar, P. & Gill, S. S. Comparative Analysis of OFETs Materials and Devices for Sensor Applications. *Silicon* **14**, 4463–4471 (2022).
32. Luo, L. & Liu, Z. Recent progress in organic field-effect transistor-based chem/bio-sensors. *View* **3**, 20200115 (2022).
33. Nasri, A., Pétrissans, M., Fierro, V. & Celzard, A. Gas sensing based on organic composite materials: Review of sensor types, progresses and challenges. *Mater. Sci. Semicond. Process.* **128**, 105744 (2021).
34. Alam, S., Raman, A., Raj, B., Kumar, N. & Singh, S. Design and Analysis of Gate Overlapped/Underlapped NWFET Based Lable Free Biosensor. *Silicon* , DOI:10.1007/s12633-020-00880-w.
35. Su, Y., et al.*Nanoscale Res. Lett.*, 2020, 15.
36. Yuvaraja, S., et al. Organic field-effect transistor-based flexible sensors. *Chem. Soc. Rev.* **49**, 3423–3460 (2020).
37. Zhang, J., et al. Highly Conducting Polythiophene Thin Films with Less Ordered Microstructure Displaying Excellent Thermoelectric Performance. *Macromol. Rapid Commun.* **39**, 1–8 (2018).

38. Yu, Y., et al. Small-Molecule-Based Organic Field-Effect Transistor for Nonvolatile Memory and Artificial Synapse. *Adv. Funct. Mater.* **29**, 1–31 (2019).
39. Rivnay, J., et al. Organic electrochemical transistors. *Nat. Rev. Mater. 2018 32* **3**, 1–14 (2018).
40. Blom, P. W. M. Polymer Electronics: To Be or Not to Be?. *Adv. Mater. Technol.* **5**, 1–14 (2020).
41. Singh, T. B. & Sariciftci, N. S. Progress in plastic electronics devices. *Annu. Rev. Mater. Res.* , DOI:10.1146/annurev.matsci.36.022805.094757.
42. Liu, K., Ouyang, B., Guo, X., Guo, Y. & Liu, Y. Advances in flexible organic field-effect transistors and their applications for flexible electronics. *npj Flex. Electron.* , DOI:10.1038/s41528-022-00133-3.
43. Mandal, S., et al. Low Operating Voltage Organic Field-Effect Transistors with Gelatin as a Moisture-Induced Ionic Dielectric Layer: The Issues of High Carrier Mobility. *ACS Appl. Mater. Interfaces* **12**, 19727–19736 (2020).
44. Schwabegger, G., et al. High mobility, low voltage operating C60 based n-type organic field effect transistors. *Synth. Met.* **161**, 2058–2062 (2011).
45. Zhang, X.-H., et al. High performance organic field-effect transistors using high-K dielectrics grown by atomic layer deposition (ALD). *Org. Field-Effect Transistors VI* **6658**, 66580T (2007).
46. Ledwon, P., Wiosna-Salyga, G., Chapran, M. & Motyka, R. The effect of acceptor structure on emission color tuning in organic semiconductors with D–π–A–π–D structures. *Nanomaterials* **9**, 1–19 (2019).
47. Qin, Z., et al. Molecular doped organic semiconductor crystals for optoelectronic device applications. *J. Mater. Chem. C* **8**, 14996–15008 (2020).
48. Yurash, B., et al. Atomic-Level Insight into the Postsynthesis Band Gap Engineering of a Lewis Base Polymer Using Lewis Acid Tris(pentafluorophenyl)borane. *Chem. Mater.* , DOI:10.1021/acs.chemmater.9b01224.
49. States, U., Application, P., Code, K. & Guillermo, C. Band gap control in conjugated oligomers and polymers via Lewis acids. *J. Am. Chem. Soc.* 1–32 (2013).
50. Zalar, P., Henson, Z. B., Welch, G. C., Bazan, G. C. & Nguyen, T. Q. Color tuning in polymer light-emitting diodes with lewis acids. *Angew. Chemie - Int. Ed.* **51**, 7495–7498 (2012).
51. Emmott, C. J. M., et al. Organic photovoltaic greenhouses: A unique application for semi-transparent PV?. *Energy Environ. Sci.* **8**, 1317–1328 (2015).
52. Brus, V. V., et al.*Adv. Mater.*, 2019, 31, 1900904.
53. Huynh, W. U., Dittmer, J. J. & Alivisatos, A. P. Hybrid nanorod-polymer solar cells. *Science (80-. ).* , DOI:10.1126/science.1069156.
54. Hiramoto, M., Fujiwara, H. & Yokoyama, M. Three-layered organic solar cell with a photoactive interlayer of codeposited pigments. *Appl. Phys. Lett.* , DOI:10.1063/1.104423.
55. Zhang, M., et al. Single-layered organic photovoltaics with double cascading charge transport pathways: 18% efficiencies. *Nat. Commun.* **12**, 1–10 (2021).
56. Chen, W., Nikiforov, M. P. & Darling, S. B. Morphology characterization in organic and hybrid solar cells. *Energy Environ. Sci.* **5**, 8045–8074 (2012).
57. Koster, L. J. A., Smits, E. C. P., Mihailetchi, V. D. & Blom, P. W. M. Device model for the operation of polymer/fullerene bulk heterojunction solar cells. *Phys. Rev. B - Condens.*

*Matter Mater. Phys.* , DOI:10.1103/PhysRevB.72.085205.
58. Köhler, A. & Bässler, H. *Electronic processes in organic semiconductors: An introduction*. (Wiley-VCH Verlag GmbH, 2015).
59. Brabec, C. J., Sariciftci, N. S. & Hummelen, J. C. Plastic Solar Cells. *Adv. Funct. Mater.* **11**, 15–26 (2001).
60. Sariciftci, N. S., Smilowitz, L., Heeger, A. J. & Wudl, F. Photoinduced electron transfer from a conducting polymer to buckminsterfullerene. *Science (80-. ).* **258**, 1474–1476 (1992).
61. Brabec, C. J., et al. Tracing photoinduced electron transfer process in conjugated polymer/fullerene bulk heterojunctions in real time. *Chem. Phys. Lett.* , DOI:10.1016/S0009-2614(01)00431-6.
62. Uoyama, H., Goushi, K., Shizu, K., Nomura, H. & Adachi, C. Highly efficient organic light-emitting diodes from delayed fluorescence. *Nature* **492**, 234–238 (2012).
63. Kretzschmar, A., Patze, C., Schwaebel, S. T. & Bunz, U. H. F. Development of Thermally Activated Delayed Fluorescence Materials with Shortened Emissive Lifetimes. *J. Org. Chem.* **80**, 9126–9131 (2015).
64. Yanai, N., et al. Absolute Method to Certify Quantum Yields of Photon Upconversion via Triplet-Triplet Annihilation. *J. Phys. Chem. A* **123**, 10197–10203 (2019).
65. Khitrin, A. & Fung, B. M. Design of heteronuclear decoupling sequences for solids. *J. Chem. Phys.* **112**, 2392–2398 (2000).
66. Schnell, I. & Spiess, W. H.*J. Magn. Reson.*, 2001, 151, 153–227.
67. Manjunatha Reddy, G. N., Malon, M., Marsh, A., Nishiyama, Y. & Brown, S. P. Fast magic-angle spinning three-dimensional nmr experiment for simultaneously probing HH and NH proximities in solids. *Anal. Chem.* **88**, 11412–11419 (2016).
68. Hong, Y. lee, Manjunatha Reddy, G. N. & Nishiyama, Y.*Solid State Nucl. Magn. Reson.*, 2020, 106.
69. Reddy, G. N. M., et al.*Chem. - A Eur. J.*, 2017, 23, 2235.
70. Karki, A., et al. Understanding the High Performance of over 15% Efficiency in Single-Junction Bulk Heterojunction Organic Solar Cells. *Adv. Mater.* 1903868 (2019).
71. Karki, A., et al. The role of bulk and interfacial morphology in charge generation, recombination, and extraction in non-fullerene acceptor organic solar cells. *Energy Environ. Sci.* **13**, 3679–3692 (2020).
72. Baride, A., Sigdel, G., Cross, W. M., Kellar, J. J. & May, P. S. Near infrared-to-near infrared upconversion nanocrystals for latent fingerprint development. *ACS Appl. Nano Mater.* **2**, 4518–4527 (2019).
73. Kim, J., et al. Rapid and background-free detection of avian influenza virus in opaque sample using NIR-to-NIR upconversion nanoparticle-based lateral flow immunoassay platform. *Biosens. Bioelectron.* **112**, 209–215 (2018).
74. Sedlmeier, A., Achatz, D. E., Fischer, L. H., Gorris, H. H. & Wolfbeis, O. S. Photon upconverting nanoparticles for luminescent sensing of temperature. *Nanoscale* **4**, 7090–7096 (2012).
75. Yildiz, D., et al. Anti-Stokes Stress Sensing: Mechanochemical Activation of Triplet–Triplet Annihilation Photon Upconversion. *Angew. Chemie - Int. Ed.* **58**, 12919–12923 (2019).
76. Bharmoria, P., Bildirir, H. & Moth-Poulsen, K. Triplet-triplet annihilation based near

infrared to visible molecular photon upconversion. *Chem. Soc. Rev.* **49**, 6529–6554 (2020).
77. Morifuji, T., Takekuma, Y. & Nagata, M. Integrated Photon Upconversion Dye-Sensitized Solar Cell by Co-adsorption with Derivative of Pt-Porphyrin and Anthracene on Mesoporous TiO2. *ACS Omega* **4**, 11271–11275 (2019).
78. Parker, C. A. & Hatchard, C. G. Delayed fluorescence from solutions of anthracene and phenanthrene. *Proc. Chem. Soc*. 147 (1962).
79. Wieghold, S. & Nienhausi, L. Engineering 3D perovskites for photon interconversion applications. *PLoS One* **15**, 34–37 (2020).
80. Sittig, M., et al. Fluorescence upconversion by triplet-triplet annihilation in all-organic poly(methacrylate)-terpolymers. *Phys. Chem. Chem. Phys.* **22**, 4072–4079 (2020).
81. Zhou, Y., Castellano, F. N., Schmidt, T. W. & Hanson, K. On the Quantum Yield of Photon Upconversion via Triplet-Triplet Annihilation. *ACS Energy Lett.* **5**, 2322–2326 (2020).
82. Duan, P., Yanai, N. & Kimizuka, N. Photon upconverting liquids: Matrix-free molecular upconversion systems functioning in air. *J. Am. Chem. Soc.* **135**, 19056–19059 (2013).
83. Wang, B., et al. Efficient triplet sensitizers of palladium(II) tetraphenylporphyrins for upconversion-powered photoelectrochemistry. *J. Phys. Chem. C* **118**, 1417–1425 (2014).
84. Kim, J. H., Deng, F., Castellano, F. N. & Kim, J. H. High efficiency low-power upconverting soft materials. *Chem. Mater.* **24**, 2250–2252 (2012).
85. Atkins, P. & Paula, J. De. *Physical Chemistry: Thermodynamics, Structure, and Change*. 2006).
86. Pristash, S. R., Corp, K. L., Rabe, E. J. & Schlenker, C. W. Heavy-Atom-Free Red-to-Yellow Photon Upconversion in a Thiosquaraine Composite. *ACS Appl. Energy Mater.* **3**, 19–28 (2020).
87. Parker, C. A. & Hatchard, C. G. Triplet-singlet emission in fluid solutions. Phosphorescence of eosin. *Trans. Faraday Soc.* **57**, 1894–1904 (1961).
88. Maciejewski, A., Szymanski, M. & Steer, R. P. Thermally activated delayed S1 fluorescence of aromatic thiones. *J. Phys. Chem.* **90**, 6314–6318 (1986).
89. Endo, A., et al. Thermally activated delayed fluorescence from Sn4+-porphyrin complexes and their application to organic light-emitting diodes -A novel mechanism for electroluminescence. *Adv. Mater.* **21**, 4802–4806 (2009).
90. Uoyama, H., Goushi, K., Shizu, K., Nomura, H. & Adachi, C. Highly efficient organic light-emitting diodes from delayed fluorescence. *Nature* **492**, 234–238 (2012).
91. Lee, D. R., et al. Above 30% external quantum efficiency in green delayed fluorescent organic light-emitting diodes. *ACS Appl. Mater. Interfaces* **7**, 9625–9629 (2015).
92. Lee, Y. H., et al. High-Efficiency Sky Blue to Ultradeep Blue Thermally Activated Delayed Fluorescent Diodes Based on Ortho-Carbazole-Appended Triarylboron Emitters: Above 32% External Quantum Efficiency in Blue Devices. *Adv. Opt. Mater.* **6**, 1–10 (2018).
93. Zeng, W., et al. Achieving Nearly 30% External Quantum Efficiency for Orange–Red Organic Light Emitting Diodes by Employing Thermally Activated Delayed Fluorescence Emitters Composed of 1,8-Naphthalimide-Acridine Hybrids. *Adv. Mater.* **30**, 1–8 (2018).
94. Li, B., et al. Highly efficient blue organic light-emitting diodes from pyrimidine-based thermally activated delayed fluorescence emitters. *J. Mater. Chem. C* **6**, 2351–2359

(2018).
95. Nakanotani, H., Masui, K., Nishide, J., Shibata, T. & Adachi, C. Promising operational stability of high-efficiency organic light-emitting diodes based on thermally activated delayed fluorescence. *Sci. Rep.* **3**, 2–6 (2013).
96. Yeh, T. C., et al. New naphthyridine-based bipolar host materials for thermally activated delayed fluorescent organic light-emitting diodes. *Org. Electron.* **70**, 55–62 (2019).
97. Wang, S., et al. Achieving high power efficiency and low roll-off OLEDs based on energy transfer from thermally activated delayed excitons to fluorescent dopants. *Chem. Commun.* **51**, 11972–11975 (2015).
98. Kim, B. S., Yook, K. S. & Lee, J. Y. Above 20% external quantum efficiency in novel hybrid white organic light-emitting diodes having green thermally activated delayed fluorescent emitter. *Sci. Rep.* **4**, 1–6 (2014).
99. Yurash, B., et al. Photoluminescence Quenching Probes Spin Conversion and Exciton Dynamics in Thermally Activated Delayed Fluorescence Materials. *Adv. Mater.* **31**, 1804490 (2019).
100. Yanai, N., et al. Increased vis-to-UV upconversion performance by energy level matching between a TADF donor and high triplet energy acceptors. *J. Mater. Chem. C* **4**, 6447–6451 (2016).
101. Ogawa, T., et al. Donor-Acceptor-Collector Ternary Crystalline Films for Efficient Solid-State Photon Upconversion. *J. Am. Chem. Soc.* **140**, 8788–8796 (2018).
102. Kim, K. & Jordan, K. D. Comparison of density functional and MP2 calculations on the water monomer and dimer. *J. Phys. Chem.* **98**, 10089–10094 (1994).
103. Stephen, P. J., Devlin, F. J., Chabalowski, C. F. & Frisch, M. J. Ab Initio Calculation of Vibrational Absorption. *J. Phys. Chem.* **98**, 11623–11627 (1994).
104. Berlman, I. B. Handbook of Fluorescence Spectra of Aromatic Molecules. *Handb. Fluoresc. Spectra Aromat. Mol.* , DOI:10.1016/b978-0-12-092656-5.x5001-1.
105. Monguzzi, A., Mézyk, J., Scotognella, F., Tubino, R. & Meinardi, F. Upconversion-induced fluorescence in multicomponent systems: Steady-state excitation power threshold. *Phys. Rev. B - Condens. Matter Mater. Phys.* **78**, 2–6 (2008).
106. Durandin, N. A., et al. Critical Sensitizer Quality Attributes for Efficient Triplet-Triplet Annihilation Upconversion with Low Power Density Thresholds. *J. Phys. Chem. C* **123**, 22865–22872 (2019).
107. Yanai, N. & Kimizuka, N. Recent emergence of photon upconversion based on triplet energy migration in molecular assemblies. *Chem. Commun.* **52**, 5354–5370 (2016).
108. Lüssem, B., Riede, M. & Leo, K. *Doping of organic semiconductors*. (John Wiley & Sons, Ltd, 2013).
109. Euvrard, J., Yan, Y. & Mitzi, D. B. Electrical doping in halide perovskites. *Nat. Rev. Mater.* **6**, 531–549 (2021).
110. Shirakawa, H., Louis, E. J., MacDiarmid, A. G., Chiang, C. K. & Heeger, A. J. Synthesis of electrically conducting organic polymers: Halogen derivatives of polyacetylene, (CH)x. *J. Chem. Soc. Chem. Commun.* **36**, 578–580 (1977).
111. Yamamoto, Y., Yoshino, K. & Inuishi, Y. Electrical Properties of Phthalocyanine-Halogen Complexes. *J. Phys. Soc. Japan* **47**, 1887–1891 (1979).
112. Parthasarathy, G., Shen, C., Kahn, A. & Forrest, S. R. Lithium doping of semiconducting organic charge transport materials. *J. Appl. Phys.* **89**, 4986–4992 (2001).

113. Pfeiffer, M., et al. Doped organic semiconductors: Physics and application in light emitting diodes. *Org. Electron.* **4**, 89–103 (2003).
114. Walzer, K., Männig, B., Pfeiffer, M. & Leo, K. Highly efficient organic devices based on electrically doped transport layers. *Chem. Rev.* **107**, 1233–1271 (2007).
115. Han, Y., et al. Doping of Large Ionization Potential Indenopyrazine Polymers via Lewis Acid Complexation with Tris(pentafluorophenyl)borane: A Simple Method for Improving the Performance of Organic Thin-Film Transistors. *Chem. Mater.* **28**, 8016–8024 (2016).
116. Paterson, A. F., et al. Addition of the Lewis Acid Zn(C6F5)2 Enables Organic Transistors with a Maximum Hole Mobility in Excess of 20 cm2 V−1 s−1. *Adv. Mater.* **31**, 1–8 (2019).
117. Basu, A., et al. Impact of p-type doping on charge transport in blade-coated small-molecule:polymer blend transistors. *J. Mater. Chem. C* **8**, 15368–15376 (2020).
118. An, M. H., et al. Controllable molecular doping in organic single crystals toward high-efficiency light-emitting devices. *Org. Electron.* **91**, 106089 (2021).
119. Lin, Y., et al. 17.1% Efficient Single-Junction Organic Solar Cells Enabled by n-Type Doping of the Bulk-Heterojunction. *Adv. Sci.* **7**, 1–9 (2020).
120. Salzmann, I., Heimel, G., Oehzelt, M., Winkler, S. & Koch, N.*Acc. Chem. Res.*, 2016, 49, 370–378.
121. Deschler, F., et al. Imaging of morphological changes and phase segregation in doped polymeric semiconductors. *Synth. Met.* **199**, 381–387 (2015).
122. Li, J., et al. Introducing Solubility Control for Improved Organic P-Type Dopants. *Chem. Mater.* **27**, 5765–5774 (2015).
123. Duong, D. T., et al. Direct observation of doping sites in temperature-controlled, p-doped p3ht thin films by conducting atomic force microscopy. *Adv. Mater.* **26**, 6069–6073 (2014).
124. Kiefer, D., et al. Double doping of conjugated polymers with monomer molecular dopants. *Nat. Mater.* **18**, 149–155 (2019).
125. Yamashita, Y., et al. Supramolecular cocrystals built through redox-triggered ion intercalation in π-conjugated polymers. *Commun. Mater.* **2**, 1–9 (2021).
126. Lüssem, B., et al.*Chem. Rev.*, 2016, 116, 13714–13751.
127. Fujimoto, R., et al. Molecular doping in organic semiconductors: fully solution-processed, vacuum-free doping with metal–organic complexes in an orthogonal solvent. *J. Mater. Chem. C* **5**, 12023–12030 (2017).
128. Zhao, Z., et al. In Situ Synthesis of Trifluoroacetic Acid-Doped Polyaniline/Reduced Graphene Oxide Composites for High-Performance All-Solid-State Supercapacitors. *ACS Appl. Energy Mater.* **3**, 8774–8785 (2020).
129. Bridges, C. R. & Baumgartner, T. Lewis acids and bases as molecular dopants for organic semiconductors. *J. Phys. Org. Chem.* **33**, 1–17 (2020).
130. Bergquist, C., et al. Aqua, alcohol, and acetonitrile adducts of tris(perfluorophenyl)borane: Evaluation of Bronsted acidity and ligand lability with experimental and computational methods. *J. Am. Chem. Soc.* **122**, 10581–10590 (2000).
131. Suh, E. H., et al. Brønsted Acid Doping of P3HT with Largely Soluble Tris(pentafluorophenyl)borane for Highly Conductive and Stable Organic Thermoelectrics Via One-Step Solution Mixing. *Adv. Energy Mater.* , DOI:10.1002/aenm.202002521.
132. Yamashita, Y., et al. Efficient molecular doping of polymeric semiconductors driven by

anion exchange. *Nature* **572**, 634–638 (2019).
133. Lim, E., Peterson, K. A., Su, G. M. & Chabinyc, M. L. Thermoelectric Properties of Poly(3-hexylthiophene) (P3HT) Doped with 2,3,5,6-Tetrafluoro-7,7,8,8-tetracyanoquinodimethane (F4TCNQ) by Vapor-Phase Infiltration. *Chem. Mater.* **30**, 998–1010 (2018).
134. Fontana, M. T., et al. Evaporation vs Solution Sequential Doping of Conjugated Polymers: F4TCNQ Doping of Micrometer-Thick P3HT Films for Thermoelectrics. *J. Phys. Chem. C* **123**, 22711–22724 (2019).
135. Hase, H., et al. Unraveling the Microstructure of Molecularly Doped Poly(3-hexylthiophene) by Thermally Induced Dedoping. *J. Phys. Chem. C* **122**, 25893–25899 (2018).
136. Cochran, J. E., et al. Molecular interactions and ordering in electrically doped polymers: Blends of PBTTT and F4TCNQ. *Macromolecules* **47**, 6836–6846 (2014).
137. Watts, K. E., Neelamraju, B., Ratcliff, E. L. & Pemberton, J. E. Stability of Charge Transfer States in F4TCNQ-Doped P3HT. *Chem. Mater.* **31**, 6986–6994 (2019).
138. Nagamatsu, S. & Pandey, S. S. Ordered arrangement of F4TCNQ anions in three-dimensionally oriented P3HT thin films. *Sci. Rep.* **10**, 1–10 (2020).
139. Untilova, V., Biskup, T., Biniek, L., Vijayakumar, V. & Brinkmann, M. Control of Chain Alignment and Crystallization Helps Enhance Charge Conductivities and Thermoelectric Power Factors in Sequentially Doped P3HT:F4TCNQ Films. *Macromolecules* **53**, 2441–2453 (2020).
140. Jacobs, I. E., et al. Polymorphism controls the degree of charge transfer in a molecularly doped semiconducting polymer. *Mater. Horizons* **5**, 655–660 (2018).
141. Jacobs, I. E. & Moulé, A. J. Controlling Molecular Doping in Organic Semiconductors. *Adv. Mater.* **29**, 1–39 (2017).
142. Dong, C. D. & Schumacher, S. Molecular Doping of PCPDT-BT Copolymers: Comparison of Molecular Complexes with and without Integer Charge Transfer. *J. Phys. Chem. C* **123**, 30863–30870 (2019).
143. Zapata-Arteaga, O., et al. Closing the Stability-Performance Gap in Organic Thermoelectrics by Adjusting the Partial to Integer Charge Transfer Ratio. *Macromolecules* **53**, 609–620 (2020).
144. Yurash, B., et al. Towards understanding the doping mechanism of organic semiconductors by Lewis acids. *Nat. Mater.* **18**, 1327–1334 (2019).
145. Arvind, M., et al. Quantitative Analysis of Doping-Induced Polarons and Charge-Transfer Complexes of Poly(3-hexylthiophene) in Solution. *J. Phys. Chem. B* **124**, 7694–7708 (2020).
146. Marqués, P. S., et al. Understanding how Lewis acids dope organic semiconductors: A 'complex' story. *Chem. Sci.* **12**, 7012–7022 (2021).
147. Pingel, P., et al. p-Type Doping of Poly(3-hexylthiophene) with the Strong Lewis Acid Tris(pentafluorophenyl)borane. *Adv. Electron. Mater.* **2**, 1600204 (2016).
148. Duong, D. T., Wang, C., Antono, E., Toney, M. F. & Salleo, A. The chemical and structural origin of efficient p-type doping in P3HT. *Org. Electron.* **14**, 1330–1336 (2013).
149. Aziz, E. F., et al. Localized charge transfer in a molecularly doped conducting polymer. *Adv. Mater.* **19**, 3257–3260 (2007).
150. Doerrer, L. H. & Green, M. H. Oxidation of [M(?-C5 H5)2], M ⊐ Cr, Fe or Co, by the new

Brønsted acid H2OɔB(C6F5)3 yielding the salts [M(?-C5H5)2]ℏ Aℓ , where Aℓ ℬ [(C6 F5)3B(?-OH)B(C6F5)3]ℓ or [(C6F5)3BOHɔɔɔH2OB(C6F5)3]. *Dalt. Trans.* 4325–4329 (1999).
151. Zujovic, Z., Kilmartin, P. A. & Travas-Sejdic, J.*Molecules*, 2020, 25.
152. Seifrid, M. T., Reddy, G. N. M., Zhou, C., Chmelka, B. F. & Bazan, G. C. Direct Observation of the Relationship betweenMolecular Topology and Bulk Morphology for a Ï€-Conjugated Material. *J. Am. Chem. Soc.* **141**, 5078–5082 (2019).
153. Seifrid, M., Reddy, G. N. M., Chmelka, B. F. & Bazan, G. C.*Nat. Rev. Mater.*, 2020, 5, 910–930.
154. Melnyk, A., et al. Macroscopic Structural Compositions of π-Conjugated Polymers: Combined Insights from Solid-State NMR and Molecular Dynamics Simulations. *J. Phys. Chem. Lett.* **8**, 4155–4160 (2017).
155. Yurash, B., et al. Atomic-Level Insight into the Postsynthesis Band Gap Engineering of a Lewis Base Polymer Using Lewis Acid Tris(pentafluorophenyl)borane. *Chem. Mater.* **31**, 6715–6725 (2019).
156. Karki, A., et al. Unifying Energetic Disorder from Charge Transport and Band Bending in Organic Semiconductors. *Adv. Funct. Mater.* **29**, 1901109 (2019).
157. Yurash, B., et al. Towards understanding the doping mechanism of organic semiconductors by Lewis acids. *Nat. Mater.* **18**, 1327–1334 (2019).
158. Farnan, I., et al. Quantification of the disorder in network-modified silicate glasses. *Nature* **358**, 31–35 (1992).
159. Duer, M. J. *Solid-State NMR Spectroscopy Principles and Applications*. (Blackwell Science Ltd, 2001).
160. Devreux, F., Bidan, G., Syed, A. A. & Tsintavis, C. Solid state 13C NMR in conducting polymers. *J. Phys.* **46**, 1595–1601 (1985).
161. Kolbert, A. C., et al. NMR evidence for the metallic nature of highly conducting polyaniline. *Phys. Rev. B* **51**, 1541–1545 (1995).
162. Méndez, H., et al. Charge-transfer crystallites as molecular electrical dopants. *Nat. Commun.* , DOI:10.1038/ncomms9560.
163. Scholes, D. T., et al. The Effects of Crystallinity on Charge Transport and the Structure of Sequentially Processed F4TCNQ-Doped Conjugated Polymer Films. *Adv. Funct. Mater.* **27**, 1–13 (2017).
164. Hynynen, J., et al. Enhanced Electrical Conductivity of Molecularly p-Doped Poly(3-hexylthiophene) through Understanding the Correlation with Solid-State Order. *Macromolecules* **50**, 8140–8148 (2017).
165. Tait, C. E., et al. Spin-spin interactions and spin delocalisation in a doped organic semiconductor probed by EPR spectroscopy †. *Phys. Chem. Chem. Phys* **23**, 13827 (2021).
166. Brown, S. P. Probing proton-proton proximities in the solid state. *Prog. Nucl. Magn. Reson. Spectrosc.* **50**, 199–251 (2007).
167. Brown, S. P. & Spiess, H. W. Advanced solid-state NMR methods for the elucidation of structure and dynamics of molecular, macromolecular, and supramolecular systems. *Chem. Rev.* **101**, 4125–4155 (2001).
168. Brown, S. P. Applications of high-resolution1H solid-state NMR. *Solid State Nucl. Magn. Reson.* **41**, 1–27 (2012).

169. Privitera, A., et al. Electron spin as fingerprint for charge generation and transport in doped organic semiconductors †. , DOI:10.1039/d0tc06097f.
170. Biskup, T. Structure-function relationship of organic semiconductors: Detailed insights from time-resolved EPR spectroscopy. *Front. Chem.* , DOI:10.3389/fchem.2019.00010.
171. Hušák, M., et al. Determining the Crystal Structures of Peptide Analogs of Boronic Acid in the Absence of Single Crystals: Intricate Motifs of Ixazomib Citrate Revealed by XRPD Guided by ss-NMR. *Cryst. Growth Des.* **18**, 3616–3625 (2018).
172. Misseeuw, L., et al. Optical-quality controllable wet-chemical doping of graphene through a uniform, transparent and low-roughness F4-TCNQ/MEK layer. *RSC Adv.* **6**, 104491–104501 (2016).
173. Krupskaya, Y., Gibertini, M., Marzari, N. & Morpurgo, A. F. Band-Like electron transport with record-high mobility in the TCNQ family. *Adv. Mater.* **27**, 2453–2458 (2015).
174. Malcolm H Levitt. *Spin Dynamics: Basics of Nuclear Magnetic Resonance*. (John Wiley & Sons, Ltd, 2015).
175. Fediai, A., Emering, A., Symalla, F. & Wenzel, W. Disorder-driven doping activation in organic semiconductors. *Phys. Chem. Chem. Phys.* **22**, 10256–10264 (2020).
176. Samanta, S., Raval, P., Manjunatha Reddy, G. N. & Chaudhuri, D. Cooperative Self-Assembly Driven by Multiple Noncovalent Interactions: Investigating Molecular Origin and Reassessing Characterization. *ACS Cent. Sci.* , DOI:10.1021/acscentsci.1c00604.

# VI. Conclusions

Fundamental studies of mechanisms allowing for the customizable optical and electronic performance of organic semiconductors are integral for the continued advancement in organic electronic devices. It is my hope that the work of my colleagues and presented in this thesis demonstrates the benefits of maximizing the efficiency of energy harvesting from upconversion sensitizers. Additionally, I hope this study can contribute a new design strategy to develop other upconversion systems which function with threshold light intensities much closer to that provided by focused sunlight as one of the attractive aspects of photon upconversion is the ability to produce higher energy emissions with low excitation power densities. The comparative study of dopant-polymer morphology should indicate the power of solid-state magnetic resonance spectroscopy in understanding how differences in molecular-level interactions influence the performance of different dopants and how these spectroscopic tools can be used to inform theories on doping mechanisms.

## *A. Conclusions Regarding the Design of Ternary Photon Upconversion System*

In this work, we demonstrated the increase in photoluminescence quantum yield of upconversion using the TADF sensitizer 4CzIPN in a ternary upconversion system. Through DFT calculations and time-dependent photoluminescence measurements, we chose 1-methylnaphthalene to serve as the triplet acceptor based on its high triplet energy and its high efficiency in accepting triplet excitons from 4CzIPN. The addition of p-terphenyl as the singlet emitter maintained the high anti-Stokes shift of 0.83 eV while more than doubling the maximum photoluminescence UC quantum yield from 3.4% in the binary solution of 4CzIPN and p-terphenyl to 7.6% in the ternary solution. Although the ternary system also showed a high

threshold excitation intensity, this could be altered by changing the excitation wavelength, potentially altering the sensitizer concentration, or utilizing molecular design strategies to pre-arrange the sensitizer and acceptor components or enable their self-assembly.[80,106,107] We also show that the use of 4CzIPN-Br with a higher $\Phi_{ISC}$, but similar $S_1$ and $T_1$ energy levels to 4CzIPN, resulted in significantly lower delayed fluorescence quenching for the acceptors naphthalene, 1-methylnaphthalene and p-terphenyl, suggesting the need for a greater understanding of the factors governing $\Phi_{TET}$ between these molecules. While the excitation threshold intensity can still be improved by controlling the relative organization of the upconversion components, this research provides an example of an effective acceptor screening process, demonstrates the unique opportunities 3-component upconversion blends, provides for tuning individual steps of upconversion, and highlights the need to control $I_{th}$ in the ternary TTA-UC systems.

### *B. Conclusions Regarding the Solid-State Magnetic Resonance Study of Doped Polymer Morphology*

The use of high resolution ssNMR and EPR techniques through this work has provided valuable insights into the intermolecular interactions at sub-nanometer distances, which underlie the previously observed difference in doping efficiency between these molecular dopants. In the case of P4:BCF blend, the BCF molecules are closely associated with P4 backbones, though they cause minimal disruption to the conjugated backbone stacking which is critical for charge transport in organic semiconductors. In addition, BCF can interact with traces of water molecules to form Brønsted acid BCF-water complexes. The $^{11}$B NMR signals corresponding to tri- and tetracoordinated BCF complexes are distinguished and identified. EPR analysis further

corroborates the close polymer-dopant interactions, suggesting that the BCF-water complexes serve as Brønsted acid sites to enhance the doping efficiency (> 14%). By comparison, the combined EPR and NMR results indicate that the fully doped F4TCNQ molecules are closely associated with P4 backbones, and the undoped F4TCNQ molecules are distributed into different aggregates, specifically by illustrating the 2D $^{1}$H and $^{19}$F NMR measurements and analysis. This observation together with F4TCNQ aggregation help to explain the much lower doping efficiency (< 4%) in P4:F4TCNQ.[144] Insight into the hyperfine interactions in P4, P4:BCF and P4:F4TCNQ blends is obtained by analyzing pulse 2D HYSCORE spectra. Furthermore, these results are complemented by $^{1}$H longitudinal relaxation ($T_1$) measurements and analysis that indicate that the addition of dopants has an impact on the relaxation behaviors of $^{1}$H sites in P4 polymers. Therefore, high-resolution ssNMR and EPR approach can be applied to obtain essential structural insights and have much wider relevance to characterize intermolecular interactions in small molecule doped π-conjugated polymers.

# VII. Appendix

## *A. Design of Ternary Photon Upconversion System*

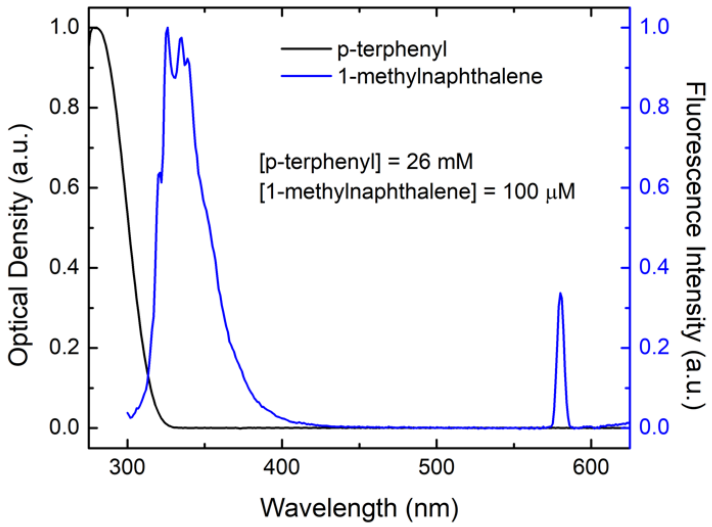


**Figure 7.1. Absorbance spectrum of neat p-terphenyl ($26 \times 10^{-3}$ M) in benzene with the emission spectrum (excitation wavelength = 290 nm) of neat 1-methylnaphthalene in benzene ($100 \times 10^{-6}$ M M). Second order diffraction of the excitation wavelength can be seen near 580 nm.**

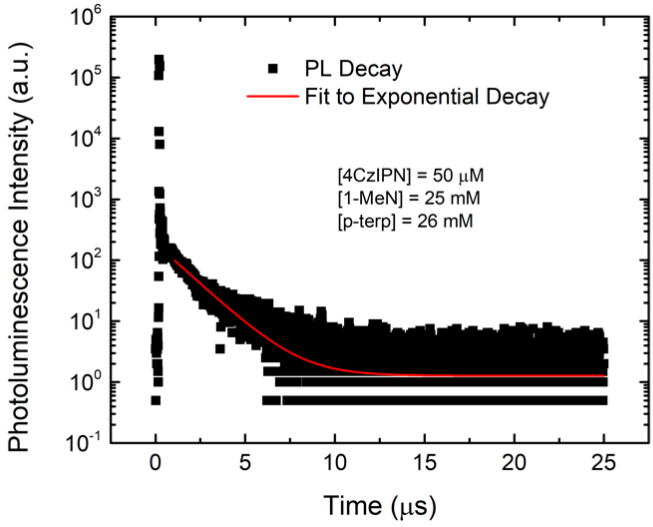


**Figure 7.2. Time-resolved photoluminescence of 50 μM 4CzIPN with 25 mM each of p-terphenyl and 1-methylnaphthalene. The excitation wavelength was 455 nm and the emission 2 was monitored at 350 nm. The sample was illuminated at 5 kHz repetition rate. Fitting the slow component to a single exponential resulted in a time constant of 1.6 μs, which is commensurate with the PL originating from a triplet state in 4CzIPN.**

This measurement was performed with a high peak intensity femtosecond excitation light source (Coherent Astrella Regenerative amplifier and Light Conversions Topas Prime Optical Parametric Aplifier with optical harmonics unit). The pulse energy density for the 150 fs pulse is about 10 mJ/cm$^2$. Becker and Hickl MSA-300 multiscaler and Hamamatsu R928P photomultiplier tube were used for the transient recording. The laser pulse peak power density in these experiments is on the order of GW/cm$^2$ which makes multiphoton processes significant. We believe that the fast component of the emission decaying on the time-scale of a few nanoseconds is attributable to the multiphoton absorption of the solvent (benzene) and consecutive excitation of p-terphenyl by its photoluminescence, as well as possibly direct two-photon excitation of the UV-emitting molecules.

1. Additional Discoveries on Upconversion Efficiency

One might contend that our observed efficiency increase of the ternary blend compared to the binary blend is merely a result of the increased total concentration of triplet acceptors. However, we do not believe this to be the case on account of several reasons. First, let us consider the efficiency of TTA, $\Phi_{TTA}$, as indicated in main text Equation 8. Our DFT calculations and quenching efficiency experiments both suggest that 1-methylnaphthalene has a lower T1 energy than p-terphenyl. Thus, although both p-terphenyl and 1-methylnaphthalene can undergo TET from 4CzIPN triplets, these triplets will quickly diffuse to the lowest energy T1 state available, which is undoubtedly that of 1-methylnaphthalene. For this reason, we expect p-terphenyl triplet states to undergo TET to 1-methylnaphthalene before they have a chance to undergo TTA and we also expect that the vast majority of TTA events occur between 1-methylnaphthalene molecules. When comparing the ternary blend to the binary blends, the concentration of the species responsible for TTA events, and their concomitant average intermolecular separation, is thus equivalent.

Second, let us consider the efficiency of TET, $\Phi_{TET}$, as indicated in main text Equation 8. The quenching efficiency (main text Figure 3.2) of $25 \times 10^{-3}$ M 1-methylnaphthalene is nearly unity (0.96), whereas that of p-terphenyl is only 0.57. Because 96% of 4CzIPN triplets are already quenched by $25 \times 10^{-3}$ M 1-methylnaphthalene, the addition of $25 \times 10^{-3}$ M p-terphenyl to a solution of 4CzIPN and $25 \times 10^{-3}$ M 1-methylnaphthalene could at most increase $\Phi_{TET}$ from 96% to 100%, which is only a 4% increase. This cannot account for the more than 2x increase of $\eta$UC observed in the ternary system compared to the binary systems (main text Figure 3.4). Indeed, when we measured the upconversion of a solution of 50 μM 4CzIPN with 50mM 1-methylnaphthalene, increasing the acceptor concentration by a factor of 2, there was no

significant increase in upconversion intensity (Figure 7.3a). This suggests that, for these excitation intensities, $\Phi_{TET}$ and $\Phi_{TTA}$ are already approaching unity at $25 \times 10^{-3}$ M 1-methylnaphthalene.

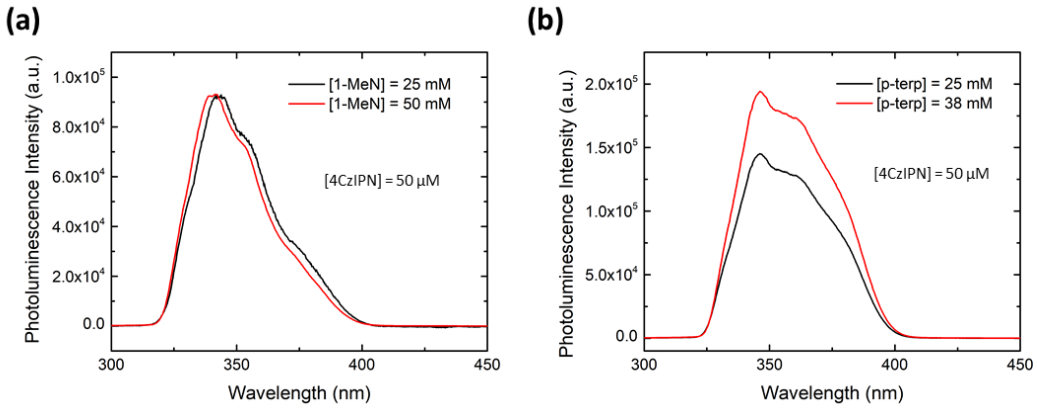


**Figure 7.3. (a) Upconversion spectra of binary blends with 4CzIPN and 1-methylnaphthalene under 335 W/cm$^2$ illumination at $25 \times 10^{-3}$ M and $50 \times 10^{-3}$ M. (b) Upconversion spectra of binary blends with 4CzIPN and p-terphenyl under 335 W/cm$^2$ illumination at $25 \times 10^{-3}$ M and $38 \times 10^{-3}$ M. For p-terphenyl the maximum solubility is around $40 \times 10^{-3}$ M.**

We were unable to prepare a solution of $50 \times 10^{-6}$ M 4CzIPN with $50 \times 10^{-3}$ M p-terphenyl due to precipitation of p-terphenyl at that concentration. The highest concentration of p-terphenyl we could achieve while maintaining solubility was $38 \times 10^{-3}$ M. Figure 7.9b shows an increase in upconversion intensity of a factor of 1.3 when increasing the concentration of p-terphenyl from $25 \times 10^{-3}$ M to $38 \times 10^{-3}$ M (factor of 1.5 increase in concentration). This increase is most likely attributable to an increase in $\Phi_{TET}$ which benefits from the increased concentration of acceptor in this case, unlike for 1-methylnaphthalene, since the quenching efficiency of p-terphenyl at $25 \times 10^{-3}$ M is only 57% and not so close to unity. At any rate, this data can be extrapolated to estimate what increase in upconversion intensity we might observe for $50 \times 10^{-3}$ M p-terphenyl. Given a 1.3x increase in upconversion for a 1.5x increase in concentration, a 2x increase in concentration

($50 \times 10^{-3}$ M p-terphenyl) is expected to produce about a 1.7x increase in upconversion. Thus, the upconversion efficiency, $\eta_{UC}$, would be expected to increase from 3.4% at $25 \times 10^{-3}$ M p-terphenyl to 5.8% at $50 \times 10^{-3}$ M. Again, this shows that concentration alone cannot explain the observed increase in upconversion efficiency in the ternary blend (7.6%) compared to the binary blends.

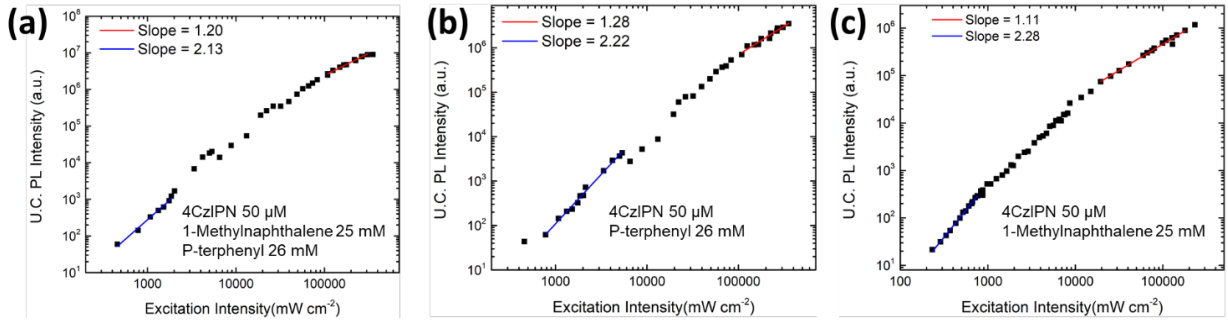


**Figure 7.4. Linear fits of the excitation intensity dependent upconversion photoluminescence intensity.**

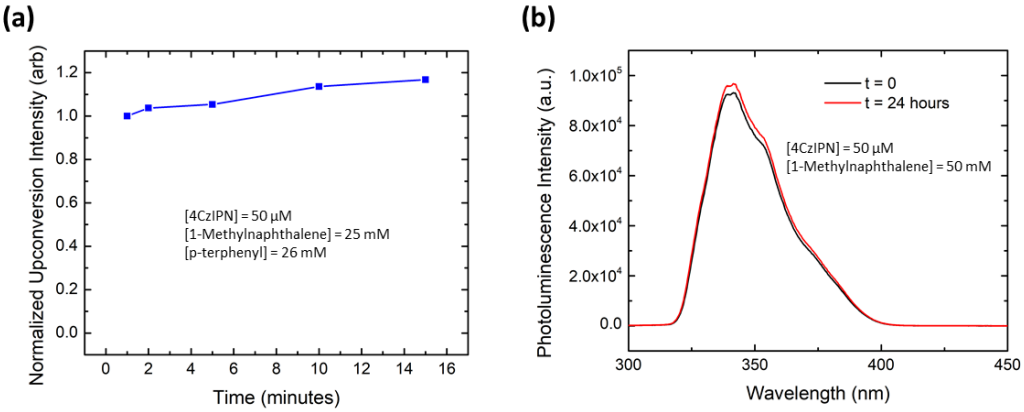


**Figure 7.5. (a) The integrated upconversion spectrum of a ternary blend was monitored as a function of time under 330 W/cm$^2$ illumination. The slight increase in intensity is most likely attributable to solution heating by the excitation laser, which increases diffusion rates and thus also the rate of TTA. For this reason, solutions were always allowed to equilibrate for some time while under excitation, until the upconversion intensity was stable, before taking measurements. (b) Upconversion spectra of a solution of $50 \times 10^{-6}$ M 4CzIPN with $50 \times 10^{-3}$ M 1- methylnaphthalene taken 24 hours apart. The subtle variation in intensity is most likely attributable to a slight change in alignment of the optical setup.**

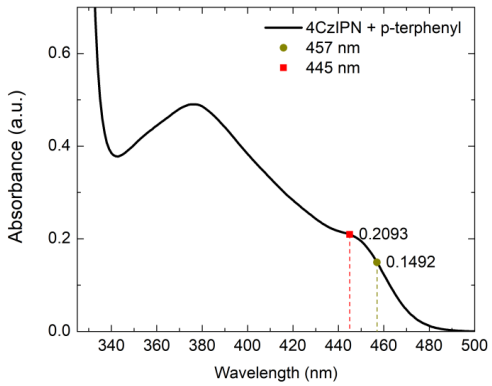


**Figure 7.6. Absorbance spectrum of 4CzIPN ($50 \times 10^{-6}$ M) and p-terphenyl ($25 \times 10^{-3}$ M) in benzene.**

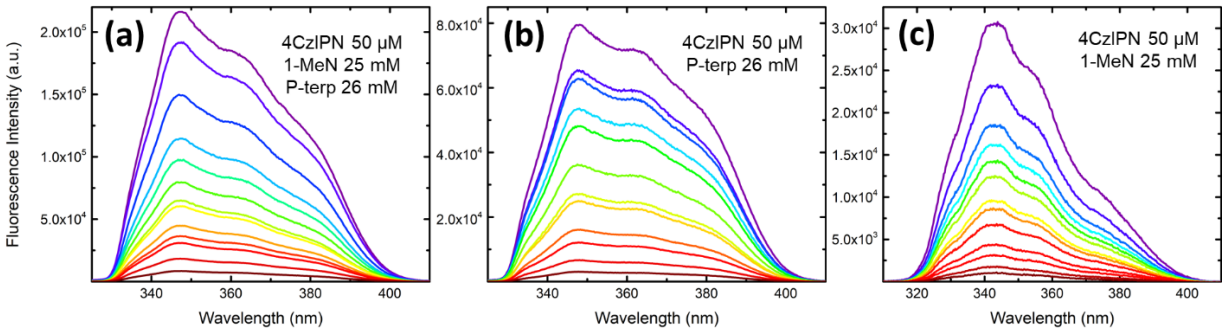


**Figure 7.7. Decrease in upconverted photoluminescence intensity with attenuation of the incident laser light. Measurements at every incident intensity used are not shown for each sample for simplicity.**

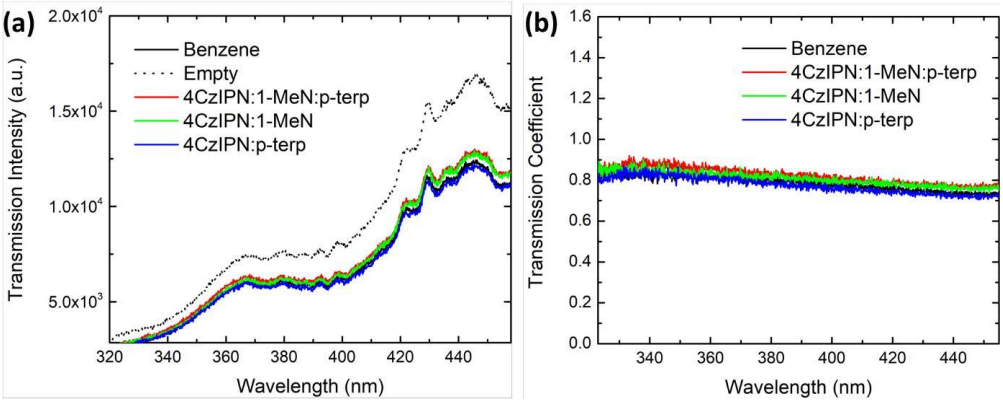

**Figure 7.8. (a) Transmission of UV light from the Ocean Optics DH-MINI through the contents of the integrating sphere. (b) Calculated reabsorption correction coefficient values.**

### *B. Morphology of Lewis Acid and F4TCNQ Doped Polymer*

1.$^{1}$H MAS NMR spectra of neat P4, P4:BCF and P4:F4TCNQ blends

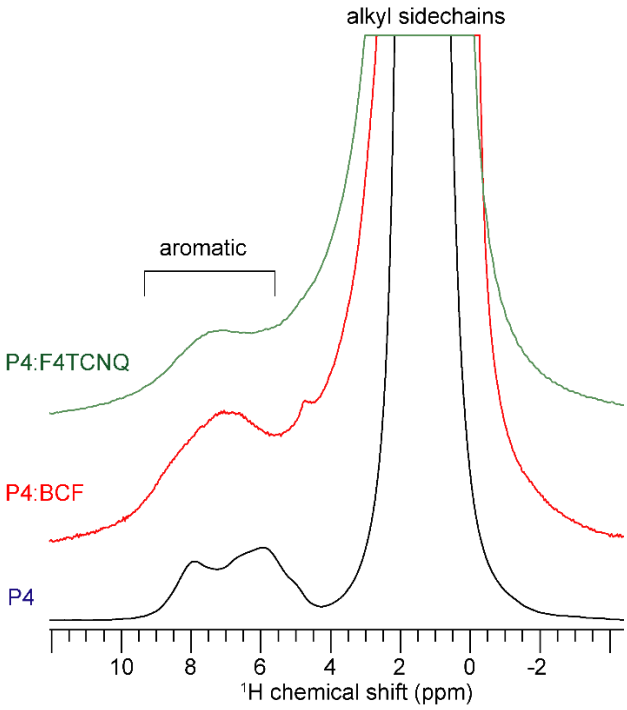


**Figure 7.9. Solid-state 1D $^{1}$H MAS NMR spectra of neat P4 and P4:BCF (1:1 molar ratio) and P4:F4TCNQ (1:0.2 molar ratio) blends show changes in the frequencies and lineshapes in the aromatic and aliphatic regions. All spectra were acquired at 18.8 T ($^{1}$H, 800.1 MHz) with 50 kHz MAS at room temperature.**

2. $^{1}H \rightarrow {}^{13}C$ CP-MAS spectra of neat P4, P4:BCF and P4:F4TCNQ blends

Figure 7.10 compares $^{13}C\{^{1}H\}$ CP MAS NMR spectra of neat P4, P4:BCF and P4:F4TCNQ blends. In a $^{13}C\{^{1}H\}$ CP MAS experiment, the $^{1}H$ and $^{13}C$ sites are simultaneously exited and $^{1}H \rightarrow {}^{13}C$ polarization transfer is achieved to enhance the intensities of these latter. While the conventional $^{13}C\{^{1}H\}$ CP-MAS spectra do not provide quantitative information because $^{13}C$ signals are nonuniformly enhanced by the polarization transfer from neighboring $^{1}H$ sites, nonetheless, relative peak integrals of alkyl versus aromatic signals in neat P4, P4:BCF and P4:F4TCNQ blends can be used to estimate the degree of broadening and intensity losses associated with the aromatic and aliphatic regions. In P4, the ratio of alkyl/aromatic signal intensity is 1.0/0.53. By comparison, the ratio of alkyl/aromatic signal intensities in P4:BCF and P4:F4TCNQ are 1.0/0.12 and 1.0/0.15, suggesting that the aromatic $^{13}C$ sites in the doped P4 polymers undergo greater signal intensity losses than the alkyl regions. Of particular note, aliphatic and aromatic sites of P4:dopant blends exhibit different degrees of intensity losses, as will be corroborated by the quantitative $^{1}H$ NMR analysis of neat P4 and P4-dopant blends discussed below.

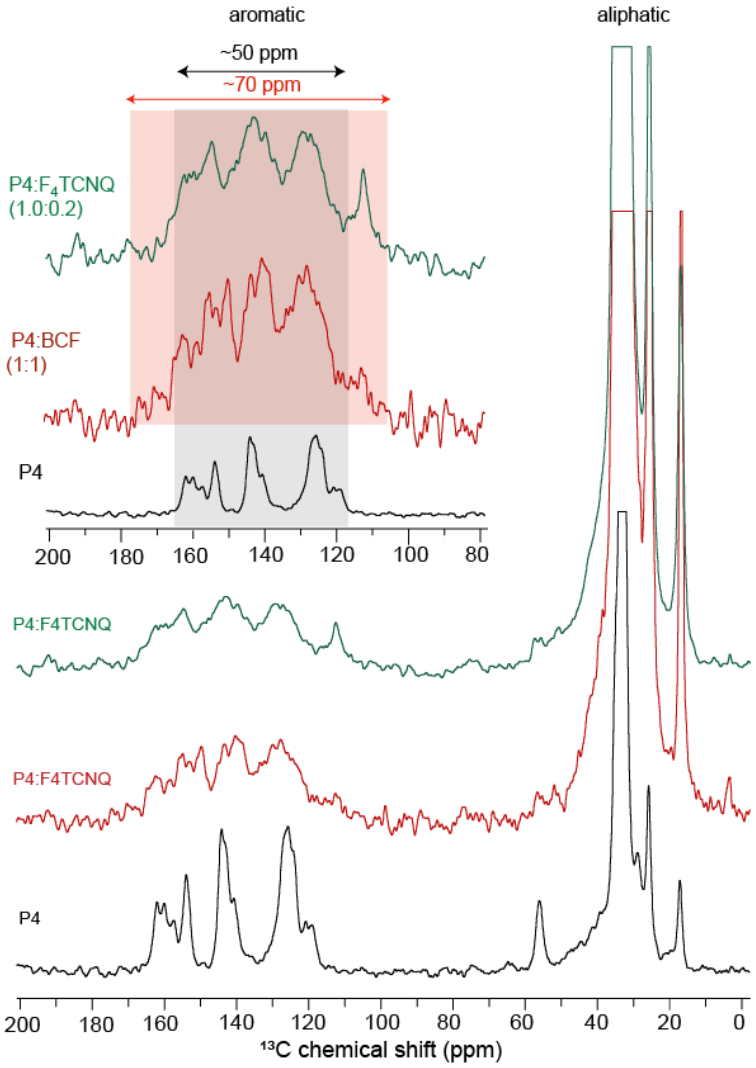


**Figure 7.10. Solid-state 1D $^{1}H \rightarrow ^{13}C$ CP MAS NMR of neat P4, P4:BCF (1:1) and P4:F4TCNQ (1:02) blends. Inset figure compares the expanded aromatic regions of neat P4 and blends depicting the signal broadening. All spectra were acquired at 9.4 T ($^{1}H$, 400 MHz) and at room temperature with 4 ms of CP contact time.**

3. Lineshape fitting analysis of 1D $^{1}$H MAS NMR spectra

For undoped and doped P4 polymers (~2.5 mg of each), $^{1}$H MAS spectra were acquired under identical experimental conditions, and the aliphatic/aromatic peak integrals were deconvoluted and compared (Figure 7.11). To convolute the lineshape of P4 $^{1}$H spectrum (Figure 7.12a), we use the knowledge of the aromatic $^{1}$H chemical shifts obtained from the analysis of 2D $^{1}$H-$^{13}$C and $^{1}$H-$^{1}$H correlation spectra (Figures 7.13 and 7.14). Although deconvolution analysis does not provide information on the relative populations of different aromatic and aliphatic $^{1}$H sites in doped polymers, nonetheless, it enables the aliphatic/aromatic signal integral ratio (66/4.7) in pristine P4 polymer to be estimated. In P4, the alkyl sidechains contain 66 hydrogen atoms and aromatic backbone contains 4 hydrogen atoms. By comparison, the peak integral of aliphatic signal in doped P4:F4TCNQ is ~36.3, (calibrated with respect to 66 in neat P4) in P4:BCF ~49.5, and P4:BCF+water is ~13.2, suggesting the signal intensity loss in aliphatic regions. In a similar manner, $^{1}$H signal intensity loss of aromatic groups is estimated for P4:dopant blends (Table 7.1). This analysis indicates that P4:F4TCNQ and P4:BCF blends exhibit different degrees of peak broadening and intensity loss, which can be attributable to different distributions of free radicals and doping mechanisms. With these factors in mind, we hypothesize that the detected $^{1}$H signal intensities are expected to be largely originating from the diamagnetic regions of doped polymers, making it difficult to obtain an accurate quantitative analysis of signal intensity loss.

**Figure 7.11. Lineshape analysis of 1D $^{1}$H MAS NMR spectra of (a) neat P4, (b) P4:F4TCNQ (1:0.2) (c) P4:BCF (1:1), and (d) P4:BCF (1:1) + water, indicating the different signal integrals, which are quantified and presented in Table 7.2. *denotes the signal from residual water.**

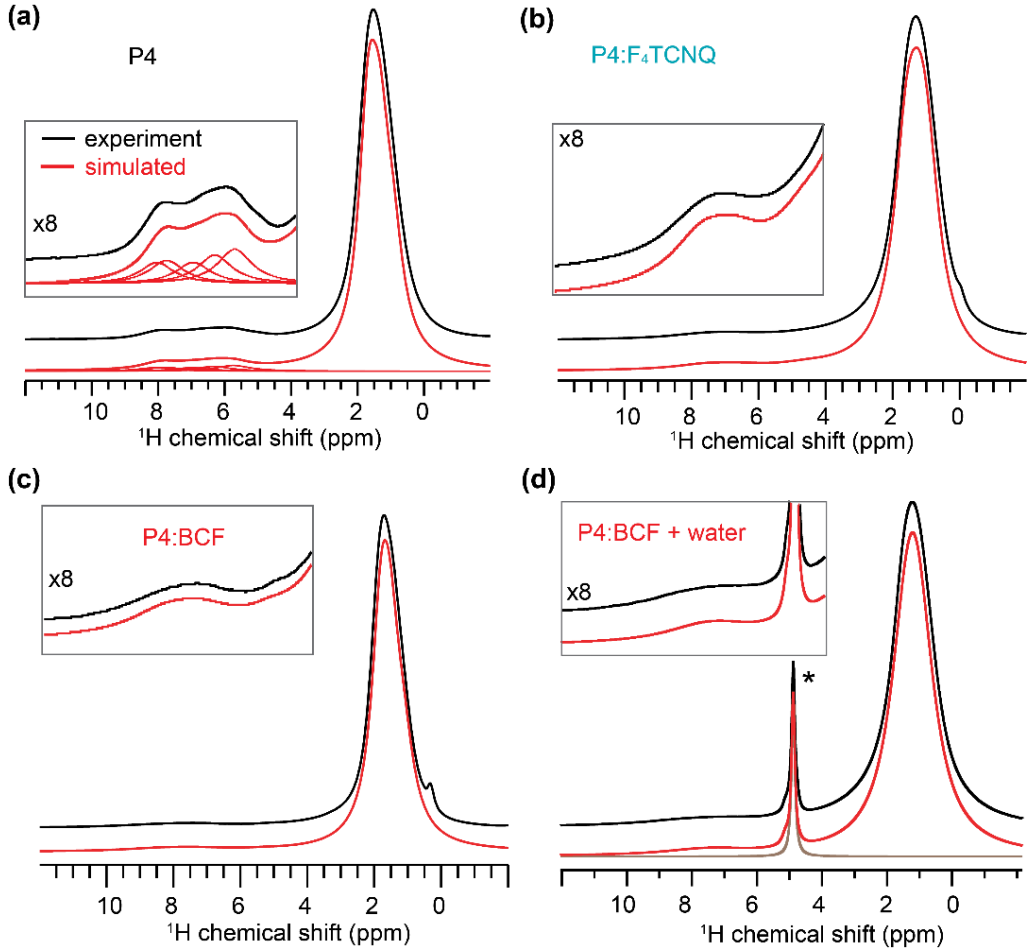

**Table 7.1. Aliphatic and aromatic $^{1}$H peak integrals in P4, and P4:BCF and P4:F4TCNQ materials**

| Material | $^{1}$H signal integral (a.u.) | |
|---|---|---|
| | Alkyl | Aromatic |
| P4 | 66.0 | 4.7 |
| P4:F4TCNQ (1:0.2) | 36.3 | 1.7 |
| P4:BCF (1:1) | 49.5 | 1.4 |
| P4:BCF (1:1) + water | 13.2 | 0.5 |

4. 2D $^{1}H$-$^{13}C$ heteronuclear correlation NMR spectrum of P4 polymer

In a 2D $^{1}H$-$^{13}C$ HETCOR spectrum presented in Figure S5, different distributions of 2D peaks between 20-40 ppm ($^{13}C$) and 0-3 ppm ($^{1}H$) are due to the inter- and intramolecular dipolar-coupled $^{1}H$-$^{13}C$ moieties in alkyl sidechains. A 2D peak at ~53 ppm ($^{13}C$) and 1-3 ppm ($^{1}H$) is due to the through-space interactions between quaternary carbon atom and alkyl sidechain protons (cyan arrows) as depicted in in the schematic structure. In the aromatic region, a peak at 124 ppm ($^{13}C$) and 5.7-6.4 ($^{1}H$) ppm is attributable to hydrogenated carbon atoms (cyan dots) of BT groups, and a peak at 125-126 ppm ($^{13}C$) and 7.2-8.4 ($^{1}H$) ppm is attributable to hydrogenated carbon atoms of CPDT groups. Notably, the weak intensity signal between hydrogenated carbon atoms (purple dots) and the alkyl sidechain protons indicates the close proximity between CPDT groups and thiophene carbon atoms (red arrows) as shown in the schematic structure. These peak assignments aid the analysis of $^{1}H$ DQ-SQ correlation spectra discussed in Figure 4.2 (main text) and Figures 7.14-7.16 discussed below, and provide a basis for the deconvolution analysis of the $^{1}H$ NMR spectrum presented in Figure 7.12a.

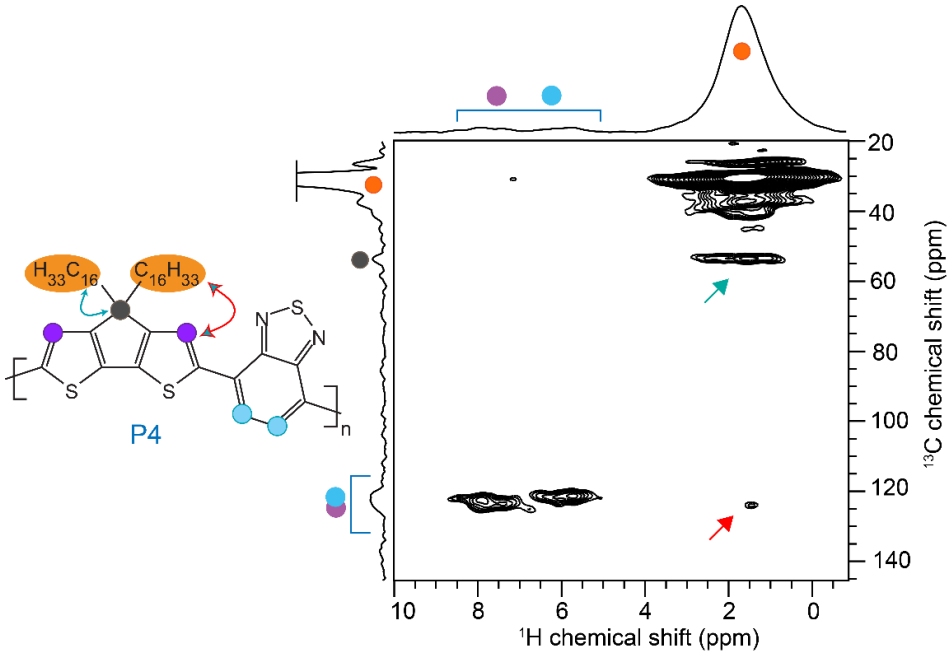


**Figure 7.12. Solid-state 2D $^{1}$H-$^{13}$C heteronuclear correlation (HETCOR, $^{1}$H-detected) spectrum of P4 acquired at 18.8 T ($^{1}$H, 800.1 MHz), 50 kHz MAS and at room temperature with 2 ms of CP contact time. The top horizontal and left vertical spectra are the summed projections of the $^{1}$H and $^{13}$C dimensions. 2D correlation peaks correspond to aliphatic and aromatic moieties are color coded as depicted in the schematic structure. The blue and red arrows indicate the through-space dipolar interactions between quaternary carbon atoms and alkyl sidechains (black dot), and between hydrogenated thiophene carbon atoms (purple dots) and alkyl sidechains.**

5. 2D $^{1}$H-$^{1}$H DQ-SQ correlation NMR spectrum of P4 polymer

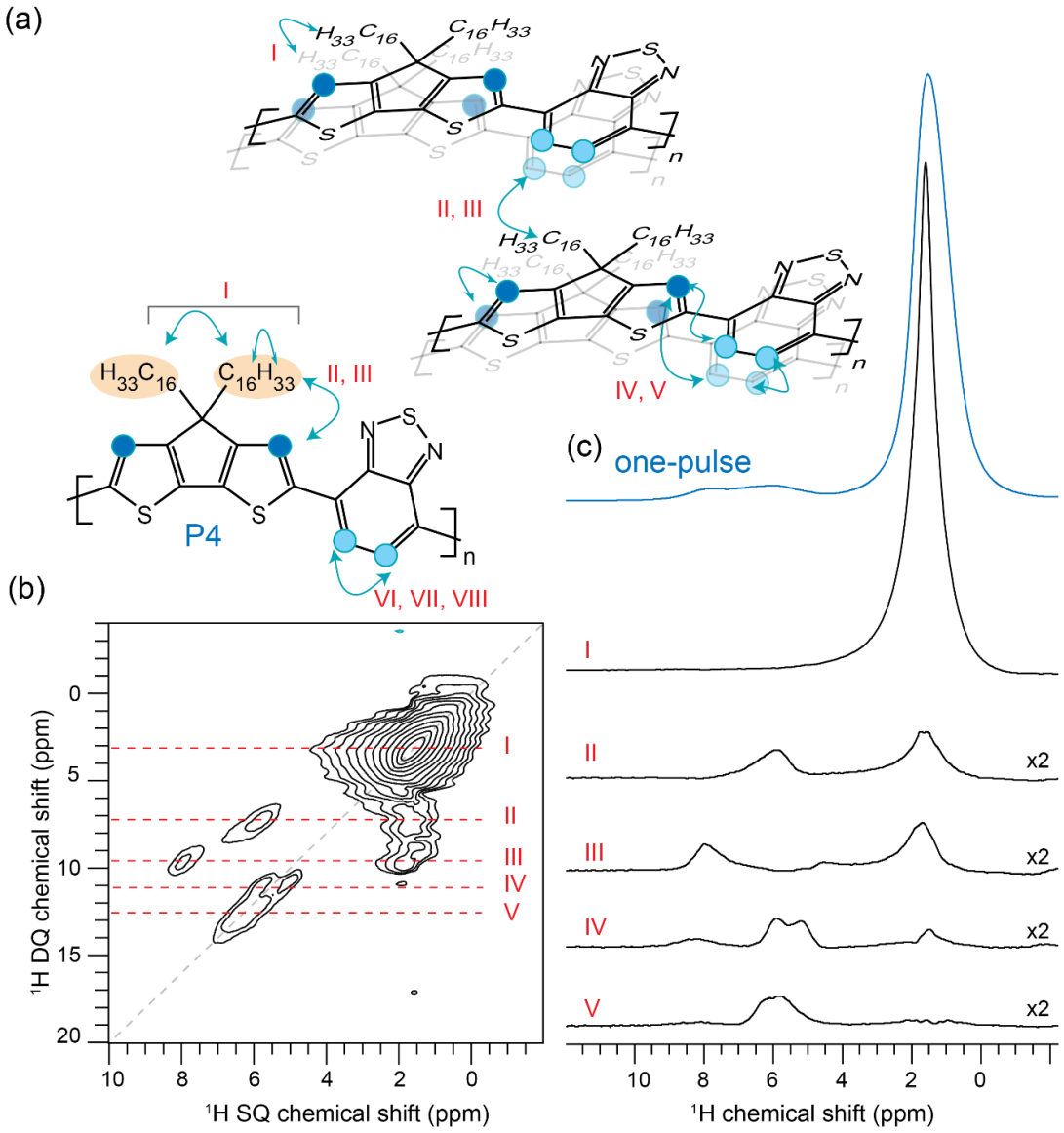


**Figure 7.13. (a) Molecular structure of P4 with specific $^{1}$H-$^{1}$H dipolar interactions that may contribute to $^{1}$H DQ signals. (b) Solid-state 2D $^{1}$H-$^{1}$H DQ-SQ correlation spectrum of pristine P4, together with (c) line-cut SQ spectra at specific DQ peaks correspond to the through-space interactions shown in (a). In (c), a single-pulse $^{1}$H spectrum is shown for a comparison. All spectra were acquired at 18.8 T ($^{1}$H, 800.1 MHz), 50 kHz MAS and at room temperature.**

6. 2D $^{1}$H-$^{1}$H DQ-SQ NMR spectra of P4:BCF and P4:F4TCNQ blends

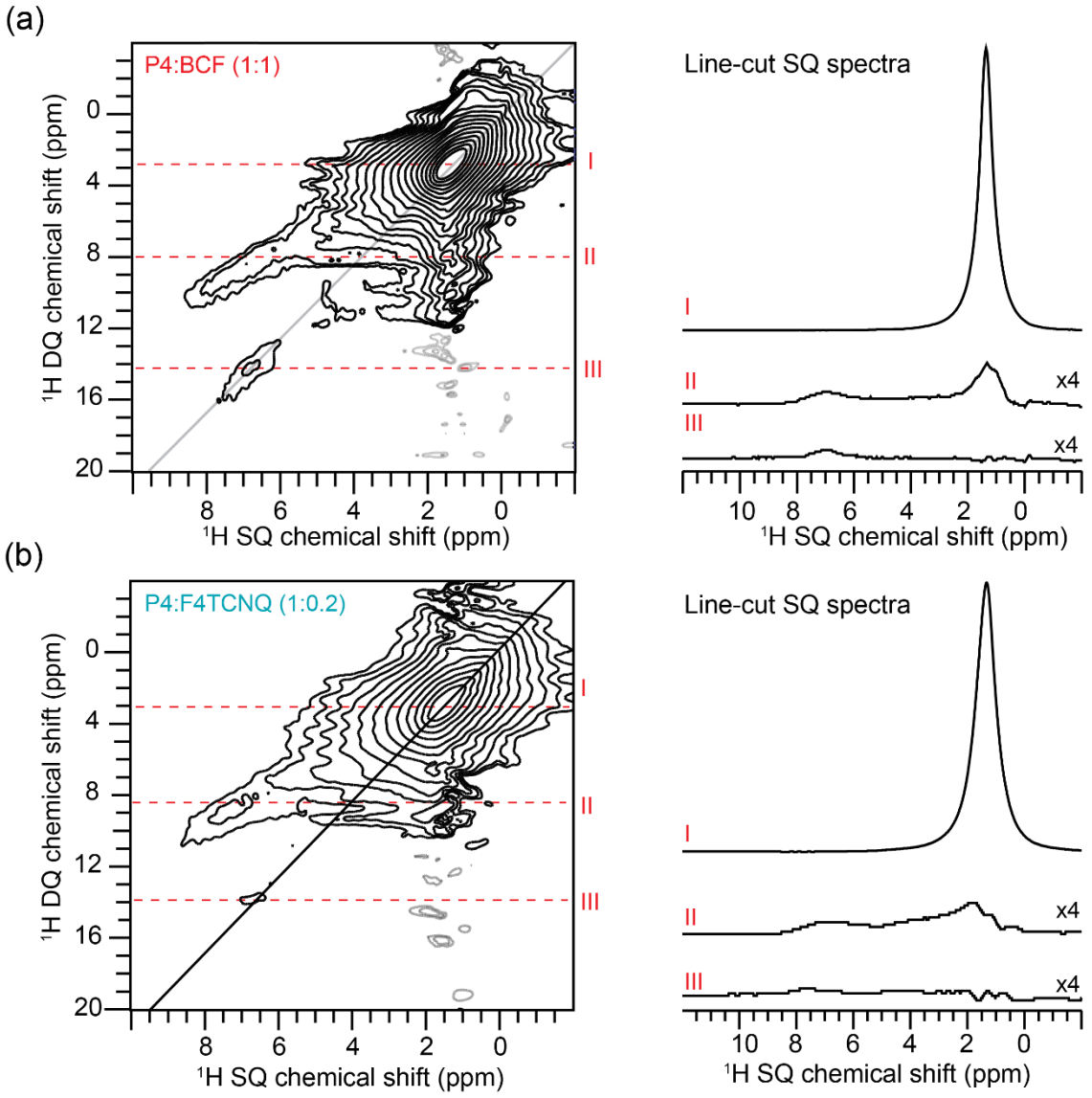


**Figure 7.14. Solid-state 2D $^{1}$H-$^{1}$H DQ-SQ correlation NMR spectra of (a) P4:BCF and (b) P4:F4TCNQ doped polymers together with their line-cut SQ spectra at specific DQ chemical shifts that indicate the significant intensity losses for aromatic regions of P4 polymer. Weak intensity aromatic peaks (III) in the line-cut spectra are most likely due to artifacts or expected to originate from weak residual $^{1}$H DQ signals of undoped polymer regions. This is consistent with the EPR analysis that showed the presence of F4TCNQ radicals (located at much closer proximities to P4 backbones) and BCF moieties (located in the vicinity of P4 backbones). All spectra were acquired at 18.8 T ($^{1}$H, 800.1 MHz) with 50 kHz MAS at room temperature.**

7. 2D $^{1}$H-$^{1}$H DQ-SQ NMR spectra of P4, P4:BCF and P4:F4TCNQ blends

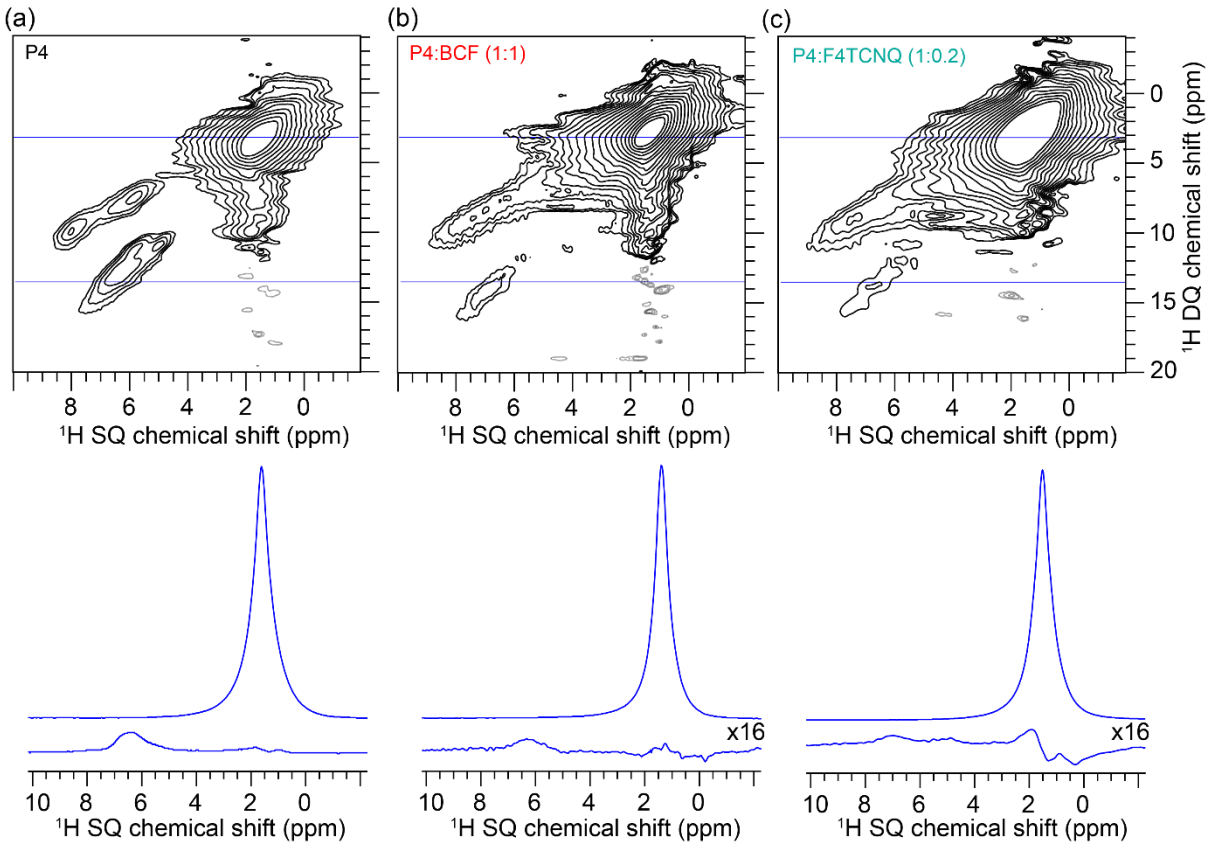


**Figure 7.15. Solid-state 2D $^{1}$H-$^{1}$H DQ-SQ correlation NMR spectra of (a) P4, (b) P4:BCF and (c) P4:F4TCNQ acquired with a longer recoupling time of 40 microseconds (corresponding to two rotor periods, $2\tau_r$ with 50 kHz MAS frequency). For each spectrum, line-cut SQ spectra extracted for the $^{1}$H DQ peaks at 3.5 and 13.5 ppm (horizontal blue solid lines in a-c) are compared in the bottom panels. Although the 2D peaks are relatively better visible in the aromatic regions of doped P4 polymers, their signal intensities remain closer to the noise level, indicating that these signals are most likely artifacts or very weak residual DQ peaks originating from the diamagnetic regions of the doped P4 polymers. The base contours are at (a) 6%, (b) 0.6% and (c) ~0.8% of the maximum peak intensity.**

8. EPR spectra of pristine P4, P4:F4TCNQ, P4:BCF and P4:BCF-water blends

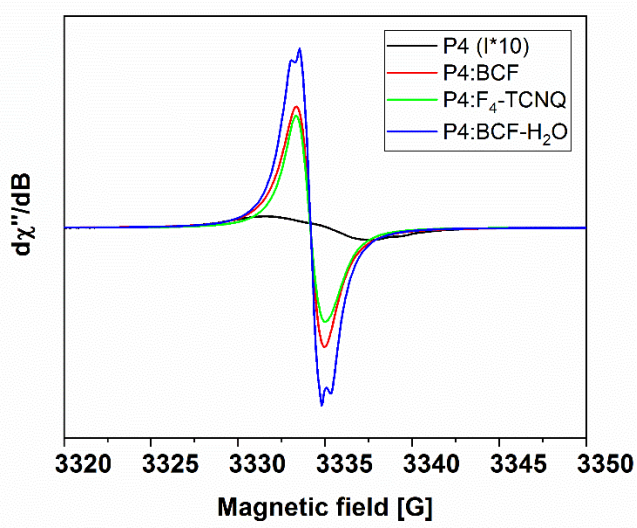


**Figure 7.16. Solid-state continuous-wave X-band EPR spectra of P4, P4:F4TCNQ, P4:BCF and P4:BCF-water blends indicating the differences in the signal intensities and spectral features.**

9. Longitudinal relaxation ($T_1$) measurements and analysis

For neat compounds and blends, longitudinal relaxation ($T_1$) values associated with aromatic and sidechain $^{1}$H sites were measured using saturation recovery experiments at 18.8 T (50 kHz MAS). A pseudo-2D NMR experiment was acquired using a saturation recovery sequence. $T_1$ values were measured using Topspin 4.0.6 package and compared (Table 7.2). For neat F4TCNQ, it was feasible to obtain a pseudo-2D NMR spectrum acquired as a function of saturation recovery delay. For P4:F4TCNQ (1:02), dilute concertation of dopant molecules and different distributions of $^{19}$F signals originating from different locally disordered regions lead to poor signal-to-noise ratio. In addition, these signals are obscured by a background signal.

Therefore, a $T_2$-fileter (i.e., a spin-echo block with 1 rotor period) was added to prevent the background signals in order to identify the $^{19}F$ signals originating from the dopants. $T_2$-filtered 1D $^{19}F$ spectra were acquired by varying a inter-scan repetition delay in the range between 0.5 s and 50 s (Figure 4.4, main text). $T_1$ values are given in Table 7.2.

**Table S2. $T_1$ relaxation times of $^1H$ sites in P4, and P4:BCF and P4:F4TCNQ materials**

| Material | $^1H$ $T_1$ relaxation time (s) | |
|---|---|---|
| | Alkyl chains | Aromatic groups |
| P4 | 0.93 | 0.98 |
| P4:F4TCNQ (1:0.2) | 0.16 | 0.03 |
| P4:BCF (1:1) | 0.87 | 0.89 |
| P4:BCF (1:1) + water | 0.57 | # |

| Material | $^{19}F$ $T_1$ relaxation time (s) |
|---|---|
| F4TCNQ | 378 |
| P4:F4TCNQ (1:0.2) | < 100 |

# signal intensity is too weak for $T_1$ values to be determined.

10. 2D $^{19}$F-$^{19}$F spin diffusion NMR spectra of P4:F4TCNQ blends

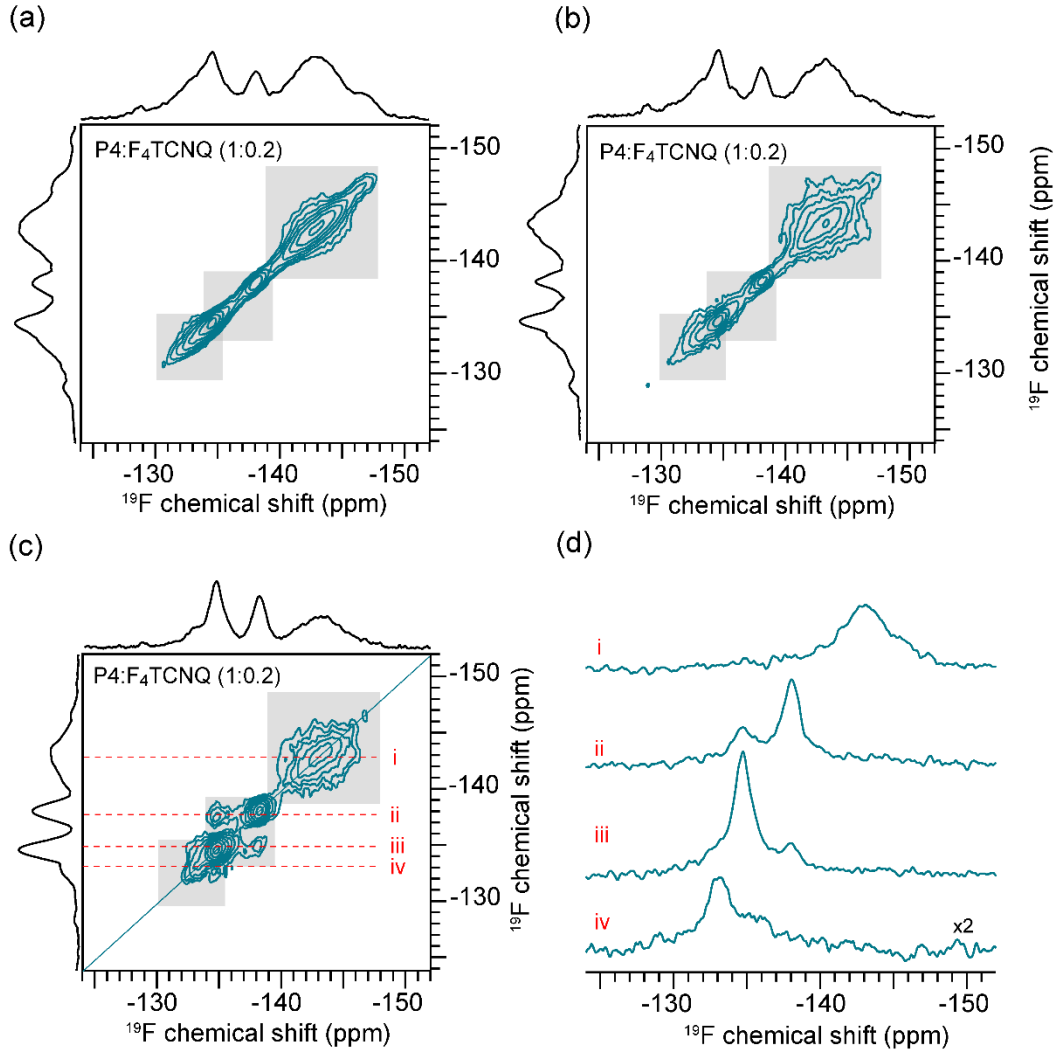


**Figure 7.17. Solid-state 2D $^{19}$F-$^{19}$F spin-diffusion NMR spectra of P4:F4TCNQ acquired with (a) 10 ms (b) 100 ms and (c) 500 ms of mixing time. The signals correspond to locally ordered and disordered regions are depicted in gray boxes. The cross peaks did not appear in (a) and (b), whereas cross peaks are observed between $^{19}$F sites in the ordered regions. (d) line-cut spectra extracted from (c) for different $^{19}$F signals (i-iv). All spectra were acquired at 18.8 T (Larmor frequency of $^{19}$F = 752.8 MHz) with 50 kHz MAS at room temperature.**

***Appendix References***


1 A. Khitrin and B. M. Fung, *J. Chem. Phys.*, 2000, **112**, 2392–2398.

2 I. Schnell and W. H. Spiess, *J. Magn. Reson.*, 2001, **151**, 153–227.

3 G. N. Manjunatha Reddy, M. Malon, A. Marsh, Y. Nishiyama and S. P. Brown, *Anal. Chem.*, 2016, **88**, 11412–11419.

4 Y. lee Hong, G. N. Manjunatha Reddy and Y. Nishiyama, *Solid State Nucl. Magn. Reson.*, 2020, **106**, 101651.

5 G. N. M. Reddy, A. Huqi, D. Iuga, S. Sakurai, A. Marsh, J. T. Davis, S. Masiero and S. P. Brown, *Chem. - A Eur. J.*, 2017, **23**, 2235.

6 A. Karki, J. Vollbrecht, A. L. Dixon, N. Schopp, M. Schrock, G. N. M. Reddy and T. Nguyen, *Adv. Mater.*, 2019, 1903868.

7 A. Karki, J. Vollbrecht, A. J. Gillett, S. S. Xiao, Y. Yang, Z. Peng, N. Schopp, A. L. Dixon, S. Yoon, M. Schrock, H. Ade, G. N. M. Reddy, R. H. Friend and T. Q. Nguyen, *Energy Environ. Sci.*, 2020, **13**, 3679–3692.